Stress relaxation cracking in AISI 316L-type austenitic stainless steels

Harry Pommier

ParisTech
INSTITUT DES SCIENCES ET TECHNOLOGIES
PARIS INSTITUTE OF TECHNOLOGY

MINES ParisTech

École doctorale №432: Sciences des Métiers de l'Ingénieur

Doctorat MINES ParisTech

T H È S E

pour obtenir le grade de docteur délivré par

l'École nationale supérieure des Mines de Paris

Spécialité "Science des Métiers de l'Ingénieur"

Présentée et soutenue publiquement par

Harry POMMIER

le 14 décembre 2015

Stress relaxation cracking in AISI 316L-type austenitic stainless steels

Fissuration en relaxation des aciers inoxydables austénitiques de type AISI 316L

Directeur de thèse : **Esteban P. BUSSO**
Maître de thèse : **Thilo F. MORGENEYER**
Co-encadrant de thèse : **André PINEAU**

Jury

Pr Peter E.J. Flewitt, University of Bristol	Rapporteur
Pr Noel P. O'Dowd, University of Limerick	Rapporteur
Pr Véronique Doquet, Directrice de recherche CNRS, École Polytechnique	Présidente du jury
Dr Sophie Dubiez-Le Goff, Ingénieur de recherche, AREVA NP	Examinateur
Dr Quentin Auzoux, Ingénieur de recherche, CEA Saclay	Examinateur
Pr Esteban P. Busso, Directeur scientifique, ONERA	Examinateur
Dr Thilo F. Morgeneyer, Chargé de recherche, École des Mines de Paris	Examinateur
Pr André Pineau, Professeur émérite, École des Mines de Paris	Examinateur
Dr Gilles Perrin, Ingénieur expert, Direction R&D, Areva NP	Membre invité

T H È S E

MINES ParisTech
Centre des Matériaux
10 rue Henri Desbruères, 91003 Evry, France

Abstract

Stress relaxation cracking can potentially be found in the heat affected zone of large welded parts after service in the 500-700°C temperature range. This phenomenon, also known as reheat cracking (RC), is driven by the high temperature relaxation of residual stress fields initially introduced during welding. The main objective of this doctoral thesis is to identify the material and microstructural characteristics as well as the driving forces responsible for RC damage development in AISI 316L-type austenitic stainless steels.

The proposed methodology relies on the reproduction of RC conditions in five chemically different AISI 316L-type steels using pre-compressed CT-like specimens. Subsequent investigation using SEM, EBSD, TEM and X-ray tomography revealed that intergranular damage had developed in some of the specimens. The extent of damage was found to depend on the steel grade, the temperature and duration of the thermal exposure, and the notch radius.

The numerical investigation of the local residual stress and strain fields in the specimens was carried out using a novel internal state variable-based viscoplastic constitutive model. A comparison between the predicted residual stress fields in the CT-like specimens and the intergranular damage distributions measured by X-ray tomography enabled the threshold level of local residual stresses associated with the initiation of stress relaxation microcracks to be inferred. Finally, the distribution of the measured local RC damage was modelled numerically by explicitly linking a suitable phenomenological scalar damage law with the above constitutive model. The corresponding results were found to be consistent with the observed damage distributions.

Keywords: AISI 316L, reheat cracking, intergranular damage, residual stress relaxation, viscoplastic constitutive model, synchrotron X-ray tomography

Preface

"Strength is the outcome of need;
security sets a premium on feebleness."

– H.G. Wells, *The Time Machine*

Aussi bien utilisés dans les centrales nucléaires que pour faire des fourchettes, les aciers inoxydables austénitiques nécessitent parfois des ingrédients atomiques finement dosés afin de correctement se tenir à la « cuisson ». Si l'on imagine que certains atomes sont des épices, la citation ci-dessus pourrait exprimer le fait qu'en métallurgie comme en cuisine, il est déconseillé de trop assaisonner un plat par zèle avec certaines d'entre elles...Mais avant d'entrer dans les explications nécessaires pour appréhender ce problème, je tiens à remercier les personnes qui ont permis l'aboutissement de ce travail de thèse.

Je remercie mon directeur de thèse, Esteban P. Busso, pour ses conseils avisés et pour sa volonté de toujours me faire progresser scientifiquement. Je le remercie également pour la liberté qu'il m'a accordée ainsi que la grande disponibilité dont il a fait preuve à mon égard jusqu'à la fin de ma thèse. Je tiens également à remercier Thilo F. Morgeneyer tout particulièrement pour son aide et ses enseignements concernant la partie expérimentale de ce travail. J'adresse également mes plus sincères remerciements à André Pineau qui a apporté énormément d'énergie et de bonnes idées et qui a toujours été disponible pour répondre à mes questions.

Je remercie Véronique Doquet qui m'a fait l'honneur de présider le jury de thèse, Peter E.J. Flewitt et Noel P. O'Dowd qui ont accepté de rapporter cette thèse ainsi que Sophie Dubiez-Le Goff, Quentin Auzoux et Gilles Perrin pour l'intérêt qu'ils ont porté à mon travail.

J'ai eu la chance, pendant ces années de thèse, de côtoyer les chercheurs, ingénieurs et techniciens du Centre des Matériaux. En particulier, Samuel Forest, Mathieu Mazière, Henri Proudhon, Vladislav Yastrebov, Vladimir Esin, Anne-Françoise Gourgues-Lorenzon, Jérôme Crépin, Jacques Besson, Yazid Madi, Alain Köster, Fabrice Gaslain, Anne Laurent, Mohammed Sennour, Abdennour Meddour, Régis Clement, Odile Adam, René Cluzet et Georges Cassas. Mais également, pêle-mêle, de nombreux thésards: Samuel Jules (compagnon de squash et de SC2), Victor Cruise (parapentiste bondouflois et footballeur-humoriste), Aurélien (roi du code et PGM-motard), Arina (lobbyiste chargée du tourisme en Normandie), Mouhcine (compère de bureau et de nuits blanches à l'ESRF), Geoffrey (pilote Tarbais d'aéronef), Raphael (Mister Lova-Lova du snowboard), Adrien (maçon de l'extrême), Michael (meilleur humoriste grivois de France), Franck (Ballon d'Or du CdM), mais aussi, Judith, Hayat, Hicham, Francesco, Josiane, David, Victor F., et évidemment la formidable Emma qui m'a énormément aidé et soutenu.

Je remercie également tous ceux qui ont contribué de près ou de loin à cette thèse : Lukas Helfen, Marco Di Michiel, Mario Scheel, Martine Blat, Vincent Robin, Yves Lejeail, Frederic Delabrouille, Marie José Cornu et les autres que j'oublie.

Finalement, j'aimerais adresser mes remerciements les plus chaleureux à ma famille et mes amis qui m'ont soutenu tout au long de cette thèse.

Contents

List of Figures

CHAPTER 1

Introduction

Résumé[1]

Les aciers inoxydables austénitiques sont largement utilisés dans l'industrie chimique et de l'énergie en raison de leur bonne résistance à la corrosion, leurs bonnes propriétés mécaniques jusqu'à environ 650°C et leur bonne soudabilité par les procédés conventionnels. En particulier, les aciers inoxydables austénitiques de type AISI 316L sont envisagés comme matériaux de structure pour les Réacteur à Neutron Rapide refroidis au sodium (RNR-Na) étudiés en France et conçus pour fonctionner à des températures de service proches de 550°C. Or, à ces températures, un retour d'expérience international a montré l'existence d'un phénomène d'endommagement intergranulaire suceptible d'apparaître en service dans les Zones Affectées Thermiquement (ZAT) de pièces soudées de fortes épaisseurs. Ce phénomène, connu sous le nom de fissuration en relaxation (FER) ou « reheat cracking », a été particulièrement observé dans les aciers 316H utilisés au Royaume-Uni dans les Réacteur Avancés refroidis au Gaz (AGR) pour des températures de services proches de 550°C. Cependant, à ce jour, aucun cas de FER n'a été observé dans des conditions similaires avec des aciers de type 316L. Il est néanmoins important de rechercher les conditions thermomécaniques pouvant mener à la FER dans ces aciers pour garantir l'intégrité de futurs composants soudés utilisés, par exemple, dans des RNR-Na.

Les études menées depuis les années 50 ont montré que la fissuration en relaxation se développe entre 500 et 700°C en présence de fortes contraintes résiduelles de traction dans les zones ayant subies une déformation plastique due aux incompatibilités de déformation thermiques lors du procédé de soudage. Pour des conditions thermo-mécanique similaires, il a été observé que les aciers de la famille des 316 (i.e. 316H, L et L(N)) peuvent avoir des résistances à la FER drastiquement différentes. Ces différentes résistances pourraient impliquer le rôle de la composition chimique des aciers, et tout particulièrement leur teneur en C, N et P, qui sont supposés influer : (i) sur la cinétiques de dégradation des joints de grains associées à la précipitation intergranulaire de carbure et à la ségrégation intergranulaire d'impuretés comme par exemple le phosphore et/ou (ii) sur la cinétiques de relaxation des contraintes résiduelles. De plus, le niveau des contraintes résiduelles pouvant mener à la FER, ainsi que l'effet de la température de service ne sont pas connus pour les aciers de type 316L. Les objectifs de cette thèse doctorale peuvent donc se résumer à :

- *identifier les caractéristiques des aciers de type 316L et les forces motrices responsables de la FER,*
- *améliorer la compréhension du rôle de la composition chimique et des conditions thermo-mécaniques sur les mécanismes responsables de la FER,*
- *développer un cadre numérique basé sur les observations et les mesures expérimentales permettant de décrire et de prédire la FER dans les aciers de type 316L.*

Afin de répondre à ces objectifs, la démarche retenue consiste à reproduire la FER dans cinq alliages de type 316L sélectionnés pour leurs compositions chimiques différentes en C, N et P. Pour ce faire, de forts champs de contraintes résiduelles de traction sont introduit par un cycle mécanique de compression dans la région du fond d'entaille d'éprouvette dont la géométrie est proche de celle du type CT. Par la suite, ces éprouvettes subissent un traitement thermique de relaxation entre 550 et 600°C pendant 1 à 6 mois.

Ensuite, l'endommagement intergranulaire potentiellement présent dans les éprouvettes est analysé et quantifié par MEB, EBSD et tomographie X de synchrotron. La comparaison entre les résistances à la FER des aciers testés devrait permettre d'évaluer les effets respectifs du carbone de l'azote et du phosphore sur le développement de ce type d'endommagement.

L'approche proposée pour évaluer les conditions thermo-mécaniques nécessaires à la FER dans ces aciers consiste à comparer les distributions d'endommagement dans les éprouvettes avec des prédictions numériques de déformations et de contraintes résiduelles dans ces même zones. Finalement, la calibration de l'évolution d'une variable d'endommagment scalaire qui peut être calculée dans un post-processing de calcul éléments finis devrait permettre de reproduire les distributions d'endommagement dans les éprouvettes et de consistituer un outil permettant la prédiction de la FER dans les aciers de type 316L.

Contents

1.1 Context

1.1.1 Industrial context

Austenitic stainless steels exhibit good oxidation and high temperature corrosion resistance, mechanical properties at low and high temperatures (up to about 600°C) and offer a good weldability with conventional processes. For these reasons, they are widely used in the chemical and power generation industries. In particular, AISI 304L austenitic stainless steels have been used in the

[1] Cette thèse de doctorat est écrite en anglais. Cependant, un résumé en français de chaque chapitre est proposé au début de ceux-ci.

French fleet of pressurized water reactors (PWRs) including tubing and pipework subjected to service temperatures close to 320°C. In fast neutron reactors, which are potential candidates to complement French PWRs, AISI 316L-type austenitic stainless steels are considered as structural materials which could be used at temperatures close to 550°C. At these temperatures, international operational experience revealed the existence of intergranular damage, known as reheat cracking (RC), that can be found near the weld joints of some large austenitic stainless steel welded components. Such damage phenomenon has been widely reported in the UK advanced gas-cooled reactor (AGR) welded structures produced from AISI 316H austenitic stainless steels (Coleman et al., 1998). In the past, large welded AISI 316L-type austenitic stainless steel components have been used close to 550°C in the French small-scale prototype of a fast neutron reactor, Phénix, and the associated full-size nuclear power station, Superphénix. However, no reheat cracking damage was reported during service in these reactors and, more generally, in AISI 316L-type steels. Nevertheless, a study of the thermo-mechanical conditions responsible for reheat cracking in AISI 316L-type steels is needed to ensure the integrity of potential future power plants operating at temperatures close to 550°C during typical lifetimes of ∼60 years.

1.1.2 Scientific context

Reheat cracking, also known as stress relaxation cracking or stress relief cracking, is an intergranular damage phenomenon which can potentially be found in heat affected zones (HAZ) of large welded parts after either post-weld heat treatment or service in the 500-700°C temperature range. This phenomenon is known to be driven by the high temperature relaxation of residual stress fields which are initially introduced during welding as a result of thermal strain and deformation incompatibilities. These incompatibilities depend on the weld configuration and on the component thickness, as industrial RC cases are typically known to occur near attachment welds where the cross-sectional thickness is above 30-40 mm (Coleman et al., 1998; Dhooge, 1998). Reheat cracking development was not found to require external applied loadings and can result in macroscopic intergranular cracks despite the low equivalent viscoplastic strain typically associated with residual stress relaxation ($<\sim 1\%$). Such macroscopic cracks are known to result from the formation of intergranular microcavities that grow and coalesce to form intergranular microcracks which subsequently join up to form macroscopic cracks such as those shown in Figure 1.1.

Previous studies have shown that the regions affected by reheat cracking were strain hardened during the welding process (Auzoux, 2004; Auzoux et al., 2010; Bouchard et al., 2004). Although the level of plastic deformation that can be attained depends on the welding configuration and process, a value of approximately 10-20% cumulated plastic strain can develop a few millimeters from the fusion boundary in austenitic stainless steels (Auzoux et al., 2010; Turski et al., 2008). Furthermore, pre-deformation was found to be necessary to induce the right conditions for reheat cracking damage development in austenitic stainless steels (Auzoux et al., 2010; Chabaud-Reytier et al., 2003). From a micromechanical point of view, the pre-deformation is generally assumed to induce extensive local residual stress concentration at grain boundaries (GBs) which favor intergranular microcavity nucleation and thus intergranular damage development (Auzoux, 2004). Under creep conditions, high levels of stress triaxiality are known to reduce austenitic stainless steel ductility (Skelton et al., 2003; Spindler, 2004a). However, under RC (*i.e.* stress relaxation) conditions, similar stress triaxiality effect has not been thoroughly

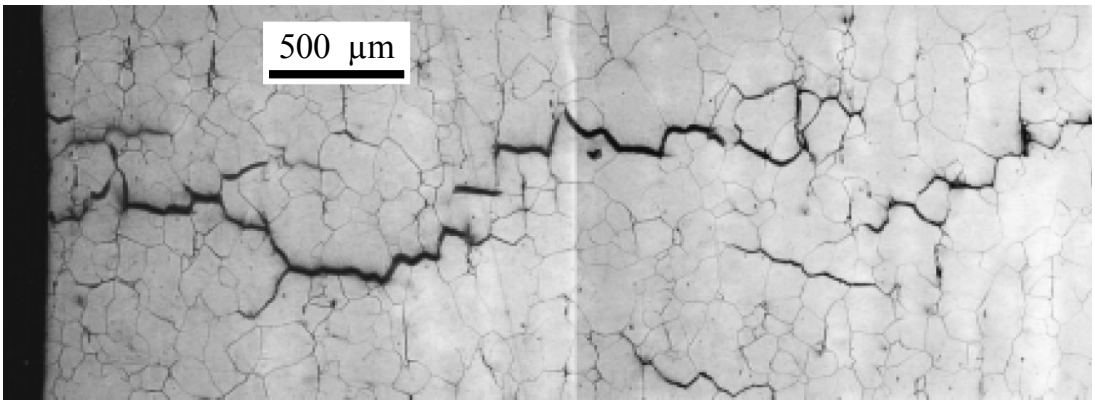

Figure 1.1: Optical micrograph of a region showing a macroscopic intergranular crack identified as reheat cracking damage in a AISI 316H welded component (at ∼5 mm from the fusion line) after 50 000 hrs at 500°C (Auzoux, 2004).

studied.

It is generally established that the limitation of reheat cracking occurrence can be obtained by controlling the welding process in order to reduce the levels of pre-deformation and residual stresses (*e.g.* (Coleman et al., 1998)). However, under the same conditions, a comprehensive understanding of the different reheat cracking resistance of chemically-close AISI 316-type steels is lacking (Auzoux, 2004). Those different resistances may involve (i) GB degradation kinetics associated to intergranular carbide precipitation and intergranular segregation of impurities such as phosphorus and/or (ii) residual stress relaxation kinetics. Furthermore, the critical residual stress magnitude that can lead to reheat cracking, as well as the effect of temperature on the development of reheat cracking damage, have not been quantified in AISI 316L-type austenitic stainless steels.

1.2 Objectives

The main objectives of this doctoral thesis can be defined as follows.

- To identify the material and microstructural characteristics as well as the driving forces responsible for reheat cracking damage development in AISI 316L-type austenitic stainless steels.

- To gain an understanding about the role of alloying element and the thermo-mechanical conditions on the mechanisms of reheat cracking in AISI 316L-type austenitic stainless steels.

- To develop a physics-inspired constitutive material modelling framework based on the experimental observations and measurements to predict the reheat cracking damage development in AISI 316L-type austenitic stainless steels.

1.3 Methodology

The study of reheat cracking in real components is not practical due to their typical dimensions. Consequently, since the 50's, the development of procedures based on simple laboratory-size specimen suitable for reheat cracking studies has received increased consideration. In the past, the most common method involved the production of Borland welded specimen (Borland, 1960; Spindler, 2004b). However, the assessment of the testing conditions in welded specimen are particularly challenging due to the complex thermo-mechanical loadings and microstructure evolutions associated with the welding process. Thus, since the early 2000's, experimental methods have been devised to study reheat cracking under closely controlled laboratory conditions (Hossain et al., 2007, 2010; Turski et al., 2008). In this work, the methodology chosen to reproduce reheat cracking is based on the work by Turski et al. (2008), who proposed a procedure to introduce a tensile residual residual stress field in the notch root region of a CT-like specimen. The advantages of this technique is that it enables (i) an homogeneous microstructure to be studied and (ii) the possibility to predict the residual stress and strain fields initially present in the specimen, as well as their subsequent high temperature relaxation with a suitable constitutive model. Some of the tested AISI 316L-type austenitic stainless steels are expected to be much more resistant to intergranular cracking at high temperatures than the ones tested in previous studies (Argence and Pineau, 1995). Consequently, since high pre-deformation level is known to extent RC, the tested materials will be pre-deformed by 20% cold rolling in order to ensure that sufficient reheat cracking damage will be generated during the CT-like specimen thermal exposures.

Five different AISI 316L-type austenitic stainless steels which differ from their chemical compositions are studied experimentally. Two of them with controlled phosphorus contents were specially casted for this work while the others are industrial grades. The experimental programme involves the testing of those steels under reheat cracking (*i.e.* residual stress relaxation) conditions at 550, 575 and 600°C for one to six months to study the effect of temperature and thermal exposure duration. After thermal exposure, the potential intergranular damage present in the specimens are analysed using SEM coupled with EBSD. Furthermore, a novel approach proposed in this work relies in the use of X-ray synchrotron tomography to quantify in 3D the level of intergranular damage potentially present in the specimens which should provide a better statistical significance for the damage distributions. A comparison between the reheat cracking resistance of the five steels are carried out to enable the effect of some alloying elements on the reheat cracking damage development in the 500-600°C temperature range to be assessed. A focus is placed on the C, N and P contents as those elements are assumed to significantly affect GB degradation kinetics (C and P) and residual stress relaxation kinetics (N).

An analysis of the mechanical conditions that led to reheat cracking in the specimens is necessary to re-examine the mechanical driving force responsible for reheat cracking. Thus, the proposed approach is to numerically predict the local residual stress and strain fields in the specimens numerically using non-linear FE techniques. For this purpose, a novel viscoplastic constitutive model is proposed. It relies on internal state variables explicitly linked to microstructure related length scales. A comparison between the predicted residual stress fields in the CT-like specimens and the intergranular damage distributions measured by X-ray synchrotron tomography is made to infer the threshold level of local residual stresses associated with the initiation of stress relaxation micro-cracks.

Finally, the distribution of the measured local reheat damage is modelled numerically by linking, in a sequential manner, an existing evolutionary relation for a scalar damage variable,

with the predicted stress and strain fields obtained from the proposed viscoplastic constitutive model.

1.4 Thesis outline

The thesis is divided into three main parts which correspond to submitted, or about to be submitted, papers.

First, the work concerning the experimental investigations of reheat cracking in the five AISI 316L-type austenitic stainless steels is presented in Chapter 2. Intergranular damage is observed in the mid-thickness of the tested CT specimens and a comparison between the five steel resistances to RC is carried out. Furthermore, the effect of chemical composition, temperature and residual stress magnitude on reheat cracking damage development is studied and discussed.

Next, the novel viscoplastic constitutive model used to predict the residual stress field evolutions in the specimens is presented in Chapter 3. The constitutive model is formulated assuming large strain kinematics, calibrated from AISI 316L-type steel data mainly obtained in this work, and is then implemented numerically into the finite element method. It is then applied to the prediction of the residual stress relaxation in the notch root regions of the CT-like specimens from room temperature up 550-600°C.

Then, Chapter 4 presents the modelling of the experimental damage distributions found in the specimens using an evolutionary relation for a scalar damage variable. The effects of the predicted initial residual stress magnitude, as well as the testing temperature, on the damage distributions found experimentally are reproduced with the damage law which provides a useful estimation of the RC propensity in AISI 316L-type steels.

Finally, the conclusions of this work and the prospects for future researches are presented in Chapter 5.

CHAPTER 2

Experimental study of stress relaxation cracking

Résumé

Ce chapitre concerne l'étude des mécanismes responsables de la fissuration en relaxation (FER) des aciers de type AISI 316L. Ce phénomène, aussi connu sous le nom de « reheat cracking », se retrouve typiquement dans les zones affectées par la chaleur de composants industriels massifs soudés puis réchauffés à des températures de service proches de 550°C. Ici, cinq aciers de type 316L à différentes par leurs teneurs en C, N et P sont testés afin d'évaluer les effets de la composition chimique sur trois mécanismes affectant potentiellement la FER: (i) la précipitation intergranulaire de carbures $M_{23}C_6$, (ii) la cinétique de relaxation des contraintes résiduelles et (iii) la ségrégation intergranulaire du phosphore. Après avoir testé ces cinq aciers de type 316L dans des conditions de FER en utilisant des éprouvettes dont la géométrie est proche de celle de type « Compact Tension », différent niveaux d'endommagement intergranulaire ont été observés par microscopie optique et par tomographie X de synchrotron. Des analyses détaillées au MEB et au MET ont montrées que le mécanisme dominant pour la FER est la nucléation de microcavités à l'interface entre les carbures intergranulaires $M_{23}C_6$ et les grains adjacents situés dans les régions de fortes contraintes résiduelles. Il a également été déduit que l'ajout de phosphore augmente le nombre de joints de grains présentant des microcavités intergranulaires. Finalement, la comparaison entre les prédictions des champs de contraintes résiduelles dans les éprouvettes de type CT et l'endommagement observé par tomographie X de synchrotron a permis de déduire un niveau seuil de contrainte résiduelle principale, σ_I, de 740 ± 40 MPa au dessous duquel la FER n'apparaît pas pour les cinq aciers testés. Dans ce chapitre, les prédictions de contraintes résiduelles dans les éprouvettes ont été obtenus par des calcul éléments finis décrits dans le chapter 3. De plus, bien que des résultats de mesures d'endommagement par tomographie X de synchrotron soient utilisés, une description plus détaillée de la procédure de mesure associée à cette technique est disponible au chapter 4. Des résultats complémentaires sur l'évolution in situ de l'endommagement intergranulaire mesuré par tomographie en fonction du chargement mécanique de traction appliqué sont présentés en annexe Appendix C. Ce chapitre est adapté d'un article publié dans Acta Materialia (Pommier et al., 2016).

This chapter deals with the experimental investigations performed to study reheat cracking in five AISI 316L-type austenitic stainless steels. Intergranular damage is observed and a compari-

son between the five steel resistances to reheat cracking is carried out. Furthermore, the effect of the chemical composition, temperature and residual stress magnitude on reheat cracking damage development is studied and discussed. The specimen stress and strain field predictions presented in this chapter are obtained from finite element simulations detailed in chapter 3. Furthermore, some damage measurement results obtained by synchrotron X-ray tomography are shown but a more detailed description of the associated procedure is presented in chapter 4 and Appendix C. This work is adapted from a paper accepted for publication in *Acta Materialia* (Pommier et al., 2016).

Abstract

This work concerns a study of the mechanisms responsible for intergranular cracking during high temperature stress relaxation in AISI 316L-type austenitic stainless steels. This phenomenon, also known as reheat cracking, is typically present in heat affected zones of massive welded parts used in the energy industry. Here, five steel grades with different C, N and P contents were considered to assess the effects of chemical composition on the three main mechanisms potentially responsible for reheat cracking, namely intergranular $M_{23}C_6$ carbide precipitation, stress relaxation phenomena, and intergranular P segregation. After testing the five AISI 316L-type grades under reheat cracking conditions by a pre-compressed CT-like specimen technique, different degrees of intergranular damage were observed in the specimens by optical microscopy and synchrotron X-ray tomography. Detailed grain boundary analyses by SEM and TEM in the five different steel grades showed the main mechanism responsible for reheat cracking to be the nucleation of microcavities at intergranular $M_{23}C_6$ carbides in high residual stress regions. The addition of P was found to increase the number of cavitated GBs but not to be the dominant mechanism responsible for intergranular damage. A comparison between elasto-plastic finite element predictions of the residual stresses in the CT-specimens and the results of microstructural investigations revealed no intergranular damage in regions where the initial maximum principal stresses in the specimens were below 740 ± 30 *MPa.*

Contents

2.1 Introduction

Reheat cracking (RC), also known as stress relaxation or stress relief cracking, is an intergranular damage phenomenon found in heat affected zones (HAZ) of thick welded parts (*e.g.* steam header/nozzle in Advanced Gas Cooled Reactors (Bouchard et al., 2004)). Some of the materials which exhibit such mode of failure are austenitic stainless steels reheated at high temperatures (773-973 K) during either post-weld heat treatment or service. Such intergranular damage is known to be driven by the high temperature relaxation of residual stress fields initially introduced during the welding process due to thermal strain incompatibilities. These incompatibilities depend on the weld configuration and on the component thickness, as industrial RC cases are typically known to occur near attachment welds where the cross-sectional thickness is above 30-40 mm. The main objective of this work is to investigate the effects of C, N and P contents on RC damage development in AISI 316L-type austenitic stainless steels.

In the mid-fifties, the first in-service cases of RC were described and studied on stabilised austenitic stainless steels[1] (Curran and Rankin, 1957; Emerson and Jackson, 1957; Younger and Baker, 1960; Younger et al., 1963). Massive welded pipes of 347 and 321 steel grades (Nb and Ti-stabilised austenitic stainless steels, respectively) were found to be prone to RC during high temperature service. 304-type and 316-type non-stabilised austenitic stainless steels, which do not exhibit intragranular precipitation of Ti or Nb-carbides, were found to be less sensitive to RC (Meitzner, 1975), but not immune to, as this phenomenon was observed in 304H (Cabrillat et al., 2001; Van Wortel, 1998) and 316H (Bouchard et al., 2004; Coleman et al., 1998). More recently, 316L and 316L(N) steels (Auzoux et al., 2005, 2010) were found to be sensitive to intergranular cracking under reheat cracking conditions. However, as far as the author is aware, no evidence of in-service RC has been reported in 316L-type steels.

The main mechanical condition for RC to occur was found to be the presence of high tensile residual stress fields in the material before thermal exposure at high temperatures. During the welding process of massive parts, thermal strain incompatibilities induce the formation of predeformed zones and the development of residual stress fields near the weld. The level of residual stresses required to develop RC in annealed austenitic stainless steels was found to be only attainable by strain hardening (Auzoux et al., 2010; Chabaud-Reytier et al., 2003). Besides, high stress triaxialities were also found to increase RC damage (Spindler, 2004a). Those observations are consistent with the lower creep ductility observed in austenitic stainless steels on predeformed states (Auzoux et al., 2005; Moen and Smith, 1975; Willis et al., 1999; Wilshire and Willis, 2004) and subjected to high stress triaxialities (Skelton et al., 2003; Spindler, 2004a).

Several mechanisms were suggested to explain the RC susceptibility of predeformed austenitic

[1] Thereafter, the AISI numbering system is implicitly assumed when designating 300 series steels.

stainless steels. In 347 and 321 steels, it was first attributed to strain-induced precipitation hardening due to Nb(C,N) and Ti(C,N) carbides (Dhooge, 1998; Dhooge and Vinckier, 1987; Thomas, 1984; Younger et al., 1963). However, Chabaud-Reytier *et al.* (Chabaud-Reytier et al., 2003) suggested that intragranular Ti(C,N) carbide precipitation was not the predominant mechanism responsible for RC in 321 steel. Instead, they attributed this mode of failure to solute solid solution atoms (C and N) which impede the mobility of dislocations and thus reduce the residual stress relaxation rate. Those solid solution atoms can explain the susceptibility of non-stabilised austenitic stainless steels to RC, and also suggest that the grades with high solute atom contents would be more sensitive than low content ones. This understanding was not confirmed by the observations of Auzoux *et al.* (Auzoux et al., 2010) on 316H, 316L(N) and 316L steels exposed to RC conditions. They found that the global content of solute atoms cannot explain the various sensitivities of 316-type grades to RC since the tested 316L (low C and low N) was found to be the most prone to RC. Thus, the respective effects of C and N contents in solid solution are still unclear.

Another mechanism known to be responsible for intergranular damage in austenitic stainless steel is intergranular carbide precipitation. During service at temperatures close to 823 K, grain boundary (GB) strength can be impaired by the precipitation of intergranular carbides (mostly, Fe(Cr,Mo)-rich $M_{23}C_6$) which is accelerated by prior room-temperature (RT) deformation (Weiss and Stickler, 1972). More recently, Hong *et al.* (Hong et al., 2001) and Jones *et al.* (Jones et al., 2008) investigated the relationship between GB characteristics and the formation of intergranular $M_{23}C_6$ carbides in austenitic stainless steels. They concluded that the presence of $M_{23}C_6$ depends on GB type: highly random misoriented GBs exhibit more carbide precipitation than $\Sigma 3$ boundaries. Besides, the shape of intergranular carbides is linked to GB characteristics: as misorientation between adjacent grains increases, the carbide morphology tends to change from plate-like to acute triangular shapes. The latter $M_{23}C_6$ carbide morphology can explain the more pronounced cavitation observed on random highly misoriented GBs during creep at high temperature (Hong and Nam, 2003; Hong et al., 2001; Kim et al., 2004).

A third mechanism which can potentially affect the cohesive strength of GBs, and hence RC, is the intergranular segregation of impurities such as S and P (Hong et al., 1986). In comparison with P, intergranular S segregation is less important in austenitic stainless steels (Briant, 1987a) due to the formation of non-metallic MnS inclusions during hot-rolling. Sulphur is thus unlikely to affect creep cavitation in 316L-type austenitic stainless steels. Similarly to intergranular carbide precipitation, GB misorientations can also affect intergranular segregation levels. For instance, it was observed that $\Sigma 3$ GBs present less P segregation than other types in Fe-Cr-Ni (Ogura et al., 1987) and Fe-Mn-C steels (Herbig et al., 2015).

The mechanisms of intergranular $M_{23}C_6$ carbide precipitation and P segregation can affect each other. Kegg *et al.* (Kegg et al., 1974) showed that P segregation accelerates both the nucleation and growth rate of $M_{23}C_6$ carbides. Their propensity to reduce GB strength was reported by Chen *et al.* (Chen et al., 2010). At 77 K, the intergranular fracture surface of 316H austenitic stainless steel was found to be an increasing function of intergranular $M_{23}C_6$ carbide coverage and intergranular P content. Even if a correlation exists, the relative effects of $M_{23}C_6$ carbide precipitation and P segregation on GB strength is still unclear.

The above literature review shows that RC occurs during the relaxation at high temperatures of the high tensile residual stresses initially introduced during plastic deformation of the material. However, the dominant micromechanisms responsible for grain boundary weakening at high temperatures are still not fully understood. This includes the role of $M_{23}C_6$ carbide precipitation, the effects of C and especially N contents on stress relaxation kinetics, as well as

the effect of intergranular P segregation.

Several published works have dealt with the development of experimental methods to reproduce stress relaxation cracking at the laboratory scale (Borland, 1960; Hossain et al., 2007, 2010; Sherry et al., 2002; Spindler, 2004b). The procedure developed by Turski *et al.* (Turski et al., 2008), which consists of introducing a triaxial tensile residual stress field at the notch root of a CT-like specimen by precompression at RT, enables the magnitude of the maximum residual stress in the notch root region to be controlled. This approach also makes it possible for stress relaxation cracking of homogeneous microstructures to be studied under known residual stress fields. The method to be used in this work is based on this pre-compressed CT technique.

The paper is structured as follows. First, three industrial steel grades (various C and N contents, similar P contents) and two laboratory-made grades (similar C and N contents, one with high P, another with very low P) are described. Then, the RC experimental procedure of pre-compressed CT-like specimen is explained. Afterwards, the mechanical response of the materials at room and high temperatures is investigated, characterised and modelled to predict the residual stress and strain fields in the CT specimens. The results of RC experiments, conducted on the five 316L-type grades, are next presented. In this part, the resulting intergranular damage is quantitatively studied using optical and scanning electron microscopy (OM and SEM), electron back scatter diffraction (EBSD), transmission electron microscopy (TEM) and local X-ray synchrotron tomography techniques. Finally, the effects of temperature, C, N and P on RC damage development are discussed. The resulting conclusions are then used to explain the different resistances of the five 316L-type steel to RC.

2.2 Materials and experimental procedures

2.2.1 Materials

The chemical compositions of the five 316L-type austenitic stainless steels are given in Table 2.1 (except for C, N and P, the precise compositions are not given for industrial confidentiality). Here, IA, IB and IC are designations of industrial grades that were received in annealed states (respectively at 1373, 1323 and 1373 K, for 30, 30 and 90 min before being water quenched), in the form of 14, 40 and 33 mm-thick sheets. Laboratory-made high P (HP) and low P (LP) steels were specially cast for this study by Ugitech and hot-rolled at 1385±15 K into 30 mm-thick sheets by OCAS. Upon receipt, they were annealed at 1373 K for 10 min and water quenched to obtain a grain size similar to that of industrial grades. The grain size of the five steel grades was found to be 40 ± 6 μm. The five annealed microstructures were composed of equiaxed austenitic grains containing annealing twins and showed no crystallographic texture. A microstructure representative of the five steel grades in the annealed state is shown in Figure 2.1(a) (RD and TD stand for, respectively, (hot-)rolling and transverse directions). The five material microstructures are shown in Appendix A. MnS intragranular inclusions, which are aligned and elongated along the RD, were observed in all grades, especially in IA which has a higher S content. Their chemical compositions were confirmed by energy-dispersive X-ray spectroscopy (EDS).

The annealed plates were then cold-rolled in the same direction as the original hot-rolling one to reduce their thickness by 20±2%. For the five grades, Vicker's hardness increased from 135-208 HV_{30} in the annealed state to 274-282 HV_{30} in the cold-rolled state. The latter hardness values are higher than the maximum value of 230 HV_{30} measured by Auzoux (Auzoux, 2004) in the most highly deformed zone of a multi-pass weld. Therefore, the use of this five cold-

rolled materials for the RC studies should enable the residual stress fields to be introduced to be greater than the ones found in industrial parts. It should be noted that the microstructure of the five cold-rolled materials is different than the one observed in industrial RC-affected zones since deformation twins were observed (see Figure 2.1(b)). The absence of deformation twins in industrial RC-affected zones is due to the higher temperature of deformation (~923 K (Auzoux, 2004)) during welding. Furthermore, SEM observations of the cold-rolled materials revealed no grain boundary damage (*e.g.* microcavities), at least whithin the peak resolution of the SEM used in this work [2].

Table 2.1: Chemical compositions of the AISI 316L-type steels (wt.%).

	IA	IB	IC	HP	LP
C	0.033	0.028	0.011	0.014	0.014
N	0.025	0.077	0.068	0.081	0.066
P	0.022	0.023	0.028	0.052	0.001
Cr	←		16.4 - 17.4	→	
Ni	←		11.0 - 13.6	→	
Mo	←		2.0 - 2.6	→	
Mn	←		0.8 - 2.1	→	
S	←		0.001 - 0.022	→	
B	←		0.001 - 0.002	→	
Fe	←		bal.	→	

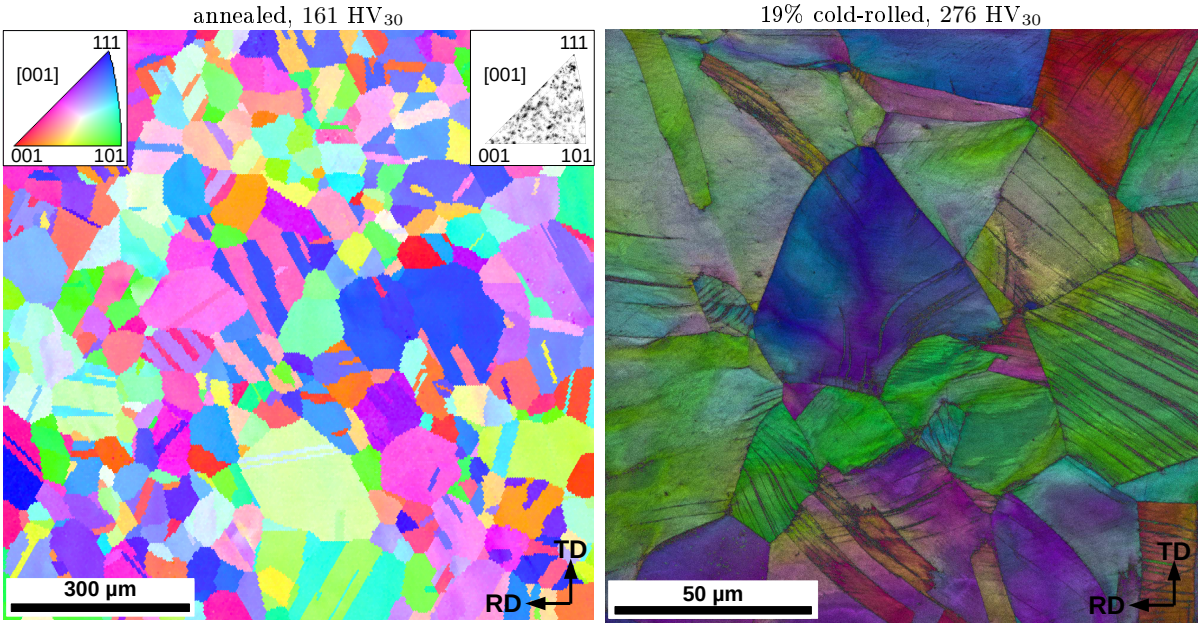

(a) (b)

Figure 2.1: Microstructure of the IB steel grade observed by EBSD: (a) annealed state shown in an inverse pole figure (IPF) and (b) cold-rolled state, in a close-up view, shown by a superposition of the IPF and image quality maps.

[2] FEI Nova NanoSEM 450 S-FEG SEM.

2.2.2 Reheat cracking reproduction procedure

Reheat cracking was reproduced at a laboratory scale using CT-like specimens cut by wire-EDM from the cold-rolled plates (see geometries in Figure 2.2(a)). Two CT specimen thicknesses (e=10 and 20 mm) were used depending on the available plate thicknesses. To study the effect of mechanical conditions on RC damage development, three notch radii (r=0.5, 1 and 2 mm) were tested for the IB grade steel. In Figure 2.2, the notch plane (XZ) is normal to the RD (Y-direction) to maximise the residual stresses to be introduced in the specimens. The specimen thickness and notch radius values are given in Table 2.2. In this work, the residual stress fields in the CT-like specimens were introduced by mechanical loading rather than by the thermal strain incompatibilities associated with the welding of actual thick industrial components. Here, the replication of typical component thicknesses was not assumed to be necessary to obtain the required level of residual stresses since high residual stress levels are obtained by mechanical loading. Furthermore, the CT specimen thicknesses (10-20 mm) remain large in comparison to early reheat crack sizes (*i.e.* of the order of the grain size (Turski et al., 2008)).

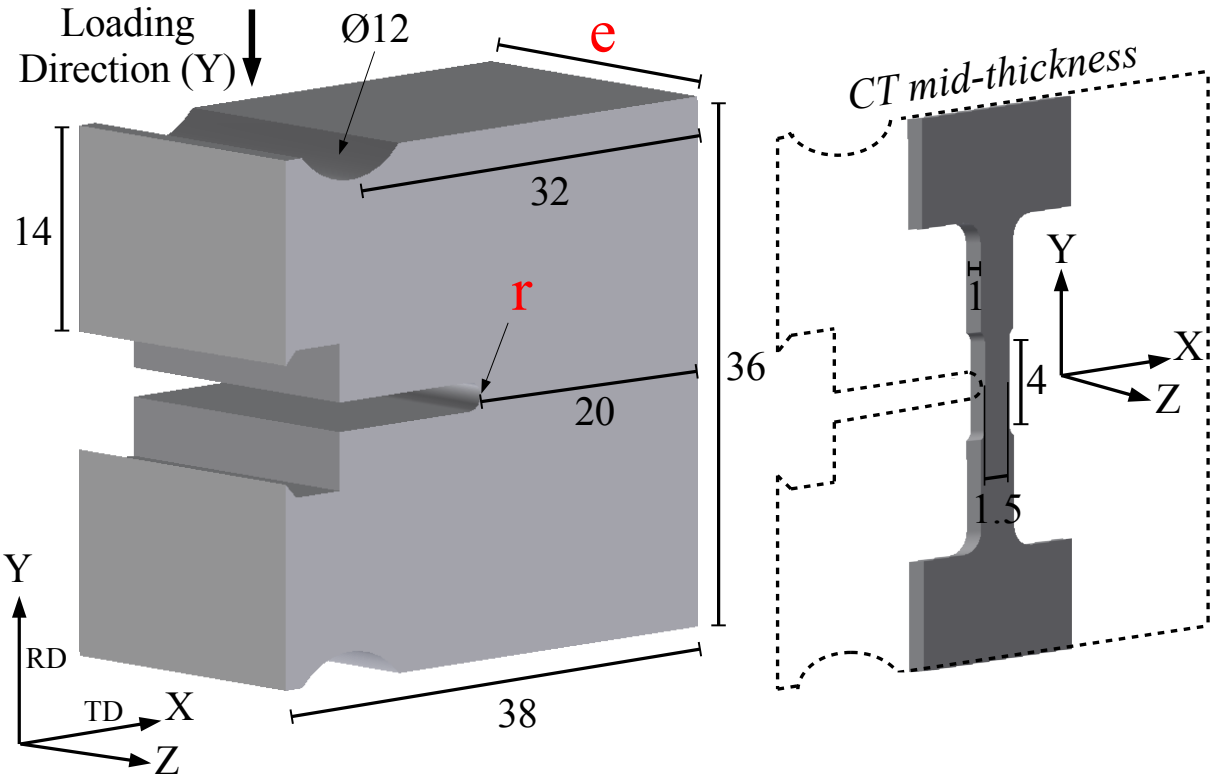

(a) (b)

Figure 2.2: (a) CT-like specimen geometries in mm, e ∈ {10,20} and r ∈ {0.5,1,2} (see Table 2.2) and (b) *in situ* tensile specimen machined from the CT specimen mid-thickness for SEM and synchrotron tomography studies.

The RC reproduction procedure consists of two steps:

(i) *Residual stress introduction*
Residual stresses were introduced in CT-like specimens by RT compression along the Y-direction (RD, see Figure 2.2(a)) using geometrically-adapted cylindrical-headed fixtures

and a 100 kN servo-hydraulic testing machine. Compressing forces of 25 and 50 kN were applied to the 10 and 20 mm-thick CT specimens, respectively. Thus, a confined plastically deformed zone was introduced in the notch root region. Upon unloading, the self-equilibrating elastic strains in the specimen led to the formation of a tensile residual stress field in the plastically deformed zone.

(ii) *Residual stress relaxation at high temperature*
Afterwards, the CT specimens were thermally exposed to constant temperatures of either 823, 848 or 873 K in resistance furnaces for 500-4313 hrs (about 1-6 months). The specimens were then removed from the furnace and air-cooled to RT. The testing conditions of each CT specimen are given in Table 2.2.

2.2.3 Microstructural characterisation techniques

After their thermal exposures, the CT specimens were cut through their mid-thicknesses (XY plane) by wire-EDM. One of the resulting mid-thickness surfaces was polished and analysed by optical microscopy, SEM and EBSD. A FEI Nova NanoSEM 450 microscope (field emission gun) coupled with an EDAX TSL Hikari camera running with OIM system was used for EBSD data acquisition. The acceleration voltage was 20 kV, the working distance was close to 14 mm and the step size was 100 nm following an hexagonal grid. In order to reveal intergranular microcavities or microcracks while minimising the risk of dislocating grain boundary carbides, mechanical polishing with grinding papers (from 40 to 3 μm) and diamond pastes (from 3 to 1 μm) was performed, followed by a light etching with a solution of colloidal silica during 5 min.

The remaining half specimen was used to machine tensile specimens for either *in situ* synchrotron X-ray tomography or *in situ* SEM observations. Their geometry and the area from which they were machined are shown in Figure 2.2(b). The tensile specimens from IA and IC grades were monotonically deformed *in situ* in a SEM chamber along the Y-direction by 10±1% true strain. They were then 3D scanned by synchrotron X-ray tomography at the European Synchrotron Radiation Facility (ESRF, line ID15a). The scanned total volume was 1550x1750x1000 μm^3, and it was subsequently reconstructed from 2000 projections. The acquisition of projected images was performed with a filtered white beam centered around a 60 keV X-ray energy. Tensile specimens from IB, HP and LP grades were incrementally deformed *in situ* at the ESRF with a tensile testing device specially designed for local tomography (Landron et al., 2011). The tensile specimens were incremently deformed from 0 to 20±3% true strain along the Y-direction while performing a 3D tomography scan at each strain step (see Appendix C, further information about synchrotron tomography and *in situ* tensile tests can be found in (Kahziz, 2016; Landron, 2012)). The deformation along the Y-direction was carried out to open up any existing microcavities and microcracks by plastic deformation. When the size of a defect exceeded the tomography voxel size (*i.e.* for this experiment, 1.095 μm), the defect could be detected.

To identify the chemical composition and structure of the intergranular carbides present in the CT specimens after thermal exposures, TEM observations were performed on a thin disc-shaped section machined from the IB grade specimen tested at 848 K for 3621 hrs (e=20 mm, r=1 mm). The sample was cut by wire-EDM out of the former tensile residual stress region so that early stage of intergranular damage development (*i.e.* nanocavities) could possibly be observed.

2.3 Mechanical analyses

2.3.1 Cold-rolled material responses

The mechanical responses of the five cold-rolled materials were obtained by an up to 5% compressive true strain followed by a 10% tensile deformation to describe the loading path experienced by the region ahead of the notch of CT specimens when compressed and then unloaded. Those tests were performed on axisymmetric specimens with a round section of 8 mm diameter and machined along the RD. A 100 kN servo-hydraulic machine was used and a strain rate of 10^{-3} s^{-1} was applied during the tests. Figure 2.3 shows that the mechanical responses of the five cold-rolled materials at RT are similar.

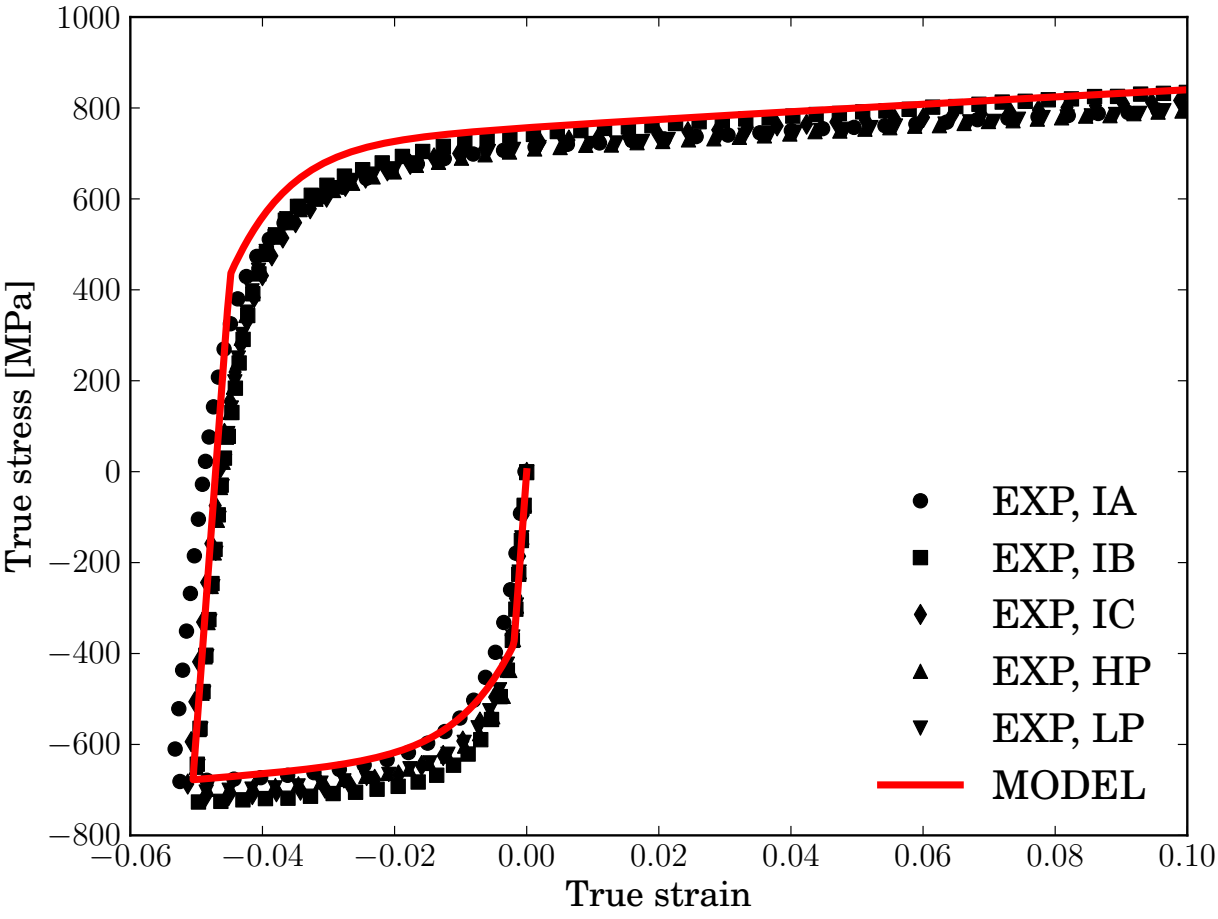

Figure 2.3: Stress/strain responses at RT of the five cold-rolled materials (MODEL describes the predicted behaviour to be discussed later in the text).

2.3.2 Prediction of CT specimen residual stress and strain fields

Finite element simulations were carried out using the commercial Z-set software (Zset, 2015) to predict the residual stress and strain fields in the CT specimens. The constitutive model used to describe the mechanical behaviour of 316L-type steels, implemented into the Z-set code as a user-defined material subroutine, relies on internal variables associated with evolving microstructural length scales (*i.e.* mean dislocation and twin spacings) and a tensorial back stress. The

main functional form of the viscoplastic constitutive model's flow and evolutionary relations are presented next. For the full formulation, refer to chapter 3.
The finite strain hypo-elastic formulation is expressed in terms of the Jaumann rate of the Kirchhoff stress tensor as:

$$\overset{\triangledown}{\mathbf{T}} = \mathcal{L} : (\mathbf{D} - \mathbf{D}^p) \tag{2.1}$$

where, $\mathbf{D}$ and $\mathbf{D}^p$, are the total deformation rate and the viscoplastic deformation rate tensors, respectively, and $\mathcal{L}$ is the fourth order isotropic elasticity tensor.
The equivalent viscoplastic strain rate, $\dot{\tilde{\epsilon}}^p$, can be written in its functional form in terms of the Kirchhoff stress tensor, $\mathbf{T}$, the absolute temperature, θ, and three microstructure-related internal variables: a mean dislocation density, ρ, the volume fraction of twins, f, and a tensorial internal stress or back stress tensor, $\mathbf{B}$. Then,

$$\dot{\tilde{\epsilon}}^p = \dot{\tilde{\epsilon}}^p\{\mathbf{T}, \theta, \rho, f, \mathbf{B}\} \tag{2.2}$$

The above equation defines the magnitude of the inelastic flow, which combined with its direction, completes the relation for the inelastic deformation rate tensor,

$$\mathbf{D}^p = \frac{3}{2}\dot{\tilde{\epsilon}}^p \frac{(\mathbf{T}' - \mathbf{B})}{\tilde{\sigma}^e} \tag{2.3}$$

where, $\mathbf{T}'$, is the deviatoric component of the Kirchhoff stress tensor and the equivalent effective stress, $\tilde{\sigma}^e = \sqrt{\frac{3}{2}(\mathbf{T}' - \mathbf{B}) : (\mathbf{T}' - \mathbf{B})}$.
Furthermore, the equivalent viscoplastic strain rate, $\dot{\tilde{\epsilon}}^p$, is assumed to be composed of a contribution due to the slip arising from dislocation motion in the untwinned material, $\dot{\tilde{\epsilon}}^p_g$, and due to mechanical twinning. Here,

$$\dot{\tilde{\epsilon}}^p = (1 - f)\dot{\tilde{\epsilon}}^p_g + \frac{\gamma_p}{\sqrt{3}M}\dot{f} \tag{2.4}$$

where, γ_p, is the shear deformation induced by the slip of a partial dislocation, and, M, the Taylor factor which accounts for the polycrystalline nature of the microstructure. The viscoplastic strain rate component due to slip, $\dot{\tilde{\epsilon}}^p_g$, accounts for the thermally activated motion of dislocations through the following expression,

$$\dot{\tilde{\epsilon}}^p_g = \dot{\tilde{\epsilon}}_0 \exp\left\{-\frac{G_0}{\mathcal{K}\theta}\left[1 - \left\langle\frac{\tilde{\sigma}^e - S}{\sigma_0}\right\rangle^p\right]^q\right\} \tag{2.5}$$

where, S, is the deformation resistance that can be functionally expressed as,

$$S = \hat{S}\{\rho, f\} \tag{2.6}$$

$\mathcal{K}$, is the Boltzmann constant, and $\dot{\tilde{\epsilon}}_0$, G_0, σ_0, p and q, are material parameters. Finally, the evolutionary equations of the model internal variables can similarly be written functionally as,

$$\dot{\rho} = \dot{\hat{\rho}}\{\dot{\tilde{\epsilon}}^p_g, \theta, \rho, f\} \tag{2.7}$$

$$\dot{f} = \dot{\hat{f}}\{\dot{\tilde{\epsilon}}^p_g, \theta, f\} \tag{2.8}$$

$$\dot{\mathbf{B}} = \dot{\hat{\mathbf{B}}}\{\mathbf{D}^p, \theta, \rho, f\} \tag{2.9}$$

The constitutive model was fully calibrated for the 293-873 K temperature range only for one

of the five steel grades studied in this work, namely the IA grade steel (see details in chapter 3). Due to the fact that the uniaxial stress-strain behaviour of the five steels at room temperature was found to be similar (*e.g.* see Figure 2.3), the constitutive model calibrated for the IA steel was also used to describe the behaviour of all the other four steels at room temperature. Note that a comparison of the measured and predicted temperature-dependent stress relaxation behaviour of the IA grade steel is given in chapter 3, and that of the IB and IC steels in Appendix E.

All the measured CT specimen force/displacement responses are presented in Figure 2.4. Here, the compressive force and the CT relative mouth opening displacement are given in absolute values. The resulting strain and stress fields upon unloading at the notch root region of CT specimens along the X-direction are shown in Figure 2.5. The 10 and 20 mm-thick specimens with a 1 mm notch radius have similar σ_{YY} residual stress distributions up to about 800 μm from the notch root. The predicted σ_{YY} residual stresses in all CT geometries show a maximum ahead of the notch root at about 300 μm from its surface. For the 20 mm-thick specimens, it was found that the smaller the notch radius, the higher the residual stresses and the smaller the tensile region along the X-direction. Thus, for the 0.5, 1 and 2 mm notch radii, the maximum residual stresses at RT were found to be 1100, 940 and 780 MPa, respectively.

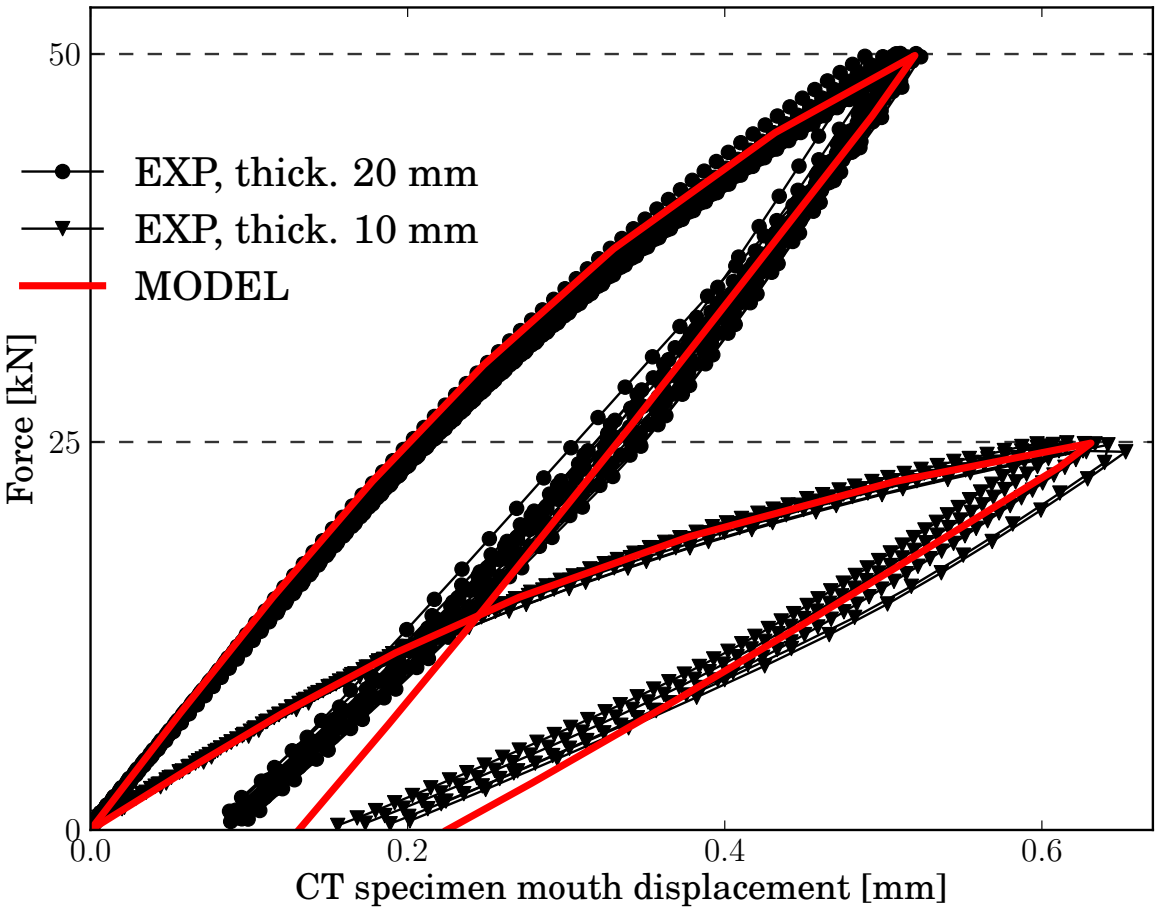

Figure 2.4: Measured and predicted force/displacement responses of the CT specimens during loading at RT.

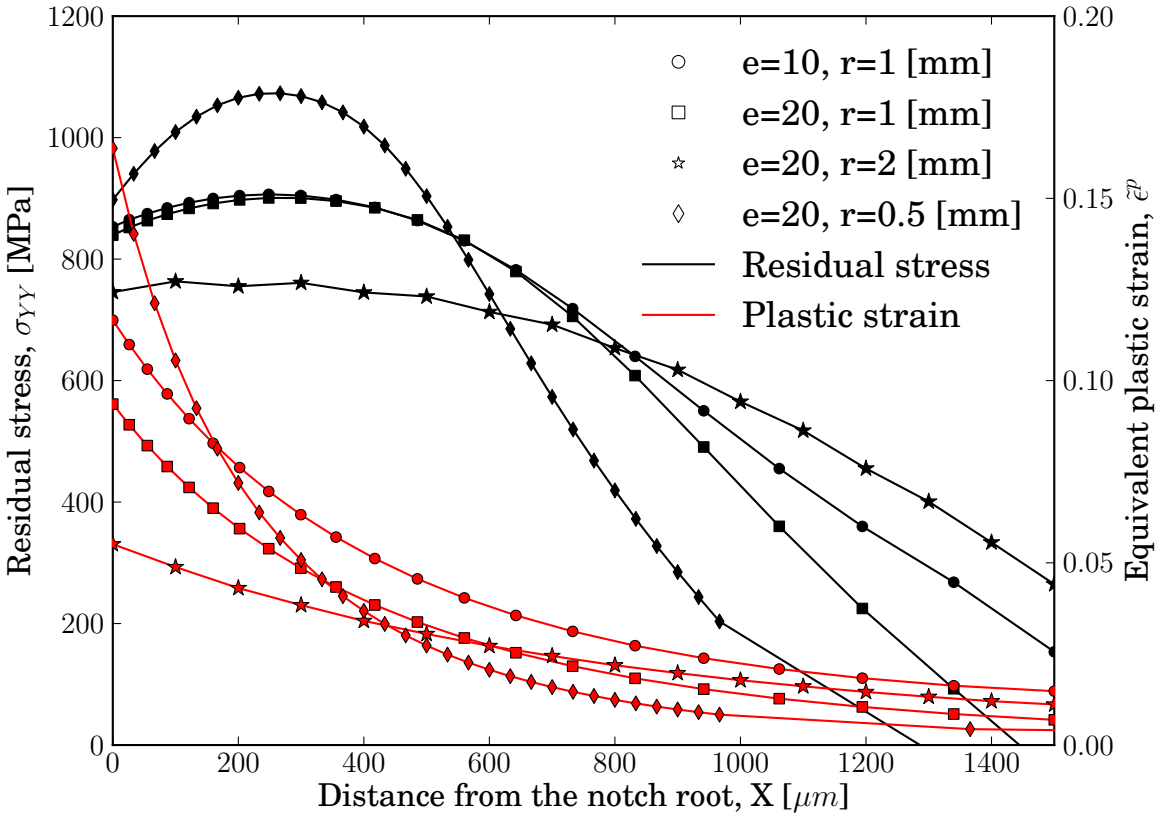

Figure 2.5: Predicted residual stresses, σ_{YY}, and equivalent accumulated plastic strain, $\bar{\epsilon}^p$, at the notch root and mid-thickness in the four different CT specimen geometries upon unloading at RT.

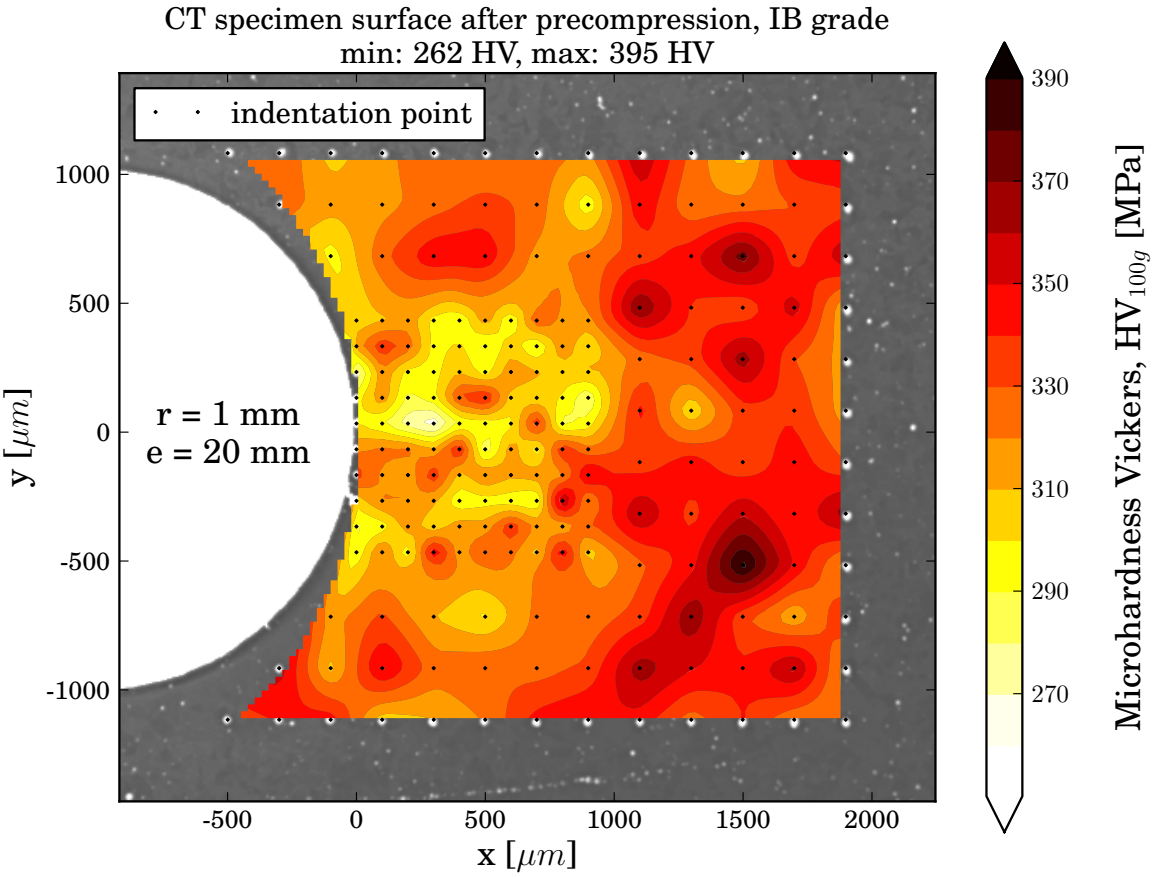

Figure 2.6: Microhardness map in the notch root region of IB grade CT specimen after compression (25 kN).

2.3.3 Quantitative indication of the existance of residual stresses

After the compression of the IB grade CT specimen (e=20 mm, r=1 mm) at RT, microhardness measurements were performed in its notch root region. Figure 2.6 shows the 100 g Vicker's microhardness map obtained by extrapolating the experimentally measured values using the natural neighbour method. The tensile residual stress field presence at the CT specimen surface is revealed by a decrease in microhardness values in the notch root region. This result may seem surprising since this zone experienced a higher plastic deformation than the base material and thus should have strain hardened more. However, it was shown experimentally (Simes et al., 1984; Tsui et al., 1996) and numerically (Bolshakov et al., 1996; Huber and Heerens, 2008) that tensile residual stresses can decrease the apparent material hardness.

2.3.4 Stress relaxation kinetics

Stress relaxation tests were performed on IB, IC and IA grade axisymmetric specimens at 823 and 873 K. These specimens had a round section of 3 mm diameter and were machined from the cold-rolled plates along the RD. The tests were conducted as follows. When the temperature attained a stable level (±0.5 K), the specimens were loaded at a strain rate of 10^{-3} s^{-1} up to 5% true strain, which corresponds approximately to the value predicted by FE in the notch root region of the CT specimens (see Figure 2.5). Then, the strain was kept constant for at least 350 hrs. The experimental results are shown in Figure 2.7(a). The measured stress relaxation results were used to identify the true viscoplastic strain rate of the IB, IC and IA steel grades at 823 and 873 K, as a function of the true stress (see Figure 2.7(b) and (c)). In these figures, the experimental data were linearly fitted in order to identify the slopes of the $\log\sigma$ *vs* $\log\dot{\epsilon}^p$ curves, and hence, the inverse strain rate sensitivity of the different steels. It should be noted that the prediction of the CT specimen force-displacement responses and residual stresses in the notch root regions relied on the FE calculations carried out with the internal variable-based constitutive model previously outlined and reported in chapter 3. For all grades, the Young's modulus used to calculate the viscoplastic strain rates was 153 GPa at 873 K and 157 GPa at 823 K chapter 3. In Figure 2.7(b) and (c), the IA and IB grades stress relaxation rates exhibit a change in the slope of the $\log\sigma$ *vs* $\log\dot{\epsilon}^p$ curves at approximately $\sim 10^{-8}$ s^{-1} while that of the IC grade remains constant. At low stresses, the slopes seem to be unaffected by temperature in all cases. The results of those tests show that the stresses relax faster in the IA than in IB and IC grades, which is consistent with their higher nitrogen contents (Mathew et al., 1991). Stress relaxation tests were not performed on the HP and LP grades, but their high temperature behaviour is expected to be similar to those of the IC and IB grades due to their close nitrogen and carbon contents.

2.4 Intergranular damage

2.4.1 Mid-thickness damage analyses

This section presents the intergranular damage analyses performed on the mid-thickness surfaces of the tested CT specimens. The optical micrograph presented in Figure 2.8(a) (see also Figure B.1 and Figure B.2) shows a typical mid-thickness surface of a damaged CT specimen (IB grade specimen with e=20 mm and r=1 mm, tested at 848 K for 3621 hrs). Damaged GBs, approximately oriented normally to the loading direction (Y) can be observed. Close-up

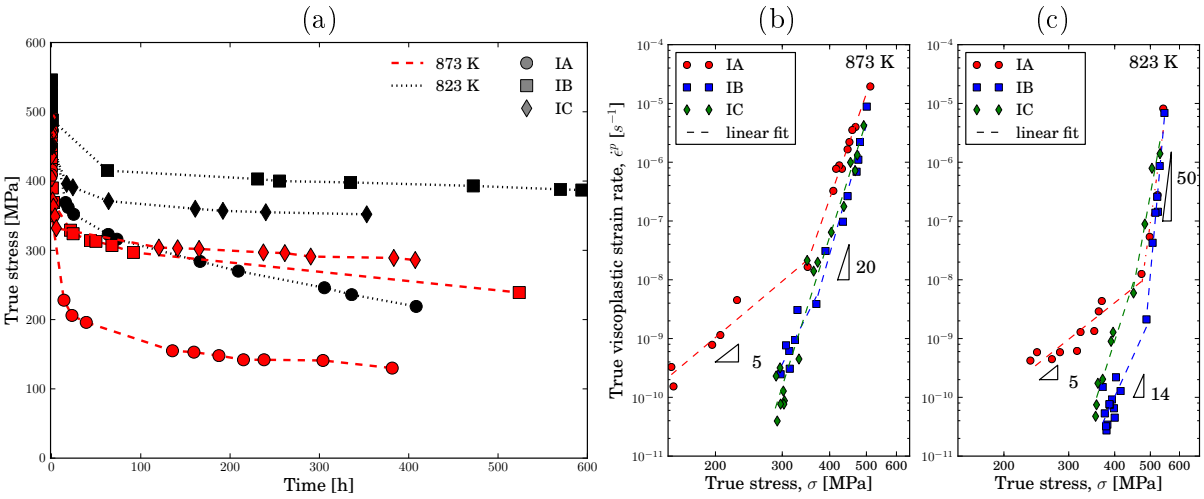

Figure 2.7: Experimental stress relaxation behaviour of the IB, IA and IC grade steels at 823 and 873 K: (a) true stress *vs* time, and the corresponding (b)(c) true viscoplastic strain rate *vs* true stress at, respectively, 873 and 823 K.

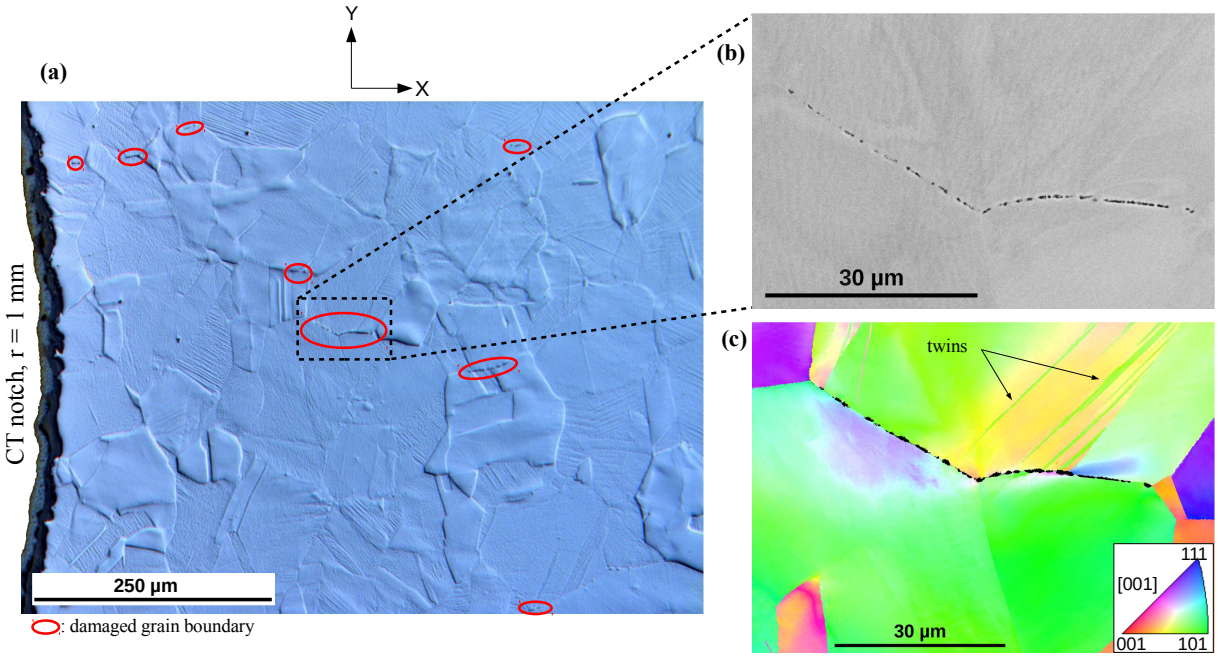

Figure 2.8: (a) Mid-thickness optical micrograph of the IB grade CT specimen tested at 848 K for 3621 hrs (e=20 mm, r=1 mm), (b) intergranular microcavities observed by SEM and (c) IPF EBSD map of the microcavities shown in (b) (IPF colour-coded figure is shown in the inset).

SEM observations of microcracks show that they result from the coalescence of microcavities (see Figure 2.8(b)). The intergranular nature of damage was confirmed by EBSD analyses (see Figure 2.8(c)). For the same testing conditions, higher amount of RC damage was observed in the 0.5 mm-notched IB specimen (see Figure 2.9). Here, the higher initial residual stresses led to the development of a macroscopic intergranular crack oriented along the X-direction (∼750 μm long). At both sides of this intergranular macrocrack, disconnected intergranular microcavities and microcracks were observed. Those observations highlight the discontinuous nature of RC damage which begins by the nucleation of intergranular microcavities, which then coalesce into microcracks and can potentially merge to form a macrocrack. The fracture surface of this specimen is shown in Figure B.4 and Figure B.5.

Table 2.2 summarises the CT specimen testing conditions. Each specimen is represented by its steel grade name with information about its thickness and notch radius. In this work, we consider that a CT specimen is damaged if a microcavity is observed optically on the mid-thickness surface of the CT specimen. All the specimens indicated in boldface red were found to have developed intergranular damage.

Amongst the forty-five tested CT specimens, intergranular microcavities or microcracks were observed in only sixteen of them. Intergranular damage was mostly identified in IB grade specimens and, to a lesser extent, in IA grade ones. The IC, HP and LP grade specimens did not develop any intergranular damage after five month exposure at either 823, 848 or 873 K. Since no damaged was observed in the HP and LP grade specimens, it was concluded that the level of P has no effect under tested conditions. In order to test the HP and LP grades under more detrimental conditions, two coupons cut from the HP and LP cold-rolled plates were pre-aged at 823 K for 1225 hrs before machining two new CT specimens of each. After the residual stress introduction, they were exposed at 823 and 873 K for 1455 hrs (see Table 2.2). In those specimens, initial GB strength was expected to be lower at the beginning of thermal exposure and thus a greater amount of intergranular damage was expected to develop subsequently. This pre-ageing actually enabled the development of RC microcavities in the HP grade specimens, while LP grade specimens remained undamaged.

Finally, a ranking of RC grade resistances can then be made from the microstructural observations (from the least to the most resistant grade): IB, IA, HP and indistinctly, IC and LP.

2.4.2 Grain boundary analyses

Figure 2.10 shows the microcavities observed by EBSD (superposition of IPF and IQ maps with a step size of 100 nm) at 150-700 μm from the notch root in the HP grade specimen pre-aged and tested at 823 K. The microcavity sizes are about 1±0.5 μm and no correlation between the intersections of GBs and deformation twins with their nucleation sites is observed. Here, the deformation twins, which were not reported in RC-affected zones of industrial welded parts (Auzoux, 2004), do not seem to alter the microcavity nucleation mechanism.

SEM observations of IB and IA grade specimens revealed that microcavities and microcracks contained intergranular particles (<200 nm in diameter) on their inner surfaces after testing at either 823, 848 or 873 K. From TEM observations, such particles were identified as $M_{23}C_6$ carbides, where, M, stands for a combination of Cr, Fe, Mo and Ni atoms (composition $(Cr_{16}Fe_4Mo_2Ni)C_6$ as determined by EDS). The crystallographic structure was identified as FCC with a lattice parameter of 10.7 $\mathring{A}$. TEM observations through a thin section taken from within

Table 2.2: CT specimen thermal exposure conditions and corresponding intergranular damage observed.

Temperature [K] \ Time [h]	∼580	∼1470	2946	3621	4313
873	**IB_1^{20}** LP_1^{20} HP_1^{20} IA_1^{10} IC_1^{10}	**IB_1^{20}** LP_1^{20} $^{PA}LP_1^{20}$ HP_1^{20} **$^{PA}HP_1^{20}$**		**IB_1^{20}** LP_1^{20} HP_1^{20}	
848	**IB_1^{20}** LP_1^{20} HP_1^{20}	**IB_1^{20} IB_1^{10}** LP_1^{20} HP_1^{20} **IA_1^{10}** IC_1^{10}		**IB_1^{20} IB_2^{20} $IB_{0.5}^{20}$** LP_1^{20} HP_1^{20}	
823	IB_1^{20} LP_1^{20} HP_1^{20}	IB_1^{20} LP_1^{20} $^{PA}LP_1^{20}$ HP_1^{20} **$^{PA}HP_1^{20}$** IA_1^{10} IC_1^{10}	**IA_1^{10}** IC_1^{10}	**IB_1^{20} IB_1^{10}** LP_1^{20} HP_1^{20}	**IA_1^{10}** IC_1^{10}

· Specimen notation: $^{pre-aged \rightarrow PA}_{steel\,grade \nearrow}\mathrm{IB}^{20 \leftarrow e\,[mm]}_{1 \leftarrow r\,[mm]}$

· Bold and red: damaged specimens
· PA: pre-aged spec. at 823 K for 1225 hrs
· Compression loadings: 25 kN for e=10 mm
50 kN for e=20 mm

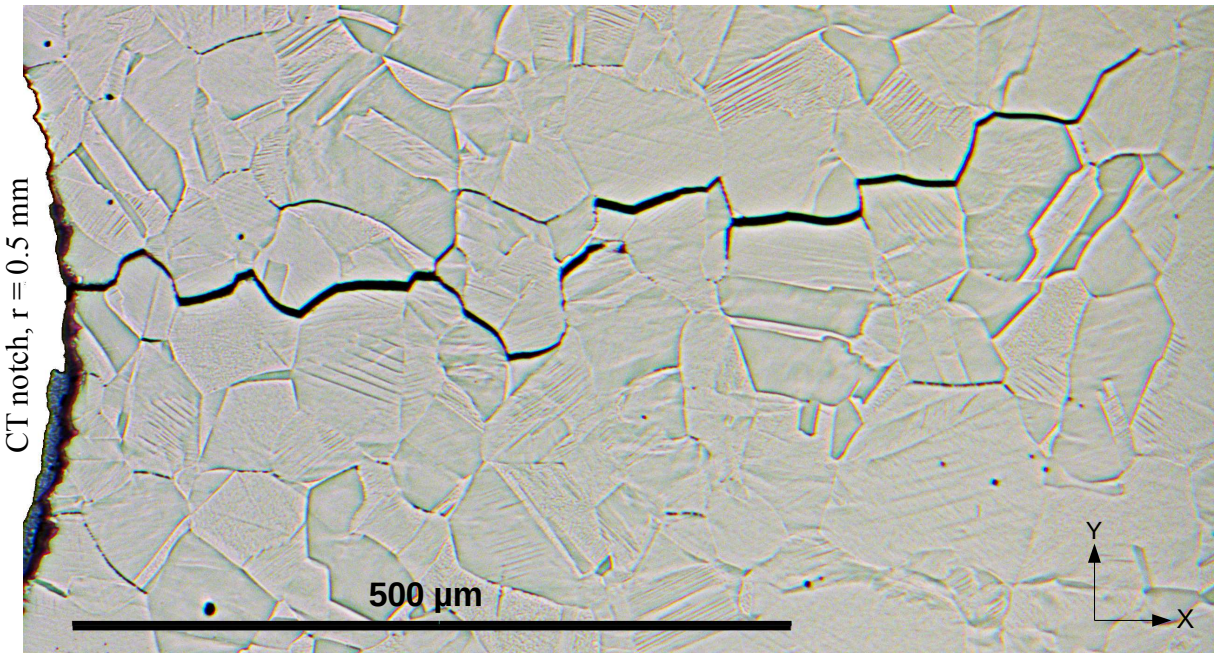

Figure 2.9: Mid-thickness optical micrograph of the IB grade CT specimen tested 3621 hrs at 848 K (e=20 mm, r=0.5 mm) showing a macroscopic intergranular crack.

the maximum residual stress zone (from IB grade, e=20 mm, r=1 mm CT specimen, tested at 848 K for 3621 hrs) revealed that $M_{23}C_6$ carbides serve as nucleation sites for nanocavities (see Figure 2.11). In this figure, the observed nanocavity mean diameter is approximately 50 nm. Other images of nanocavities can be found in appendix B, Figure B.6.

Since poor gray scale chemical contrast exists between $M_{23}C_6$ carbides and the matrix, their observation by SEM is difficult on polished surfaces. However, the opening of microcracks by plastic deformation in the *in situ* SEM tests enabled the $M_{23}C_6$ carbides to be observed since they protruded out of the microcrack inner surfaces. An example of a microcrack opened during the *in situ* SEM test is given in Figure 2.12. This micrograph shows that RC damage results from a decohesion between coarse $M_{23}C_6$ carbides and their adjacent grains (see also Figure B.3). From the experimental observations, it was concluded that the damage observed in the *in situ* SEM studies could only have evolved from grain boundary crack-like defects identified after the stress relaxation tests, *e.g.* see Figure 2.8(a). This is supported by the fact that, after the *in situ* tomography test, no damage was seen outside the regions exposed to high levels of tensile residual stresses. In addition, all RC damage was found to consist of the same rather flat intergranular crack-like defects, and no evidence of ductile damage was found at coarse particle sites (*e.g.* MnS inclusions), which would have resulted in more spherical shaped cavities.

The GB misorientation distributions of the five AISI 316L-type austenitic stainless steels were measured and compared with the misorientation distributions of 35 damaged GBs. The results are given in Figure 2.13. The GB misorientation distributions of the five steel grades are similar and ~50% are recrystalisation twin boundaries ($\Sigma 3$ twin, 60°/<111> in FCC material). The damaged GB misorientations reveal that the misorientations between 25 and 55° are detrimental to GB strength whereas no $\Sigma 3$ GB was found to be damaged, even though they represent about 50% of the total.

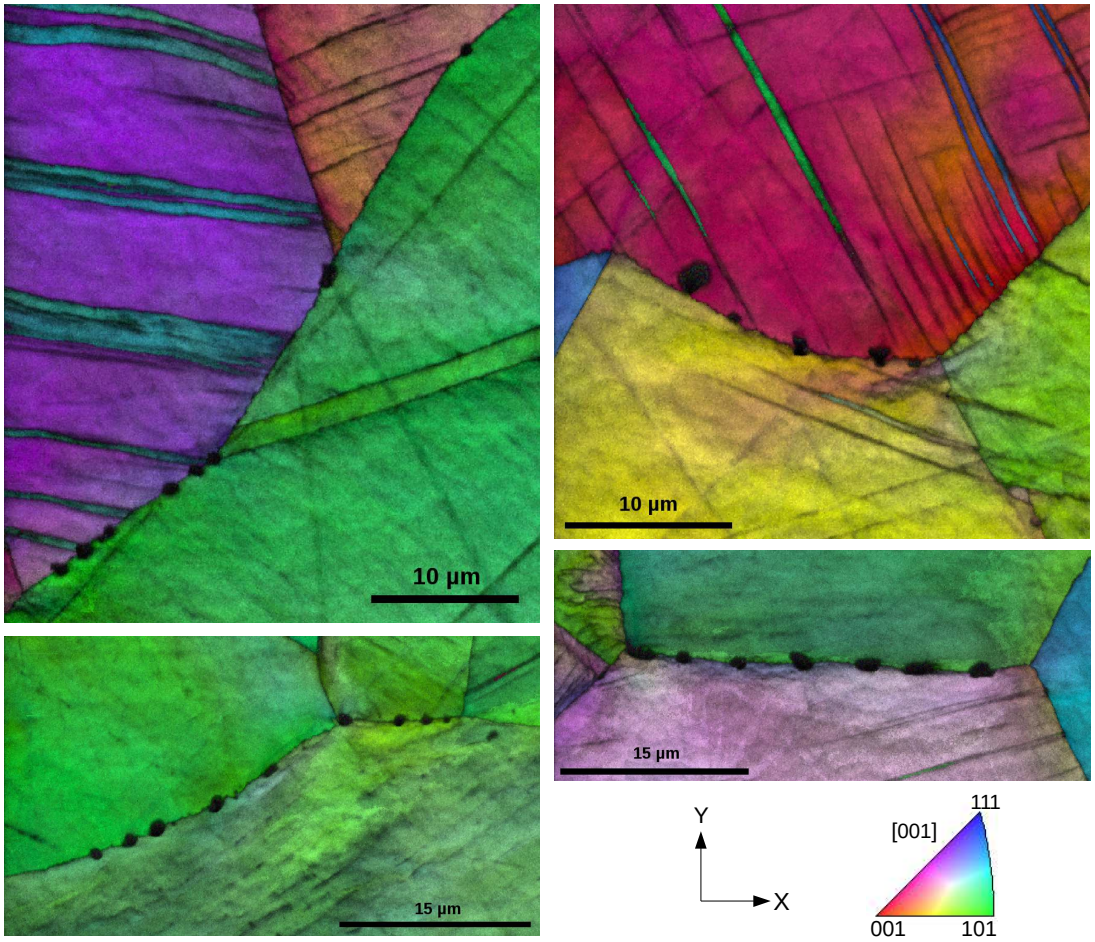

Figure 2.10: Superposition of EBSD IPF and IQ maps of regions exhibiting microcavities in the HP grade specimen (e=20 mm, r=1 mm) pre-aged at 823 K for 1225 hrs and tested at 823 K for 1455 hrs.

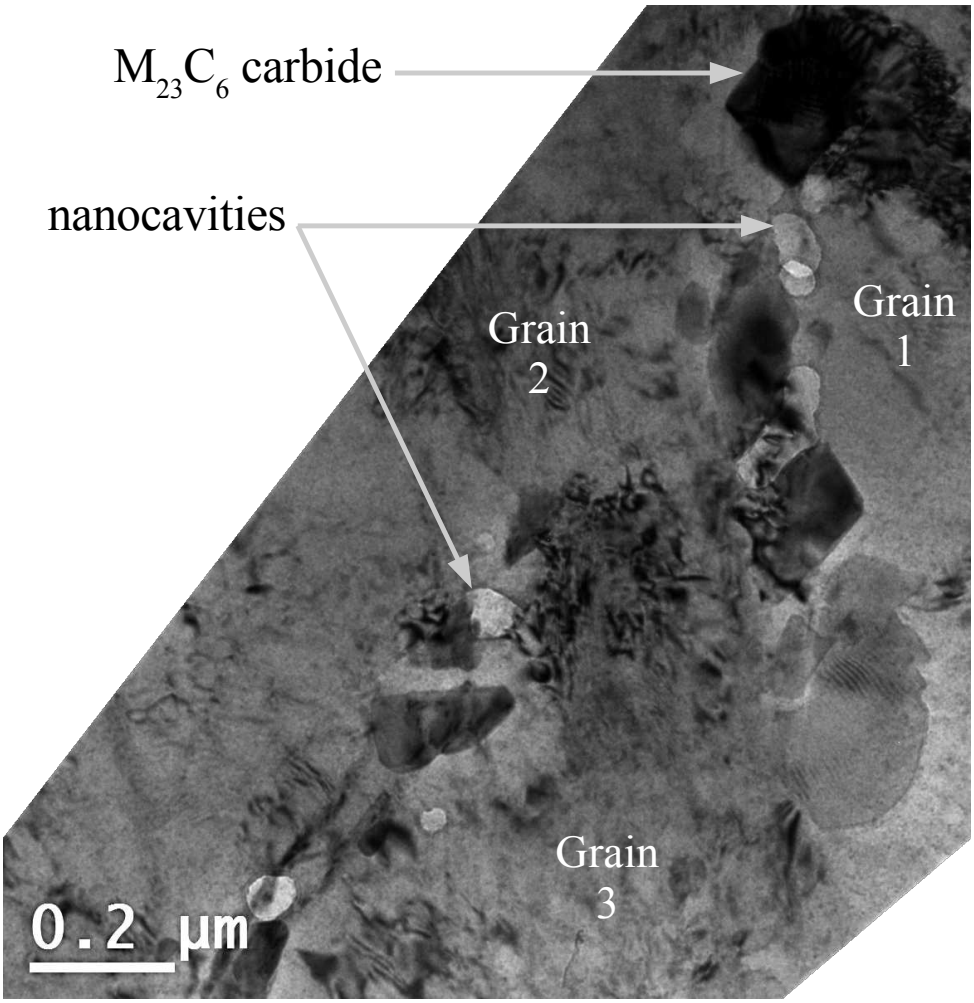

Figure 2.11: Intergranular $M_{23}C_6$ carbides and nanocavities observed by TEM.

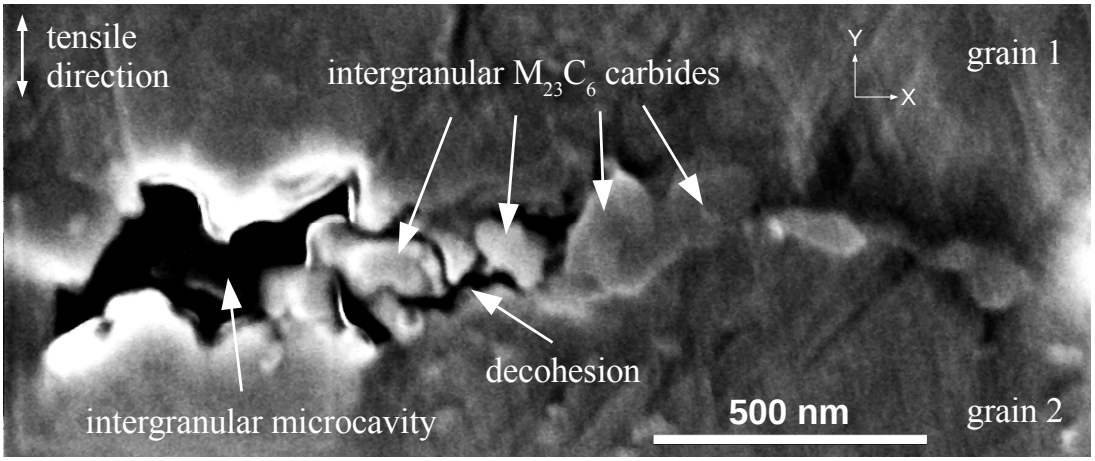

Figure 2.12: SEM image showing the partial decohesion between intergranular $M_{23}C_6$ carbides and their adjacent grains on the surface of a tensile specimen deformed *in situ* up to 11% true plastic strain (IA grade specimen, e=20 mm, r=1 mm, tested at 823 K for 4313 hrs).

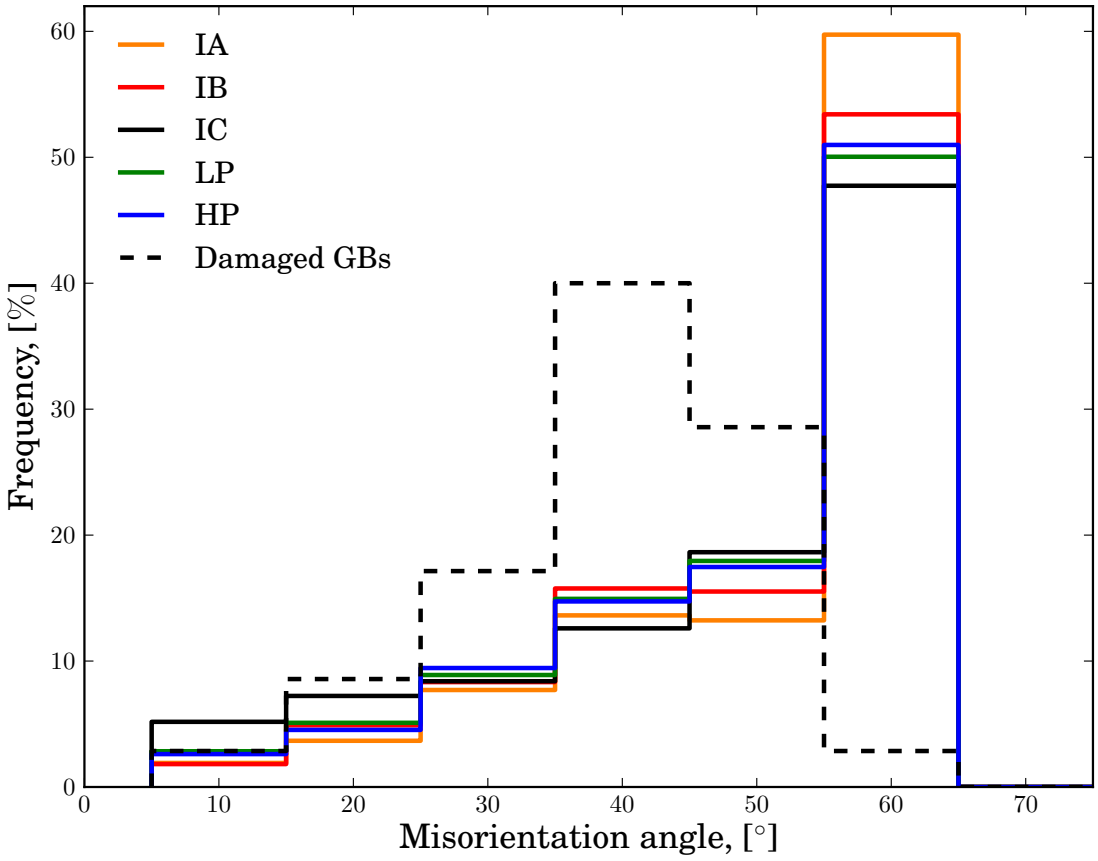

Figure 2.13: Comparison between the global distributions of GB misorientations measured by EBSD in the five austenitic stainless steels (~ 61 mm of GB measured on 1 mm^2 for each grade) and those of 35 damaged GBs identified in the IB, IA and HP steels.

2.4.3 Damage observations by synchrotron tomography

This section presents the results of intergranular damage visualisation by X-ray synchrotron tomography in tensile specimen machined from the tested CT specimens and subsequently deformed *in situ*. Figure 2.14 shows a 1450x1750x100 μm^3 slice of the notch root region of the IB grade CT specimen tested at 823 K for 2946 hrs and deformed *in situ* by up to 19% true strain. This technique enables the observation of microcracks in 3D using grayscale contrast. Note that damage appears darker than the bulk material.

A grayscale threshold level was used to create binary volumes where the matrix material is transparent and the damage is coloured. Figure 2.15 shows the damage projection along the Z-direction, in the notch root region of the IB grade CT specimen (e=20 mm, r=1 mm) tested at 848 K for 3621 hrs and *in situ* deformed by up to 23% true strain along the Y-direction. Here, the thickness of the projected slice is 500 μm. The additional homogeneous distribution of small particles that also appear coloured were identified as MnS inclusions. In this image, the black-dashed curves represent the maximum principal residual stress directions before thermal exposure predicted by the FE analysis. Good agreement is observed between the microcracks normal directions and the maximum principal residual stress directions. These results show that GB sliding is unlikely to be important under RC conditions. Furthermore, the black curve shows the distribution of intergranular damage along the X-direction. In order to quantify the intergranular damage, the scanned volume was first divided into 50 μm cubes (15 along the X-direction, 24 along the Y-direction and 10 along the Z-direction). In each cube, the microcracks were projected along the Y-direction on the bottom face (XZ). The damage was defined by the ratio of the projected-microcrack surface to the cube face area (50x50 μm^2). Finally, the damage distribution along the X-direction was obtained by averaging the damage values through the thickness (Z) and then averaging them along the Y-direction. The resulting maximum damage region is in good agreement with the predicted maximum initial residual stress distribution (see Figure 2.5).

The influence of the testing temperatures and initial residual stress magnitudes in the IB grade CT specimens were studied by synchrotron tomography. The results are given in Figure 2.16, which shows a comparison between the damage projections and the predicted maximum principal residual stresses obtained by FE. Here, Figure 2.16(a), (b) and (c) correspond to 20 mm-thick CT specimens with notch radii of 1 mm and tested at 873, 848 and 823 K, respectively, for 3621 hrs. The specimen tested at the intermediate temperature of 848 K (Figure 2.16(b)) exhibits a higher degree of damage than the others. This result was also confirmed when observing by SEM the three IB grade CT specimens tested at the same temperatures for 1455 hrs. Here the most detrimental temperature for RC resistance seems to be around 848 K for the IB grade steel. The Figure 2.16(e) and (f) maps correspond to 20 mm-thick CT specimens tested at 848 K for 3621 hrs, with notch root radii of 2 and 0.5 mm, respectively. The higher value of the principal residual stress in the 0.5 mm-notched specimen resulted in a higher amount of intergranular damage (same specimen as in Figure 2.9), whereas the 2 mm-notched specimen exhibits less damage than the 0.5 and 1 mm-notched specimens (Figure 2.16(f) and (b), respectively). In all maps, the initial threshold level of maximum principal residual stress that led to RC damage development was estimated from the different threshold values identified by the black-dashed lines in Figure 2.16at 740 ± 30 MPa.

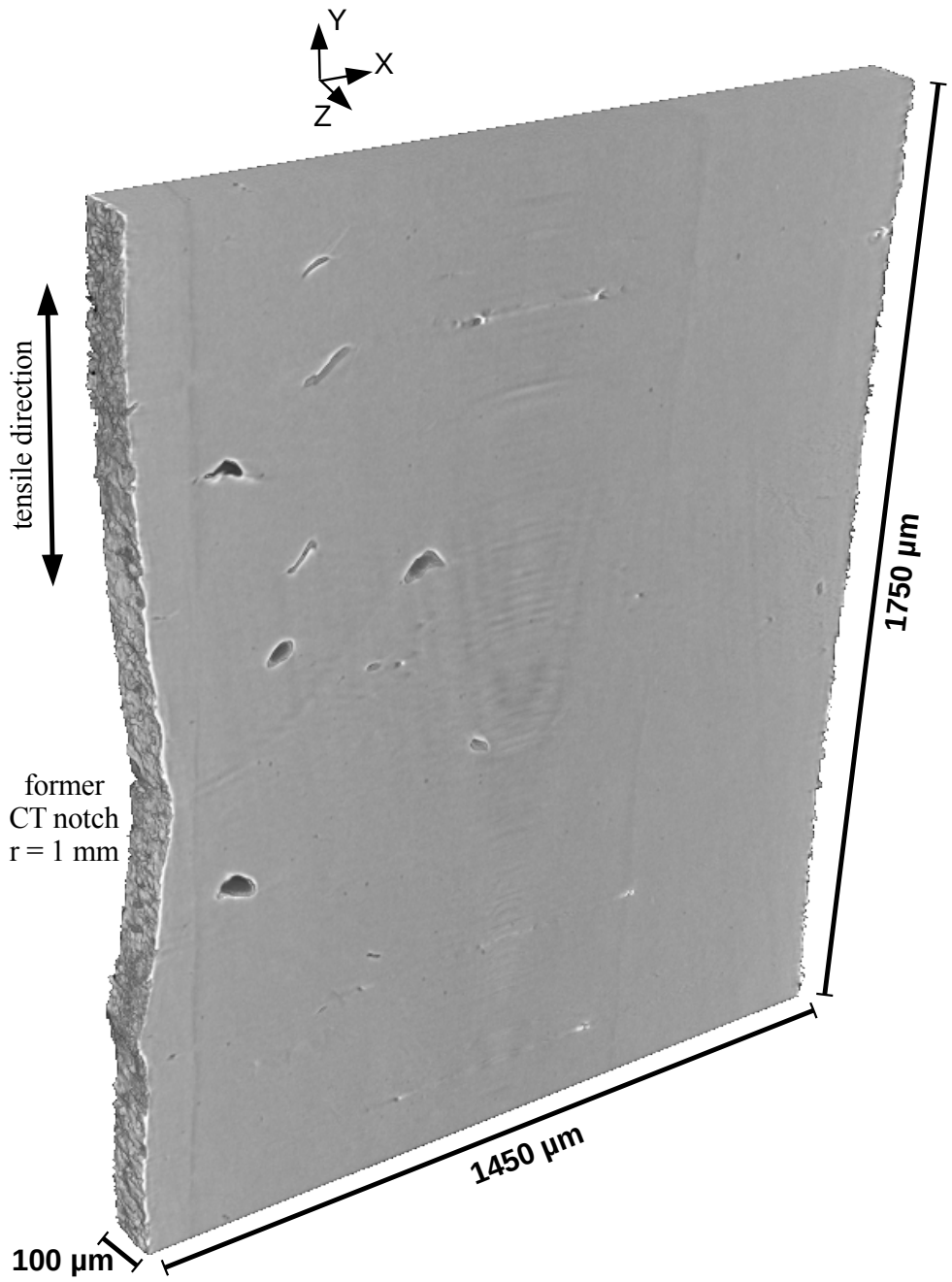

Figure 2.14: 3D synchrotron tomography data rendering in the notch root region of the former IB grade CT specimen (e=20 mm, r=1 mm) tested at 823 K for 2946 hrs and subsequently deformed *in situ* up to 19% true plastic strain.

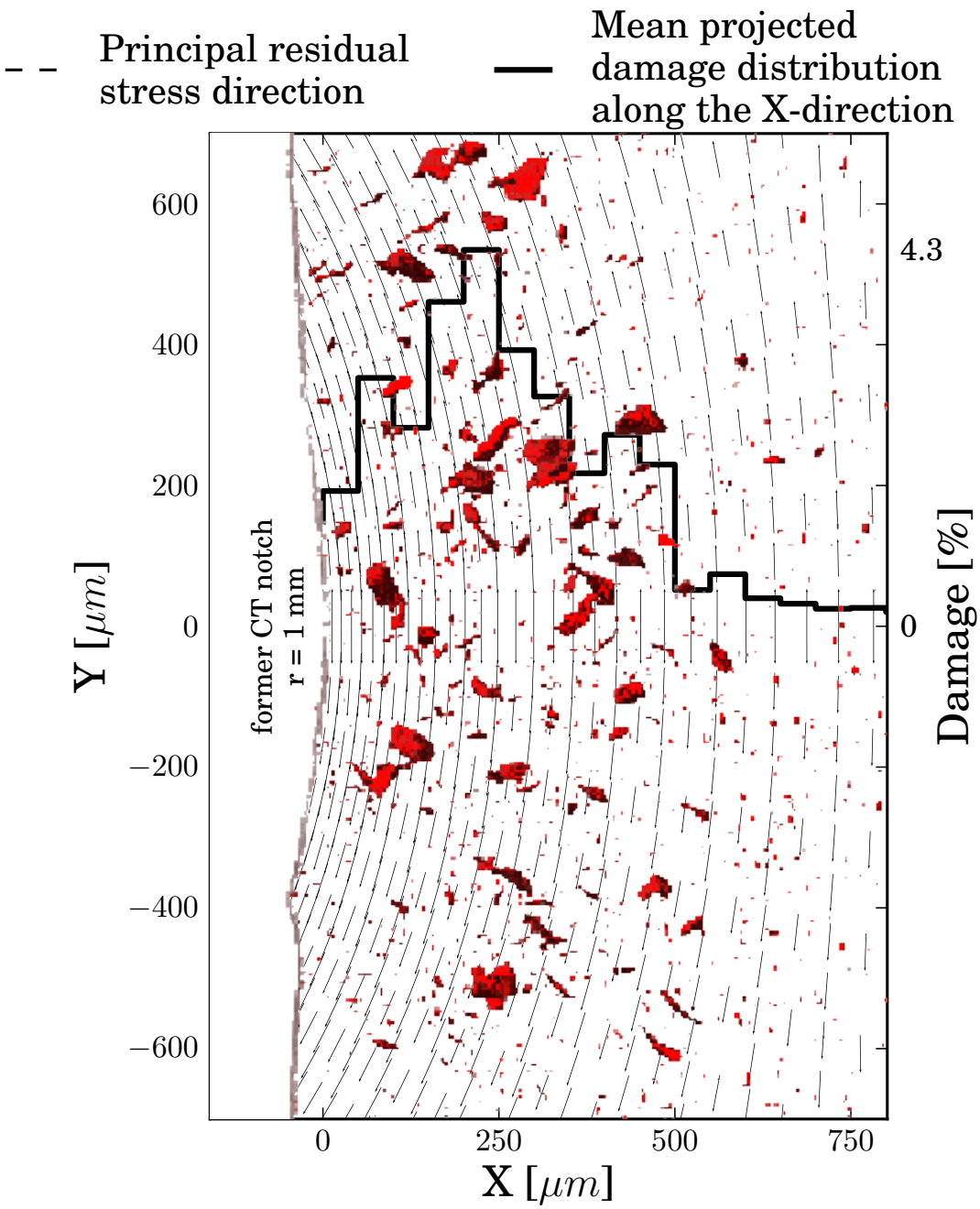

Figure 2.15: Comparison between the projection of intergranular damage identified by synchrotron tomography (500 μm-thick scan) and the initial maximum principal residual stress directions (at RT) in the notch root region of the IB grade CT specimen (e=20 mm, r=1 mm) tested at 848 K for 3621 hrs.

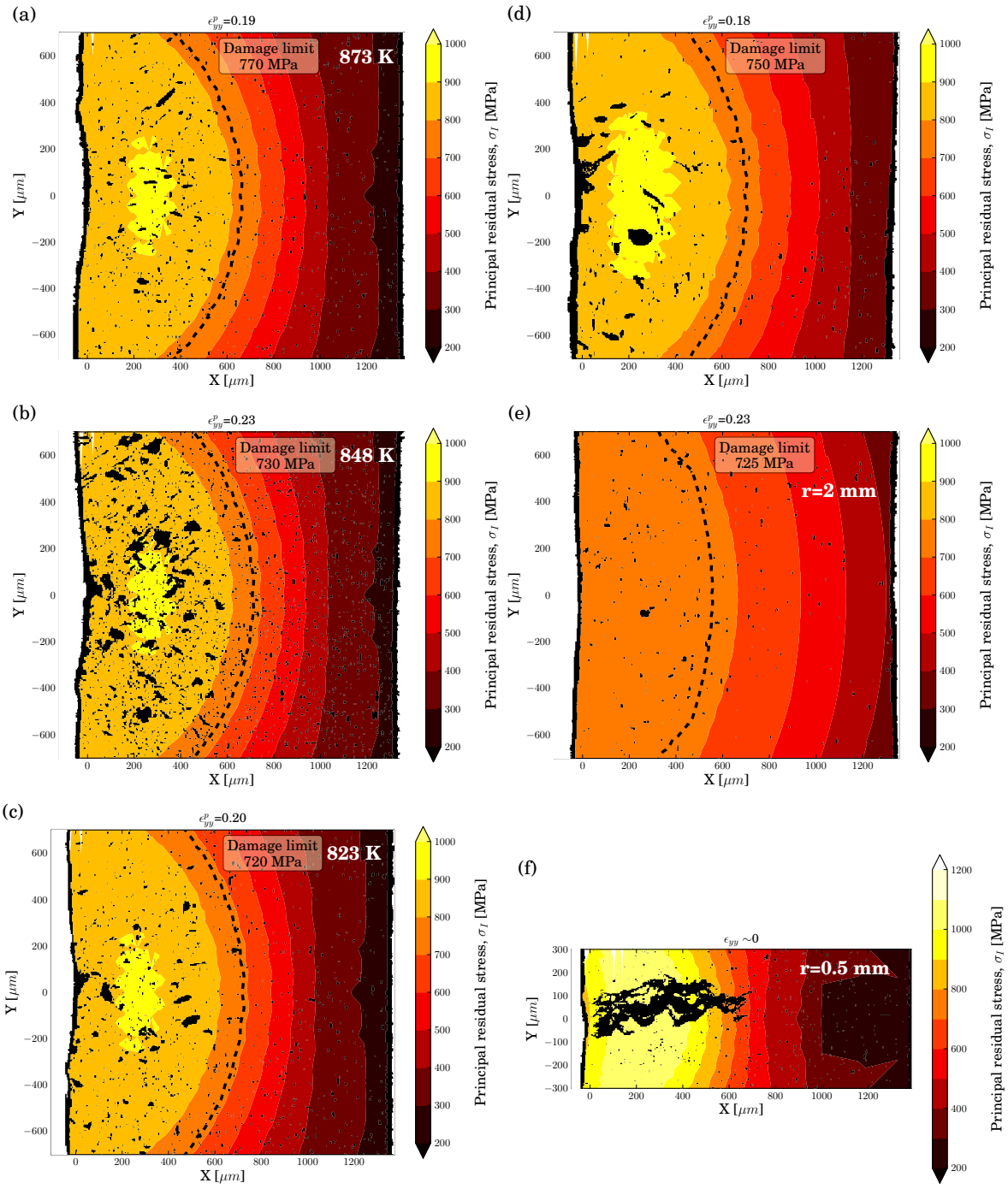

Figure 2.16: Comparison between the projection of intergranular damage obtained by synchrotron tomography (500 μm-thick scans) and the initial maximum principal residual stresses in the notch root region of IB grade CT specimens with (a)(b)(c) e=20 and r=1 mm, tested at 873, 848 and 823 K, respectively, for 3621 hrs and with (d) e=10 and r=1 mm, tested at 848 K for 1455 hrs and with (e)(f) e=20 mm and notch radii of 2 and 0.5 mm, respectively, tested at 848 K for 3621 hrs.

2.5 Discussion

2.5.1 Effect of cold rolling

The initiation of RC damage is known to occur in high residual stress regions at or near GBs which have been plastically deformed (*e.g.* (Auzoux, 2004)). However, to achieve the initial residual stress level needed to develop RC (about four times the material yield strength at room temperature for the less RC-resistant grade steels tested in this work), it is generally required that the material be strain hardened prior to service. Evidence to that effect is the high hardness levels measured in actual RC affected regions (Auzoux, 2004; Bouchard et al., 2004) and the TEM observations of increased dislocation densities in the HAZ of an AISI 316L(N) weld reported by (Auzoux, 2004). It should also be noted that all the materials in this study were pre-conditioned by cold rolling whereas RC affected regions in the HAZ of actual components undergo thermal loadings (*e.g.* during multipass welding) that may involve several cycles leading to plastic deformations at moderate-to-high temperatures. SEM observations of the cold-rolled material were carried out and revealed that no GB damage (*i.e.* microcavities) was present using the peak resolution of the SEM. In addition, no damage was observed after the residual stress relaxation tests in the IC and LP steels that posses similar mechanical properties as the other tested steels where RC damage was found. Thus, it can be concluded that GB damage could not have been introduced either as a result of the plastic deformation of the CT specimen during the room temperature compression test. Even though SEM-EBSD observations revealed that the material cold rolling introduced mechanical twins in the microstructure, their presence was not found to have affected the main intergranular damage mechanisms responsible for RC in the austenitic stainless steels (*e.g.* GB microcavity nucleation at intergranular carbides). These observations support the understanding that the use of cold rolled materials is suitable to study RC, at least from a mechanical point of view since the chemical characteristics of actual HAZ GBs may be affected by the thermal cycling of the HAZ regions during welding. Concerning the latter, it is also worth noting that a typical welding cycle in a 316L(N) steel has been reported to last typically only a couple of seconds and the peak HAZ region temperature to be approximately 923 K (Auzoux, 2004).

2.5.2 Chemical composition and temperature effects

The results of the RC experiment performed on the CT-like specimens showed evidence of GB degradation by intergranular carbide precipitation and, to a lesser extent, P segregation, when tested in the 823-873 K temperature range. Furthermore, the stress relaxation rates were found to decrease with high N contents, thus the lowest relaxation rates being in the high N grade steels (IB and IC). Reheat cracking damage development is next discussed based on the results summarised in Figure 2.17. Here, the data from Table 2.2 are presented so as to compare the respective effect of C, N and P contents on RC damage development. Figure 2.17(a), (b) and (c) shows the results of damage observation in specimens whose chemical composition differ only in the C, N and P contents, respectively. In each subfigure, the CT specimen geometry is identical. In Figure 2.17(d), the effect of temperature on RC damage development is based on the results obtained in the IB grade specimens.

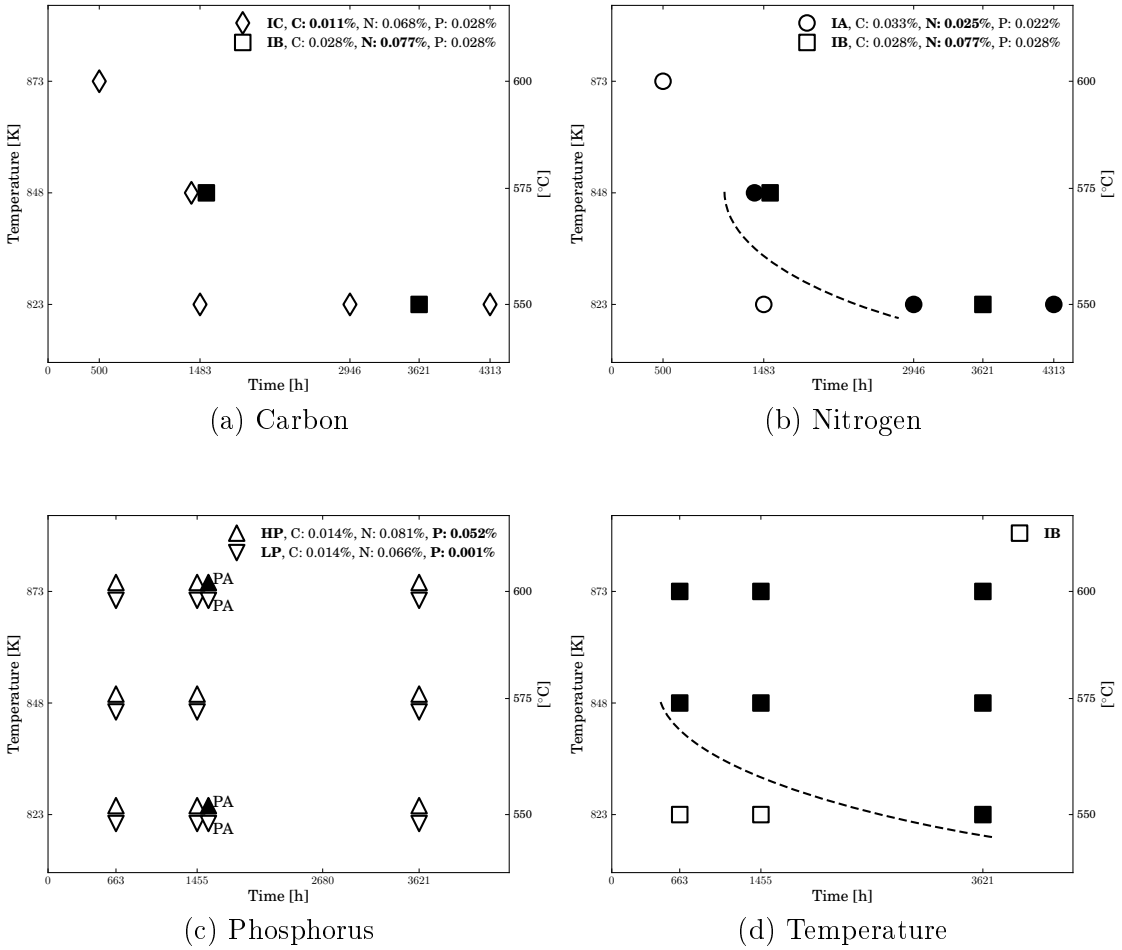

(a) Carbon (b) Nitrogen

(c) Phosphorus (d) Temperature

Figure 2.17: Effect of (a) carbon, (b) nitrogen, (c) phosphorus and (d) temperature on RC damage development. Open symbols indicate undamaged specimens and filled ones damaged. PA: pre-aged spec. at 823 K for 1225 h.

2.5.2.1 Carbon effect

Figure 2.17(a) shows the effect of C content in RC damage development (for e=10 mm and r=1 mm CT specimens). In the same conditions, the IB grade which has a high C content (0.028%) exhibits intergranular damage while the IC one (0.011% C) does not. The N and P content being similar, the lower resistance of IB grade is attributed to its higher intergranular carbide precipitation which decreases GB strength. At the microstructural scale, this observation is confirmed by the higher propensity to RC of the 25 to 55° misoriented GBs (see Figure 2.13), which are preferential surfaces for $M_{23}C_6$ carbide precipitation. Likewise, the lower propensity of $\Sigma 3$ GBs to RC is consistent with the fact that they are hardly affected by $M_{23}C_6$ carbide precipitation. The detrimental effect of high C content has also been confirmed by TEM observations since they revealed that $M_{23}C_6$ carbides are preferential sites for nanocavity nucleation (see Figure 2.11).

2.5.2.2 Phosphorus effect

Without pre-ageing, HP and LP grades did not develop intergranular damage (see Figure 2.17(c)). However, higher P content was found to increase microcavity nucleation as observed in the pre-aged HP grade steel. The P segregation levels expected at GBs in the HP grade steel was predicted using the Langmuir-McLean model (see D). The diagram shown in Figure 2.18 represents the predicted P monolayer coverage as a function of temperature and ageing time. For HP steel grade, P monolayer coverage in the tested CT specimens was expected to be about 37-41% after ~3600 hrs at 823-873 K. However, in low alloy steels, a threshold value in P monolayer coverage (~5-10%) below which no intergranular damage is observed was found (Ding et al., 2005; Naudin et al., 1999). Therefore, if we consider this threshold value as that which would trigger intergranular damage development under RC conditions, the P monolayer coverage prediction of the HP grade should be inaccurate.

The P monolayer coverage model takes no account of the individual effects of other solute elements present in AISI 316L-type steel: in austenite, some authors reported P-C repulsion interaction at GBs (Andrieu et al., 2014; Erhart and Grabke, 1981a; Paju et al., 1988; Ševc et al., 2002) or site-competing segregation mechanisms, such as P-B (Paju and Möller, 1984; Paju et al., 1988) or P-N (Briant, 1987a,b; Briant and Andresen, 1988; Erhart and Grabke, 1981b). Latter work by Briant *et al.* (Briant and Andresen, 1988) showed that phosphorus segregation can clearly be inhibited by the additions of N in 304L and 316L-type austenitic stainless steels. In order to determine the predominant segregation interaction in our 316L-type IB and HP steels, measurements of the P, N and B monolayer coverage by Auger electron spectroscopy were attempted but gave no conclusive results due to the tendency of austenitic stainless steel to undergo ductile fracture at low temperatures. An understanding of the site-competing segregation mechanisms involving P, C, N and B will be addressed in future work.

2.5.2.3 Nitrogen effect

Figure 2.17(b) shows the N content effect on RC damage development (for e=10 mm and r=1 mm CT specimens). In the same conditions, the IB grade which has a high N content (0.077%) presents more intergranular damage than the IA (0.025% N). Even though CT specimens of both grades developed damage under the same testing conditions, microstructural observation by SEM and synchrotron tomography shows that the IB grade exhibits much more intergranular

damage than the IA. The C contents being similar, the GBs should contain an equivalent number of sites ($M_{23}C_6$ carbides) for nanocavity nucleation. However, the lower stress relaxation rate (see Figure 2.7) induced by the high N content in the IB steel grade should enable high residual stresses at GBs to be maintained for a longer time and thus increase the number of nanocavities. According to the discussion results of Section 2.5.2.2, high N content could therefore have two contrasting effects on RC resistance: a detrimental one due to low stress relaxation rate and a beneficial one as it could impede intergranular P segregation by a site-competing mechanism.

2.5.2.4 Temperature effect

Figure 2.17(d) shows the effect of temperature in RC damage development (for e=20 mm and r=1 mm IB grade CT specimens). At 823 K, no intergranular damage was observed before ∼3600 hrs but after ∼660 hrs at 848 and 873 K. In addition, higher amount of damage was observed in the IB grade CT specimen tested at the intermediate temperature of 848 K than those tested at either 823 or 873 K for ∼660 to ∼3600 hrs. To explain this detrimental effect of the intermediate testing temperature on RC, it should be noted that the intergranular damage mechanisms identified here ($M_{23}C_6$ carbide precipitation, stress relaxation controlled by the amount of N in solid solution and, to a lesser extent, P segregation) are diffusion-controlled. Figure 2.19 shows a proposed schematics to explain the existence of the most detrimental temperature to minimise the time of the RC damage onset. At temperature T_i (for i=1,2 or 3), the RC damage is assumed to start at time, t_i, when the residual stress curve, $\sigma(t,T_i)$, intersects the GB strength one, $S_{GB}(t,T_i)$. The temperature-dependant kinetics of those phenomena can lead to the formation of the bell-shaped curve shown as a dashed line in Figure 2.19. Here, the intermediate testing temperature T_2 would enable an earliest development of RC damage than a higher temperature such as T_1. The existence of a most detrimental temperature could therefore be explained and should change with chemical composition (especially C and N) of the 316L-type austenitic stainless steels.

2.5.3 Susceptibility to RC of the five steel grades

The microstructural observations presented previously enable the five tested 316L-type grades to be ranked in terms of the increasing resistance to RC: IB, IA, HP and, indistinctly, LP and IC. Table 2.3 shows this grade ranking associated with their C, N and P contents. IC grade is the most resistant to RC in the tested conditions while IB grade being the least resistant. Those results are not surprising since the IC grade was also found to be highly resistant to creep-fatigue at 873 K while the IB grade did not (Argence and Pineau, 1995). In accordance with the previous discussions, Table 2.3 shows that high P content has little effect on RC. The major chemical composition effects on RC susceptibility were found to be due to the C and N contents: high C content (about >0.025%) is detrimental to GB resistance and high N content (about >0.06%) should be added only if the C content is low (about <0.015%).

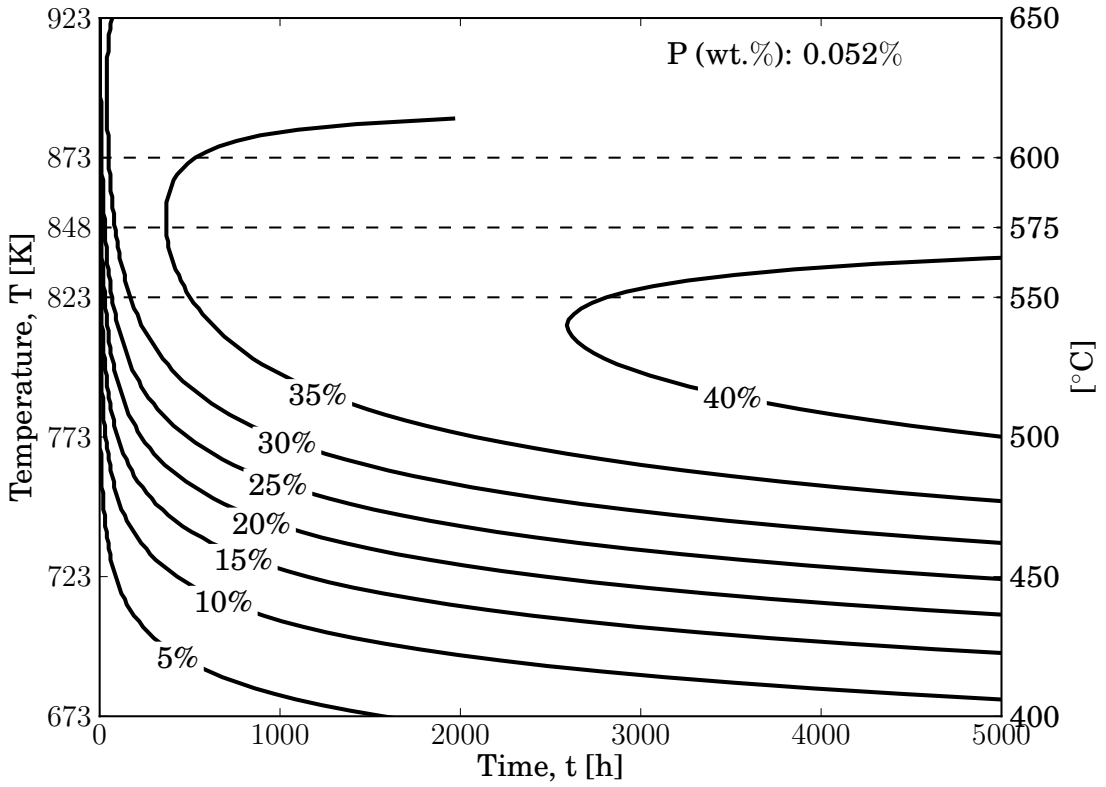

Figure 2.18: Isolines of constant P monolayer coverage in a time/temperature diagram predicted by the Langmuir-McLean model in an austenitic stainless steel with a P bulk content of 0.052%.

Table 2.3: Reheat cracking resistance ranking of the five AISI 316L-type steels and their C, N and P contents (wt.%)(1 being the most resistant).

Ranking	5^{th}	4^{th}	3^{rd}	1^{st} or 2^{nd}	1^{st} or 2^{nd}
Name	IB	IA	HP	LP	IC
C	0.028	0.033	0.014	0.014	0.011
N	0.077	0.025	0.081	0.066	0.068
P	0.028	0.022	0.052	0.001	0.021

2.5.4 Effect of stress state

Many authors have found that stress triaxiality decreases the material ductility in 316, 316H, 316L and 316L(N) steels under creep conditions (Auzoux et al., 2005; Moen and Smith, 1975; Willis et al., 1999; Wilshire and Willis, 2004). In creep damage models, extended viscoplastic cavity growth is generally associated with high triaxiality levels (*e.g.* (Spindler, 2007)). In contrast, in this work it was found that the maximum principal residual stress component is probably the main driving force for the development of intergranular damage under stress relaxation conditions. This can be seen from the information presented in Figure 2.20, which shows a comparison between the damage measured by tomography in the IB steel specimens with a notch root of 1 mm at 823, 848 and 873 K, and the predicted distributions of the initial maxi-

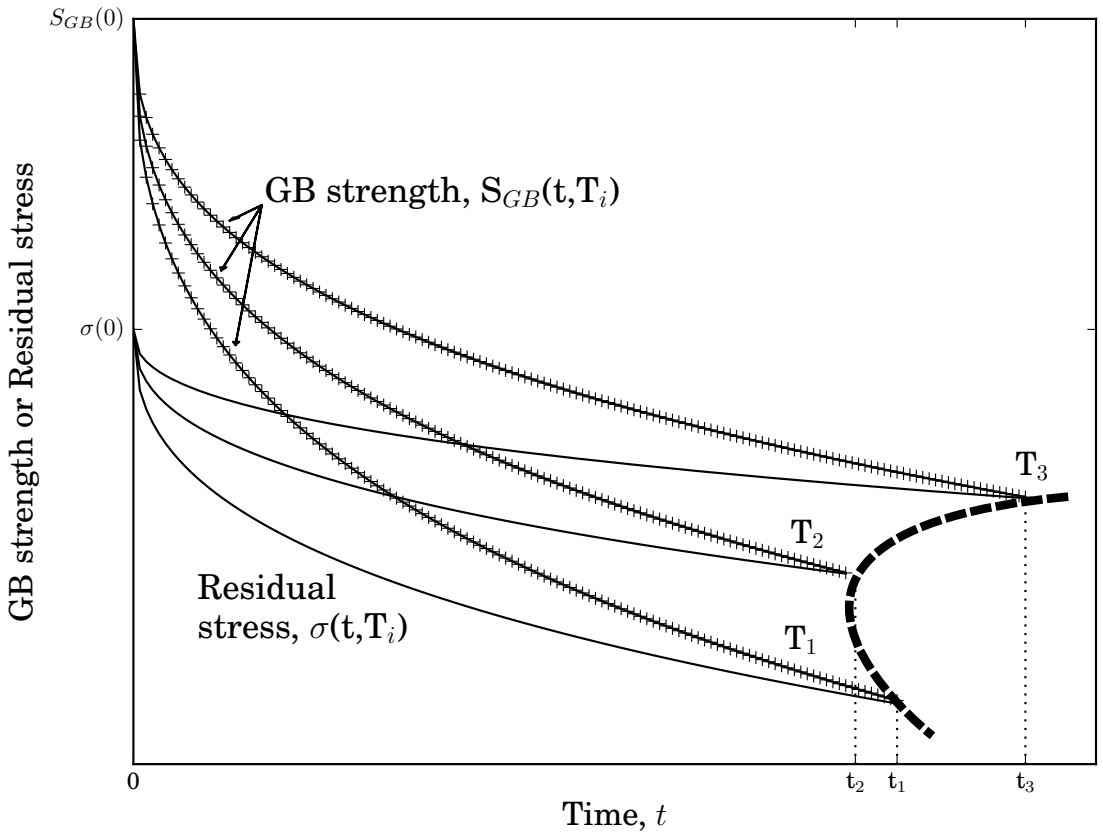

Figure 2.19: Schematic of the proposed competing mechanisms arising from residual stress relaxation and GB degradation over time. The dashed line represents the *loci* of points for the onset of RC damage at different temperatures ($T_1 > T_2 > T_3$)

mum principal residual stress, σ_I, and the stress triaxiality. Here, the latter was defined as the ratio between the mean hydrostatic stress and the equivalent Mises stress, $\sigma_H/\tilde{\sigma}$. The damage definition was that used in Figure 2.15. It can be seen that the loci of maximum measured damage for the three tested temperatures are in better accordance with the location of the peak maximum principal residual stress than that of the stress triaxiality. The effect of stress state on the damage development in the tested CT specimens are studied and discussed in more detail in a separate publication chapter 3.

2.6 Conclusions

The study of reheat cracking in five chemically different AISI 316L-type austenitic stainless steels was successfully performed using a compressed CT specimen technique. A comparison of the grade susceptibilities to intergranular damage development in the 823-873 K temperature range in the presence of high tensile residual stresses enabled an identification of the reheat cracking damage mechanisms to be made. They are: (i) the development of nanocavities on intergranular $M_{23}C_6$ carbides which precipitate preferentially on 25 to 55° misoriented GBs, (ii) the low stress relaxation rate which enables high residual normal stresses on GB to be maintained, and to a lesser extent, (iii) the P segregation at GBs which increases intergranular microcavity nucleation.

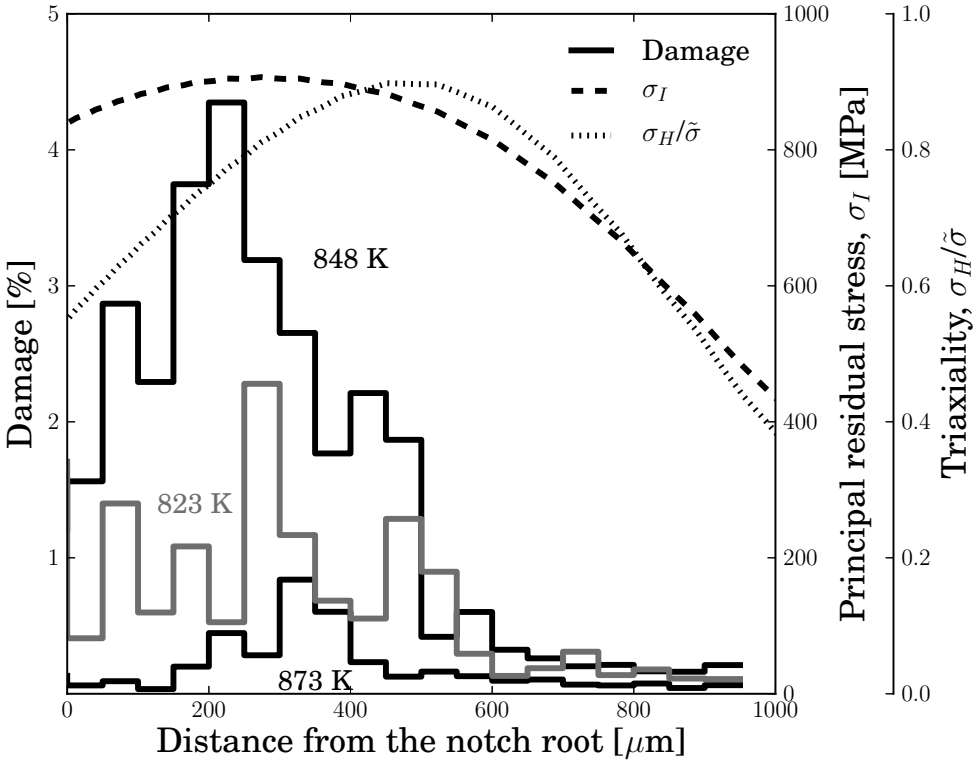

Figure 2.20: Comparison between the predicted initial principal residual stress and triaxiality distributions and the tomography-measured damage along the X-direction from the notch root of the tested IB steel CT specimens at 823, 848 and 873 K.

The use of cold rolled 316L-type steels made it possible to attain the level of residual stresses needed to develop RC in these materials without altering the above mentioned RC damage mechanisms. Furthermore, *in situ* synchrotron X-ray tomography was successfully relied upon to identify and quantify the level of intergranular damage in the specimens but only after the specimens were plastically deformed uniaxially in tension at room temperature to open up and thus render visible the intergranular microcracks.

The most detrimental operating temperature for reheat cracking damage development was found to depend on the stress relaxation behaviour and GB degradation which are directly linked to the chemical composition of the austenitic stainless steel. In particular, the intermediate testing temperature of 848 K for the AISI 316L-type IB steel was identified as the most damaging amongst the three tested temperatures under reheat cracking conditions. Furthermore, in this steel grade, a maximum principal residual stress threshold of 740 ± 30 MPa (at RT) below which no intergranular damage was found after ~3600 hrs in the 823-873 K temperature range. Furthermore, the effect of high P content was not found to be as detrimental as expected and could be explained by the site-competing segregation mechanisms between P, N, C and/or B. In the presence of high principal residual stresses ($> 740 \pm 30$ MPa), high C content (about >0.025%) was found to be detrimental to GB resistance, thus high N content (about >0.06%) should be added only if the C content of the steel is low (about <0.015%). This work has provided information about the level of residual stresses that can lead to the development of RC in AISI 316L-type steels, and of the C, N and P contents that can be relied upon as qualitative measures for future RC models/criteria to optimise welding process models and their predictions.

CHAPTER 3

Rate-dependant constitutive model formulation for 316L-type austenitic stainless steels

Résumé

Ce chapitre concerne la prédiction numérique des contraintes et déformations résiduelles dans la région du fond d'entaille des éprouvettes CT présentées au chapter 2 et utilisées pour reproduire la fissuration par relaxation. Dans ce but, un nouveau modèle de comportement viscoplastique à variables internes basées sur des longueurs liées à la microstructure du matériau, est proposé. Il a été implémenté dans le code élements finis Zébulon puis calibré. La calibration du modèle a été effectuée à partir d'essais mécaniques sur l'acier IA et de données de la bibliographie. Pour cet acier, les paramètres du modèle sont disponibles en Appendix F. Il a été trouvé que les comportements des aciers IB et IC diffèrent de celui de l'acier IA à hautes températures. Pour cette raison, certains paramètres du modèle ont été re-calibrés afin de pouvoir décrire convenablement le comportement en relaxation des aciers IB et IC. Ces paramètres sont disponibles en Appendix E. Le modèle de comportement viscoplastique est par la suite appliqué à la prédiction des contraintes résiduelles introduites à température ambiante dans la région du fond d'entaille des éprouvettes CT ainsi qu'à leur relaxation à hautes températures.

This chapter is concerned with the numerical predictions of the residual strain and stress fields present in the notch root regions of the CT specimens presented in chapter 2. To that purpose, a novel viscoplastic constitutive model is proposed, calibrated from IA steel (see Table 2.1) data mainly obtained in this work, and implemented into the finite element method (the calibrated parameters for IB and IC steels are given in Appendix E). It was then applied to the prediction of the residual stress relaxation in the notch root region of the pre-deformed CT-like specimens. This chapter is structured for a later publication.

Abstract

The presence of high tensile residual stress fields in austenitic stainless steels can lead to intergranular cracking when exposed at temperatures close to 575°C. Here, a viscoplastic constitutive model is proposed to predict both the development of residual stresses in AISI 316L-type steels by inelastic deformation at room temperature and their subsequent relaxation at high temperatures. The formulation relies on a single rate-dependent flow rule to describe the material inelastic and rate-dependent behaviour ranging from room temperature up to typical service temperatures (∼500-600°C). The evolution of the material behaviour is described through internal state variables explicitly linked to intrinsic microstructural length scales, viz. the dislocation spacing and the deformation twin spacing. Deformation twinning is assumed to occur above a critical effective stress which depends on temperature through the stacking fault energy. The constitutive model was formulated assuming large strain kinematics, calibrated from AISI 316L-type steel data mainly obtained in this work, and implemented into the finite element method. It was then applied to the prediction of the residual stress relaxation in the notch root region of pre-deformed CT-like specimens.

Contents

3.1 Introduction

Residual stresses can affect the integrity of massive welded parts used in the power generation industry. Depending on the thermo-mechanical and/or environmental conditions, significant levels

of tensile residual stresses in AISI 316L-type austenitic stainless steels are known to cause or exacerbate intergranular damage development at high temperatures. One such intergranular damage phenomenon, known as reheat cracking (RC) or stress relaxation cracking, can potentially be found in heat affected zones (HAZ) of large welded parts which are exposed to subsequent service temperatures in the ~500-700°C range. Such intergranular damage is known to be driven by the high temperature relaxation of residual stress fields initially introduced during welding due to thermal strain and deformation incompatibilities (Dhooge, 1998). Consequently, the numerical prediction of this damage phenomenon mainly relies on the ability to predict accurately the residual strain and stress field and their time evolutions near weld regions. However, numerical predictions are particularly challenging due to the complex thermo-mechanical loadings and microstructure heterogeneities associated with the welding process. Since the early 2000's, experimental methods have been devised to study RC under closely controlled laboratory conditions. Some methods rely mainly on the re-creation of representative HAZ microstructures by a combination of thermo-mechanical treatments, such as cold rolling and thermal ageing (Chabaud-Reytier et al., 2003) or hot rolling (Auzoux et al., 2010). Then, the material is tested under creep or stress relaxation conditions. Other methods consist of introducing residual stresses, in the pre-aged and/or pre-deformed material, by *e.g.* water quenching cylindrical specimens (Hossain et al., 2007) or by punching or compressing CT-like specimens (Hossain et al., 2010; Sherry et al., 2002; Turski et al., 2008). The specimens containing residual stresses are then exposed to high temperatures for several hundred hours to enable the stress relaxation to take place. The prediction of the strain and stress field evolutions in such specimens require a constitutive model capable of accurately describing the material mechanical response over large ranges of temperature and strain rate. The current most common approach consists of applying several phenomenological models to describe the successive material responses under the different temperatures and/or the different loading conditions of interest. For example, in the work by Hossain et al. (2010); Turski et al. (2008), the residual stresses present in the specimens after mechanical loading are predicted using a rate-independent elasto-plastic framework. Then, the residual stress relaxation predictions are performed using phenomenological laws for primary and secondary creep at a given temperature. Such approaches require the calibration of a new set of parameters for each potential temperature and/or prestrain level and thus does not enable the material response to be extrapolated to conditions outside those used for the calibration. The ability to extrapolate the material response are required (i) to numerically assess the thermo-mechanical conditions that can lead to the development of the residual stress levels that are known to be critical for RC, (ii) to reproduce numerically the required residual stress conditions needed to predict RC damage at untested temperatures and (iii) to reduce the number of mechanical tests needed to study the residual stress-strain evolutions when several temperatures and/or prestrain levels are considered.

A large number of phenomenological constitutive models have been proposed to describe the mechanical behavior of AISI 316L-type austenitic stainless steels (*e.g.* see review by Chaboche (2008)). However, existing models are generally too phenomenological to predict the material response with a single set of parameters over a large range of temperature and loading conditions. This work addresses those limitations by developing a novel constitutive model capable of predicting the stress-strain relaxation behavior of austenitic stainless steels when pre-deformed at low-to-high temperatures (*e.g.* cold or hot rolling), and subsequently exposed at high temperatures. For that purpose, a physically-inspired approach is proposed.

Austenitic stainless steels are low-to-moderate stacking fault energy (SFE) FCC polycrystals that can experience deformation twinning (see overview by Karaman et al. (2002)) and where

the associated strain hardening behavior have been largely studied (*e.g.* (Asgari et al., 1997; El-Danaf et al., 2001; Kalidindi, 1998)). At low temperatures, the development of deformation twins was found to induce high strain hardening due to complex slip-twin and twin-twin interactions. A certain number of physically-based macroscopic constitutive models that include the effect of deformation twinning on strain hardening have been proposed. Most are based on the idea that deformation twins act as microstructural barriers to gliding dislocations (Allain et al., 2004; Bouaziz and Guelton, 2001; Huang et al., 2011; Rémy, 1978; Steinmetz et al., 2013). Such assumption was motivated by earlier TEM work by Karaman et al. (2001a); Rémy (1981); Venables (1964). In these models, deformation twinning is usually quantified through a twin volume fraction which is measured from experimental observations. This twin volume fraction is usually taken into account in a mean free path which controls the dislocation generation and thus, a part of the material deformation hardening. Some models incorporate the effect of deformation twinning on the development of internal stresses (e.g. (Bouaziz et al., 2008)). They are assumed to arise from dislocation pileups at twin boundaries (*i.e.* $\Sigma 3$ boundaries) as observed by TEM in a Hadfield steel (Karaman et al., 2001b). A comprehensive review of the models which accounts for twinning in low SFE FCC metals can be found in (Steinmetz et al., 2013). Deformation twinning occurrence is known to decrease with increasing temperatures. Such phenomenon is generally attributed to the increase of the material SFE with increasing temperature (Lecroisey, 1971). In many models, e.g. (Steinmetz et al., 2013), the SFE plays a large role in defining a critical twinning stress above which deformation twinning occurs. High temperatures may also lead to the reduction in the material dislocation density (*i.e.* static recovery) which accelerates stress relaxation, especially when the initial dislocation density is high (*e.g.* cold rolled material). Some models have been proposed to account for static recovery at high temperatures in FCC materials (Lagneborg, 1969; Militzer et al., 1994; Nix et al., 1985; Sandström and Lagneborg, 1975) including in AISI 316L stainless steels (Lindgren et al., 2008).

One of the goals of the constitutive model proposed in this work is to describe the high temperature stress relaxation. The particular temperature range of interest for an austenitic stainless steel, such as AISI 316L-type, is 550-600°C. Under these conditions, stress relaxation can be described by a classical viscoplasticity framework. Strain-rate sensitivity depends on the level of stress at a given temperature. Generally, strain rate sensitivity at a given temperature varies non-linearly with stress, thus a power law flow rule is not suitable to describe such behavior. Instead, either an hyperbolic sine (*e.g.* (Delobelle and Oytana, 1984)) or exponential function (Busso and McClintock, 1996; Cheong and Busso, 2004; Kocks et al., 1975) is more suitable. Recently, the exponential flow rule was used to reproduce the micromechanical deformation of an AISI 316H steel at room temperature followed by a uniaxial tension at elevated temperature (550°C) (Li et al., 2013).

The work presented here describes a physics-inspired viscoplastic constitutive theory for large deformations with microstructure-related length scales which should be applicable to moderate and low stacking fault energy (SFE) face centered cubic (FCC) materials. The paper is organised as follows. The microstructure evolution observed by SEM-EBSD in a deformed AISI 316L steel including deformation twinning is described and quantified. Then the constitutive model is presented. This is followed by a description of the model calibration methodology to reproduce the mechanical responses of the AISI 316L steel of interest after cold rolling. Finally, the constitutive model is applied to study the residual stress partially responsible for RC in the notch root regions of CT-like specimens machined from cold rolled AISI 316L austenitic stainless steel.

Throughout the paper, standard tensorial notation will be used. Vectors will be described by

boldface lower case letters, second-order tensors by boldface upper case letters, and fourth-order tensors by italic upper case letters. Also $\mathbf{A} : \mathbf{B} = A_{ij}B_{ij}$, $\mathbf{AB} = A_{ij}B_{jk}$, $\mathcal{C} : \mathbf{A} = C_{ijkl}A_{kl}$ and $\mathbf{a} \otimes \mathbf{b} = a_i b_j$ where Einstein summation applies for repeated indices. Furthermore, the transpose of a tensor $\mathbf{A}$ is noted $\mathbf{A}^T$.

3.2 Microstructure and deformation twinning quantification

3.2.1 Material

The material of interest is an AISI 316L austenitic stainless steel containing 0.033 wt.% carbon and 0.025 wt.% nitrogen. It was received in the form of a 14 mm-thick hot rolled sheet, annealed at 1373 K for 30 min before water quenching. SEM observations and EBSD analyses showed the microstructure to be composed of equiaxed austenitic grains containing annealing twins and showing no crystallographic texture, see Figure 3.1a (RD and TD stand for the rolling and the transverse directions, respectively). The grain size measured from EBSD images was found to be 34±25 μm when considering $\Sigma 3$ annealing twin boundaries as grain boundaries (GBs), and 72±49 μm otherwise. From EBSD analyses, it was found that the material microstructure after 21% cold rolling exihibited deformation twins, see Figure 3.1b.

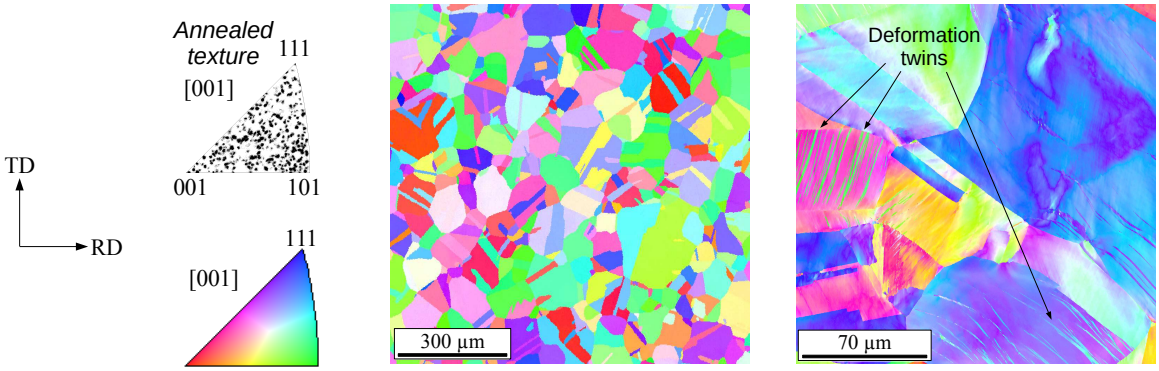

Figure 3.1: Inverse pole figure (IPF) map of the AISI 316L steel in (a) the annealed state and (b) after 21% cold rolling (close-up view).

3.2.2 Deformation twinning

In order to quantify the twinning evolution with deformation, axisymmetric tensile specimens with a diameter of 4.5 mm were deformed at different temperatures and up to different levels of plastic deformation under a strain rate of $\sim 10^{-2}$ s^{-1}. Then, these specimens were sectioned normal to the tensile direction to analyse the deformed microstructure. To obtain an appropriate surface state for SEM analyses, a low-speed saw was used and the surfaces were polished using grinding papers (from 40 to 3 μm), diamond pastes (from 3 to 1 μm) and a solution of colloidal silica (5 min). Subsequently, 200×200 μm^2 EBSD maps were acquired from these surfaces using a FEI Nova NanoSEM 450 microscope with a field emission gun coupled with an EDAX TSL Hikari camera running with OIM system. The acceleration voltage was 20 kV, the working distance was close to 14 mm and a step size of 0.1 μm following an hexagonal grid. The data acquired by EBSD were filtered with a dilatation procedure to obtain a minimum grain area of 5 points

with a minimum misorientation of 2° between adjacent grains (*e.g.* see Figure 3.2(a)). Then, the twins were isolated from the IPF maps (*e.g.* see Figure 3.2(b)), and the twin surface fractions were then measured from the resulting images as the ratio of black pixels to total number of pixels. The twin volume fraction was assumed to be identical to the twin surface fraction from the stereological equivalence between surface and volume fractions (Delesse, 1848; Underwood, 1970). The measured twin volume fraction values found in the tensile specimens deformed at different temperatures and levels of plastic deformation are shown in Figure 3.3. The minimum and maximum values of each measurement given in this figure were obtained after an erosion and a dilation procedure by one pixel applied to the binarised images. Deformation twinning was found to decrease with increasing temperature and to increase with increasing plastic strain. At 600°C, no deformation twins were observed.

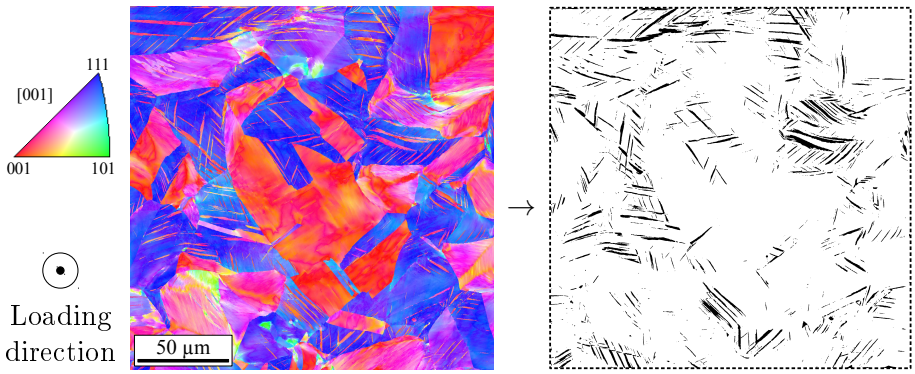

Figure 3.2: (a) EBSD-IPF map of the AISI 316L steel after 31% true strain at 100°C and (b) binarised twins isolated from (a) (here, the twin volume fraction is ∼6.5%)

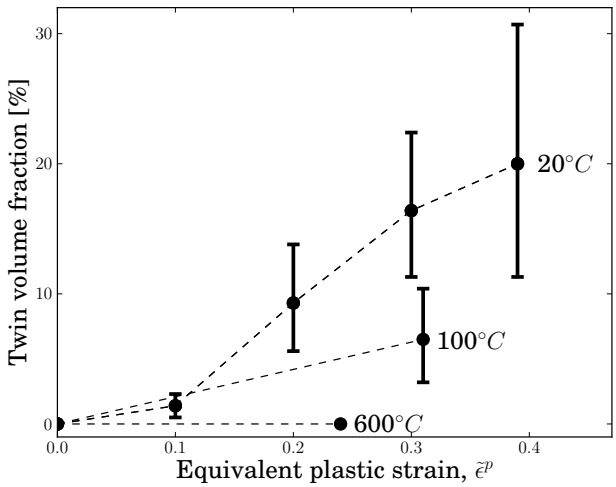

Figure 3.3: Twin volume fraction evolution with plastic deformation and temperature

3.3 Constitutive model formulation

3.3.1 Selection of the internal state variables and material flow stress

The formation of the microstructural boundaries ($\Sigma 3$, $60°/<111>$) associated with deformation twinning is assumed to increase the hardening behaviour of the material by reducing the mean free path of gliding dislocations in the bulk material. In this austenitic steel, the motion of perfect dislocations (in $\{111\}$ planes along the $<110>$ direction) was assumed to be opposed by (i) microstructural obstacles that can be overcome by thermal activation: such as Peierls valleys, substitional (mainly Cr and Ni) and interstitial (mainly C and N) atoms that create lattice distortions, and (ii) microstructural obstacles that cannot be overcome by thermal activation : such as dislocation forest, GBs and deformation twins. Here, the total resistance opposed by the first type of obstacles will be called the lattice friction resistance, S^*, and is assumed to be a function of the absolute temperature, θ, and strain rate, $\dot{\epsilon}$, thus, $S^* = \hat{S}^*\{\theta, \dot{\tilde{\epsilon}}\}$. The strengthening effect of the other type of obstacles will be designated as deformation resistance, S, and is assumed to only depend on the temperature through the evolution of the elastic parameters (François et al., 2012).

Other microstructural obstacles in AISI 316L-type steels can be found when exposed at different temperatures, ageing times and/or loading conditions that are not considered in this study. For example, martensitic transformation can occur at low temperatures. Furthermore, other microstructural obstacles, such as intermetallic phases (σ, ξ, η), inclusions (mostly, MnS) and carbides (mostly, $M_{23}C_6$ (Weiss and Stickler, 1972)) can be found in the 20-600°C temperature range but will not be accounted for in this work for simplicity. A detailed review of precipitation and secondary phase formation in austenitic stainless steels can be found in (Lo et al., 2009).

In order to link the deformation resistance, S, with the material microstructure, it will be assumed to be composed of two types of obstacles, each represented by a particular microstructural length scale as schematically illustrated in Figure 3.4:

- *Strong obstacles*: grain boundaries and twin boundaries.
  Considering the grain and twin boundaries as equivalent obstacles, a mean distance between strong obstacles, L_S, can be defined as,

$$\frac{1}{L_S} = \frac{1}{d_{GB}} + \frac{1}{d_T} \tag{3.1}$$

  where, d_T, is the mean distance between twins and, d_{GB}, is the mean distance between GBs that can be approximated as, $d_{GB} = 2/3 d_0$, when considering spherical grains of mean diameter d_0 (mean grain size). From stereological principles (Fullman, 1953), the mean distance between twins, d_T, is assumed to be a function of the twin volume fraction, f, and the mean twin thickness, e:

$$\frac{1}{d_T} = \frac{f}{2e(1-f)} \tag{3.2}$$

  Thus, the twin volume fraction measurements from Figure 3.3 can be used to determine the mean distance between twins when assuming a constant mean twin thickness.

- *Weak obstacles*: forest dislocations.
  The mean length scale associated with weak slip obstacles, L_W, is defined by the mean

distance between dislocations, d_D:

$$\frac{1}{L_W} = \frac{1}{d_D} = \sqrt{\rho} \tag{3.3}$$

where, ρ, represents the macroscopic average dislocation density of the material.

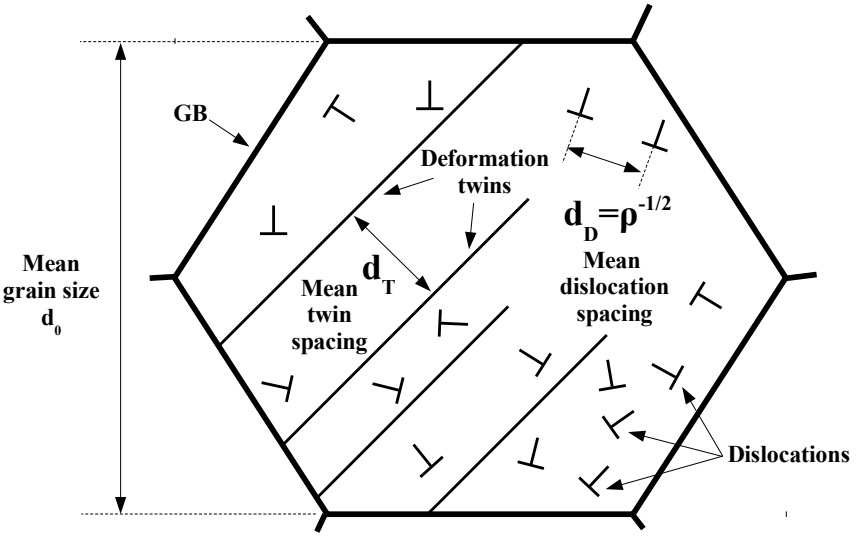

Figure 3.4: Schematic illustration of the microstructural length scales to be used in the constitutive model (ρ is the dislocation density).

These microstructural length scales defined in Eqs. 3.1 and 3.3 can be linked to the deformation resistance, S, by assuming the latter to be given by a combination of a Hall-Petch-type resistance, where twin obstacles are considered through the L_S length scale, and the classical forest dislocation resistance:

$$S = \underbrace{\frac{k_{HP}}{\sqrt{L_S}}}_{Hall-Petch-type\ resistance} + \underbrace{\frac{\alpha M \mu b}{L_W}}_{Forest\ dislocation\ resistance} \tag{3.4}$$

where, k_{HP}, is the Hall-Petch pre-factor, M, is the Taylor factor, b is the magnitude of the Burgers vector, μ is the shear modulus and α is a parameter which accounts for the spatial distribution of the dislocation forests.

The material flow stress is assumed to be given by the sum of the deformation resistance, S, the lattice friction resistance, S^* and an internal stress, $\tilde{B}$, associated with the polarisation of the dislocation structure during deformation. Thus,

$$\tilde{\sigma} = S^* + S + \tilde{B} \tag{3.5}$$

Recalling that $S^* = \hat{S}^*\{\theta, \dot{\tilde{\epsilon}}\}$ and $S = \hat{S}\{\rho, f\}$, then Eq.3.5 can be inverted to obtain the inelastic strain rate as a function of the loading $(\tilde{\sigma}, \theta)$ and the internal state variables $(\rho, f, \tilde{B})$:

$$\dot{\tilde{\epsilon}}^p = \hat{\dot{\tilde{\epsilon}}}^p\{\tilde{\sigma}, \theta, \rho, f, \tilde{B}\} \tag{3.6}$$

where elastic strain rate effects have been neglected.

3.3.2 Finite strain kinematics framework

The constitutive model is next formulated within a continuum mechanics framework for finite strain kinematics (see *e.g.* (Besson et al., 2009)). Description of deformation relies on the objective tensor of the total deformation gradient $\mathbf{F}$. The associated volumetric dilatation, J, is,

$$J = \det \mathbf{F} \tag{3.7}$$

The non-symmetric tensor of the total deformation rate gradient, $\mathbf{L}$, defined as,

$$\mathbf{L} = \dot{\mathbf{F}}\mathbf{F}^{-1} \tag{3.8}$$

can be divided into an objective symmetric and a non-objective antisymmetric tensor, $\mathbf{D}$ and $\mathbf{\Omega}$, respectively, since,

$$\mathbf{L} = \mathbf{D} + \mathbf{\Omega} \quad with, \quad \mathbf{D} = \frac{1}{2}(\mathbf{L} + \mathbf{L}^T) \quad and \quad \mathbf{\Omega} = \frac{1}{2}(\mathbf{L} - \mathbf{L}^T) \tag{3.9}$$

A corotational finite strain formulation is considered here. Passing from the global to the local reference frames is described by a rotation, $\mathbf{Q}$, defined as (Lush et al., 1989):

$$\dot{\mathbf{Q}} = \mathbf{\Omega}\mathbf{Q} \ \ with, \ \ \mathbf{Q}_0 = \mathbf{I} \tag{3.10}$$

with, $\mathbf{\Omega}$, the antisymmetric part of $\mathbf{L}$ (see Equation 3.9), $\mathbf{Q}_0$, the initial value of $\mathbf{Q}$ and, $\mathbf{I}$, the second-order identity tensor. In the local reference frame, a generic second-order tensor, $\mathbf{X}$, can thus be expressed from its un-rotated form expressed in the initial reference frame, $\overline{\mathbf{X}}$:

$$\mathbf{X} = \mathbf{Q}^T\overline{\mathbf{X}}\mathbf{Q} \tag{3.11}$$

The corotational method enables the model flow and evolutionary constitutive equations to be written in the same form as those for infinitesimal strains. Thus, the formulation becomes equivalent to the one expressed in terms of an objective time derivative, such as the Jaumann rate of the Cauchy stress. In the next section, all second-order tensors will be assumed to have been pushed forwards to the local material frame.

3.3.3 Stress-strain relation and flow rule

When formulating the model within a corotational framework, the rate of change of the Kirchhoff stress $\mathbf{T}$ is expressed as:

$$\dot{\mathbf{T}} = \mathcal{L} : (\mathbf{D} - \mathbf{D}^p) \tag{3.12}$$

where, $\mathbf{D}$ and $\mathbf{D}^p$, are the total and the viscoplastic deformation rate tensors, respectively, and, $\mathcal{L}$, is the fourth-order elasticity tensor that is given by,

$$\mathcal{L} = 2\mu\mathcal{I} + \left[\kappa - \frac{2}{3}\mu\right]\mathbf{I} \otimes \mathbf{I} \tag{3.13}$$

where, κ, is the isotropic bulk modulus of the material and, $\mathcal{I}$, is the fourth-order identity tensor. The Cauchy stress, $\boldsymbol{\sigma}$, is related to the Kirchhoff stress through the relation: $J\boldsymbol{\sigma} = \mathbf{T}$.

The equivalent viscoplastic strain rate, $\dot{\epsilon}^p$, is assumed to be composed of a component due to the slip arising from dislocation motion in the untwinned material, $\dot{\epsilon}^p_g$, and one due to mechanical

twinning (Rémy, 1978). Here,

$$\dot{\epsilon}^p = (1-f)\dot{\epsilon}^p_g + \frac{\gamma_p}{\sqrt{3}M}\dot{f} \tag{3.14}$$

where, γ_p, is the shear strain produced by the glide of a single partial dislocation. For a face-centered cubic system, $\gamma_p = \frac{1}{\sqrt{2}}$. The viscoplastic strain rate component due to slip, $\dot{\epsilon}^p_g$, accounts for the thermally-activated motion of dislocations through the following expression,

$$\dot{\epsilon}^p_g = \dot{\epsilon}_0 \exp\left\{-\frac{\Delta G}{\mathcal{K}\theta}\right\} \tag{3.15}$$

where, θ, is the absolute temperature, $\mathcal{K}$, the Boltzmann constant and, $\dot{\epsilon}_0$, a pre-exponential factor. The activation energy, ΔG, corresponds to the energy needed for dislocations to free from their pinning points. A convenient form for ΔG (see (Busso, 1990; Kocks et al., 1975)) is assumed to be a decreasing function of the lattice friction stress, σ^*, normalised by the lattice friction stress above which dislocations can be mobilised without the assistance of thermal activation,$\hat{\sigma}$. Then,

$$\Delta G = G_0\left[1-\left(\frac{\sigma^*}{\hat{\sigma}}\right)^p\right]^q \tag{3.16}$$

where, p and q, are shape parameters used to adjust the shape of the flow stress *vs* temperature and strain rate relations. Admissible acceptable ranges for p and q were found by Kocks et al. (1975) to be $0 < p \leq 1$ and $1 \leq q \leq 2$. The lattice friction stress, σ^*, can be expressed as:

$$\sigma^* = \tilde{\sigma}^e - S \tag{3.17}$$

with, $\tilde{\sigma}^e$, the effective stress defined as, $\tilde{\sigma}^e = \sqrt{\frac{3}{2}(\mathbf{T}'-\mathbf{B}):(\mathbf{T}'-\mathbf{B})}$, where, $\mathbf{T}'$, is the deviatoric component of the Kirchhoff stress tensor and, $\mathbf{B}$, is the internal stress tensor with $\tilde{B} = \sqrt{\frac{3}{2}\mathbf{B}:\mathbf{B}}$. Combining Eqs. 3.15-3.17 gives an expression for the equivalent viscoplastic strain rate due to dislocation gliding, $\dot{\epsilon}^p_g$, in terms of effective stress, $\tilde{\sigma}^e$, absolute temperature, θ, and the material microstructure through the deformation resistance, S, (Busso, 1990; Busso and McClintock, 1996; Cheong and Busso, 2004):

$$\dot{\epsilon}^p_g = \dot{\epsilon}_0 \exp\left\{-\frac{G_0}{\mathcal{K}\theta}\left[1-\left\langle\frac{\tilde{\sigma}^e - S}{\hat{\sigma}}\right\rangle^p\right]^q\right\} \tag{3.18}$$

where the notation $\langle\ \rangle$ corresponds to the Macauley brackets : $\langle x\rangle = x$ if $x > 0$ and is 0 elsewhere. In Eq.3.18, $\hat{\sigma}$ can be approximated by the product of the lattice friction resistance at 0 K, S^*_0, with the ratio of the shear modulus at the temperature of interest to that at 0 K to reduce all elastic interactions to 0 K (Busso and McClintock, 1996):

$$\hat{\sigma} = S^*_0\frac{\mu}{\mu_0} \tag{3.19}$$

By inverting Equation 3.18, and assuming $\dot{\epsilon}^p \sim \dot{\epsilon}$, the actual form of Equation 3.5 can be obtained:

$$\tilde{\sigma} = S^*_0\frac{\mu}{\mu_0}\left[1-\left(\frac{\theta}{\theta_0}\right)^{\frac{1}{q}}\right]^{\frac{1}{p}} + S + \tilde{B}, \qquad with\ \ \theta_0 = \frac{G_0}{\mathcal{K}\ln\left(\dot{\epsilon}_0/\dot{\epsilon}\right)} \tag{3.20}$$

where the first term is the lattice friction resistance. In the flow rule relation, the material parameters to be calibrated are $\dot{\epsilon}_0$, G_0, S^*_0, p and q. The flow stress dependence on the temperature

and strain rate is schematically represented in Figure 3.5 (no internal stresses are assumed here, i.e. $\tilde{B} = 0$ for simplicity).

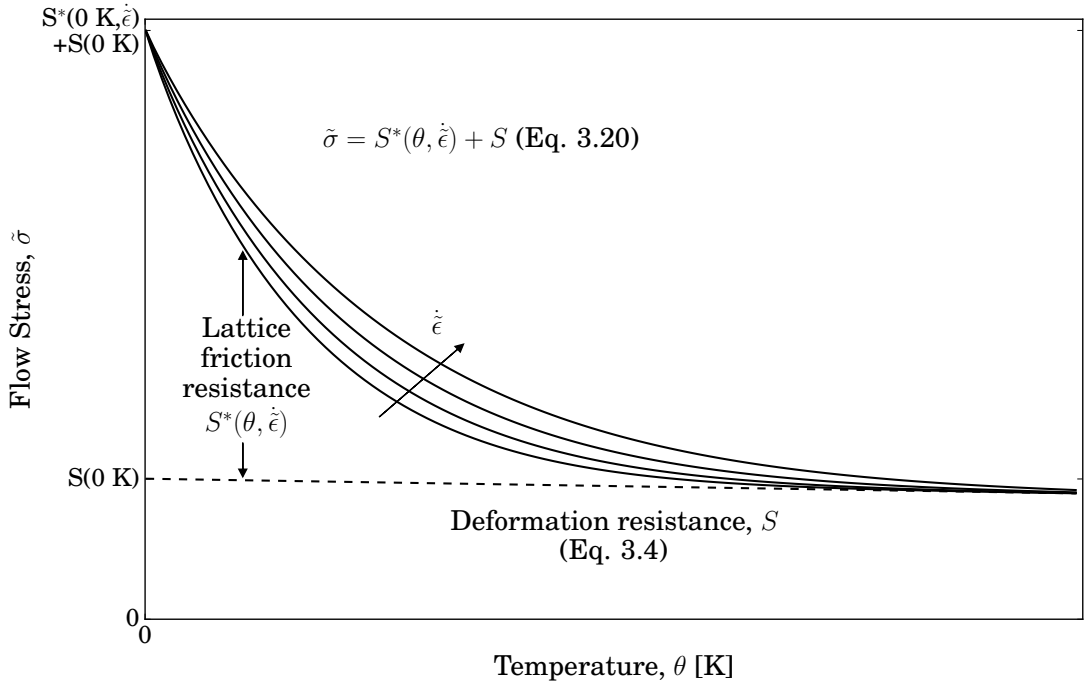

Figure 3.5: Schematic representation of the flow stress evolution with the absolute temperature and the strain rate.

The flow rule links the magnitude of the equivalent viscoplastic strain rate, given by $\dot{\tilde{\epsilon}}^p$, and the flow direction, $\mathbf{N}$, with the viscoplastic deformation rate tensor, $\mathbf{D}^p$. The flow direction is given by $\mathbf{T}' - \mathbf{B}$:

$$\mathbf{D}^p = \dot{\tilde{\epsilon}}^p \mathbf{N} = \frac{3}{2} \dot{\tilde{\epsilon}}^p \frac{(\mathbf{T}' - \mathbf{B})}{\tilde{\sigma}^e} \tag{3.21}$$

Similarly, the viscoplastic deformation rate tensor resulting from the dislocation gliding, noted $\mathbf{D}^p_g$, can be defined as:

$$\mathbf{D}^p_g = \frac{3}{2} \dot{\tilde{\epsilon}}^p_g \frac{(\mathbf{T}' - \mathbf{B})}{\tilde{\sigma}^e} \tag{3.22}$$

3.3.4 Dislocation density evolutionary equations

The evolution of the dislocation density, ρ, was chosen to result from the competition between three mechanisms: dislocation storage ($\dot{\rho}_H$), dynamic recovery ($\dot{\rho}_{DR}$) and static recovery ($\dot{\rho}_{SR}$). Thus,

$$\dot{\rho} = \dot{\rho}_H + \dot{\rho}_{DR} + \dot{\rho}_{SR} \tag{3.23}$$

The storage term corresponds to the length of dislocation stored per swept unit area (Kocks, 1966)(Kocks and Mecking, 2003):

$$\dot{\rho}_H = \frac{M}{b}\left[\frac{1}{L_S} + \frac{K}{L_W}\right]\dot{\bar{\epsilon}}_g^p \tag{3.24}$$

where, K, is a material parameter.
The dynamic recovery term describes the dynamic annihilation mechanism of opposite signed dislocations that occurs when they attained a critical distance, d, (Cheong and Busso, 2004):

$$\dot{\rho}_{DR} = -\frac{M}{b}2d\rho\dot{\bar{\epsilon}}_g^p \tag{3.25}$$

The static recovery term describes the effect of diffusion-assisted dislocation climb which reduces the density of immobile dislocations (Lagneborg, 1972)(Lindgren et al., 2008):

$$\dot{\rho}_{SR} = -\Gamma\frac{\mu b^3}{\mathcal{K}\theta}\langle\rho^2 - \rho_{eq}^2(\theta)\rangle \tag{3.26}$$

with, Γ, is the effective lattice diffusivity. The latter can be expressed with an Arrhenius equation where, Γ_0, is the frequency factor and, Q, is the activation energy: $\Gamma = \Gamma_0 e^{-\frac{Q}{\mathcal{K}\theta}}$. Here, $\rho_{eq}^2(\theta)$ is the equilibrium dislocation density at the absolute temperature θ.
Substitution of Eqs. 3.24-3.26 into 3.23 gives,

$$\dot{\rho} = \frac{M}{b}\left[\frac{1}{L_S} + \frac{K}{L_W} - 2d\rho\right]\dot{\bar{\epsilon}}_g^p - \Gamma_0 e^{-\frac{Q}{\mathcal{K}\theta}}\frac{\mu b^3}{\mathcal{K}\theta}\langle\rho^2 - \rho_{eq}^2(\theta)\rangle \tag{3.27}$$

The parameters to be calibrated are K, d, Γ_0, Q.

3.3.5 Internal stress tensor

The internal stresses are assumed to result from contributions arising from the plastic strain incompatibilities between crystallographical boundaries (*i.e.* at GBs and at twin boundaries) and the polarisation of the dislocation structure during deformation inside the grains. During plastic deformation, dislocations piled-up against GBs are known to impose stress concentrations that contribute to the formation of long-range internal stresses (Feaugas, 1999). Furthermore, TEM observations by Karaman et al. (2001a) have shown that dislocations can also pile-up against twin boundaries. Thus, the level of deformation twinning is assumed to contribute to the internal stresses. In this work, the internal stress tensor, $\mathbf{B}$, is divided into two parts: (i) intergranular stresses which result from the dislocation pileups at grain and at twin boundaries, and (ii) intragranular internal stresses resulting from the polarization of the dislocations structures within the grains. Thus,

$$\dot{\mathbf{B}} = \dot{\mathbf{B}}_I + \dot{\mathbf{B}}_{II} \tag{3.28}$$

The internal stress tensor evolutions, $\dot{\mathbf{B}}_I$ and $\dot{\mathbf{B}}_{II}$ are assumed to be both composed of a part arising from viscoplastic deformation, $\dot{\mathbf{B}}_{i_P}$ $(i = I, II)$, and a static recovery part $\dot{\mathbf{B}}_{i_{SR}}$. The latter was assumed to describe the internal stress decrease with time at high temperatures which is generally associated with thermally activated mechanisms such as dislocation climbing and the corresponding annihilation possibility (Chaboche, 2008). Thus,

$$\dot{\mathbf{B}}_i = \dot{\mathbf{B}}_{i_P} + \dot{\mathbf{B}}_{i_{SR}} \qquad for \quad i = I, II \tag{3.29}$$

The intergranular internal stress tensor evolution arising from inelastic deformation, $\dot{\mathbf{B}}_{i_P}$, is inspired from the unidimensional equation proposed by Sinclair et al. (2006) to describe a grain size dependent internal stress evolution and adapted by Bouaziz et al. (2008) to take into account twinning. Here, the internal stress evolution equation is formulated in a tensorial form. The first term describes the piling-up of dislocations at strong obstacles and is controlled by the mean distance between pile-ups, λ, the mean distance between strong obstacles, L_S, and the viscoplastic deformation rate tensor, $\mathbf{D}^p$, the second one induces the internal stresses saturation from the finite number of dislocations, m_0, allowed per pile-up. Thus, the maximal equivalent intergranular internal stress is $\frac{M\mu b}{L_S} m_0$. Here,

$$\dot{\mathbf{B}}_{I_P} = \frac{\lambda}{b}\left[\frac{2}{3}\frac{M\mu b}{L_S}\mathbf{D}^p_g - \frac{1}{m_0}\mathbf{B}_I\dot{\bar{e}}^p_g\right] \tag{3.30}$$

When no twinning occurs (*e.g.* at low strain and/or high temperature conditions), $L_S = d_G$, thus, only grain boundaries act as barriers which induce the development of intergranular internal stresses.
The static recovery term, $\dot{\mathbf{B}}_{I_{SR}}$, proposed below follows the forest dislocation static recovery kinetics through the $\dot{\rho}_{SR}$ variable (Equation 3.26). It is built from the assumption that the internal stress magnitude can be approximated to be proportional to the forest dislocation resistance, thus $\tilde{X} \sim \beta M\mu b\rho^{1/2}$, where $\tilde{X}$ is a generic equivalent internal stress and β a unitless parameter. Then, the associated internal stress static recovery rate was obtained by deriving the previous expression, thus $\dot{\tilde{X}}_{SR} \sim \beta\frac{M\mu b}{2\sqrt{\rho}}\dot{\rho}_{SR}$. Furthermore, the internal stress static recovery direction can be approximated as $\mathbf{X}/\tilde{X}$. Consequently, the static recovery term of the intergranular internal stress tensor was expressed as,

$$\dot{\mathbf{B}}_{I_{SR}} = \beta\frac{M\mu b}{2\sqrt{\rho}}\frac{\mathbf{B}_I}{\tilde{B}_I}\dot{\rho}_{SR} \tag{3.31}$$

Combining, Eqs 3.30 and 3.31 gives the full expression of $\dot{\mathbf{B}}_I$:

$$\dot{\mathbf{B}}_I = \frac{\lambda}{b}\left[\frac{2}{3}\frac{M\mu b}{L_S}\mathbf{D}^p_g - \frac{1}{m_0}\mathbf{B}_I\dot{\bar{e}}^p_g\right] - \beta\frac{M\mu b}{2\sqrt{\rho}}\frac{\mathbf{B}_I}{\tilde{B}_I}\dot{\rho}_{SR} \tag{3.32}$$

where the parameters to be calibrated are λ, m_0 and β.

The evolution of intragranular internal stresses associated with the polarisation of the dislocation structure within the grains is assumed to follow a classical Armstrong-Frederick-type non-linear hardening phenomenological relation. Those intragranular internal stresses are also assumed to follow a similar static recovery relation as in Equation 3.32:

$$\dot{\mathbf{B}}_{II} = \frac{2}{3}c_1\mathbf{D}^p_g - c_2\mathbf{B}_{II}\dot{\bar{e}}^p_g - \beta\frac{M\mu b}{2\sqrt{\rho}}\frac{\mathbf{B}_{II}}{\tilde{B}_{II}}\dot{\rho}_{SR} \tag{3.33}$$

where, c_1, is a parameter describing the initial slope of internal stress evolution and, c_2, is a parameter which defines saturation at a value of c_1/c_2. The parameters to be calibrated in this equation are c_1 and c_2 (the value of β is the same as in Equation 3.32 for simplicity).

3.3.6 Evolution of the twin volume fraction

The twin volume fraction evolution, $\dot{f}$, can be expressed as the volumetric nucleation rate, $\dot{n}$, in the untwinned material multiplied by the volume occupied by a twin,v, (Rémy, 1978). Thus,

$$\dot{f} = (1-f)v\dot{n} \tag{3.34}$$

The deformation twins are assumed to be disc-shaped with a mean thickness, e. The initial twin diameter is assumed to be, d_0, and to decrease to zero when the material is entirely twinned (i.e. $f = 1$). The volume of a single newly created twin can thus be approximated as:

$$v = \frac{\pi[(1-f)d_0]^2}{4}e \tag{3.35}$$

The twin nucleation rate is assumed to depend on the effective stress, a critical twinning stress, $\tilde{\sigma}^c$, and the viscoplastic strain rate (Steinmetz et al., 2013). Here, a simple phenomenological power law is assumed:

$$\dot{n} = n_0 \left(\frac{\tilde{\sigma}^e}{\tilde{\sigma}^c}\right)^{\ell} \dot{\epsilon}_g^p \tag{3.36}$$

where n_0 and ℓ, are parameters to be calibrated.
As an approximation to the results by Venables (1964), this critical twinning stress was assumed to be a square root function of the stacking fault energy, γ:

$$\tilde{\sigma}^c = a_t\sqrt{\gamma} \tag{3.37}$$

where a_t is a parameter to be determined.
Furthermore, the stacking fault energy is assumed to be a linear function of the absolute temperature, θ, (Lecroisey, 1971):

$$\gamma = a_\gamma\theta + \gamma_0 \tag{3.38}$$

Combining Eqs. 3.34 to 3.37 leads to the following expression for $\dot{f}$:

$$\dot{f} = \frac{\pi}{4}d_0^2 e(1-f)^3 n_0 \left(\frac{\tilde{\sigma}^e}{a_t\sqrt{\gamma}}\right)^{\ell} \dot{\epsilon}_g^p \tag{3.39}$$

It should be noted that the increase of the twin volume fraction becomes significant when $\tilde{\sigma}^e > \tilde{\sigma}^c$. Furthermore, since $\tilde{\sigma}^c$ is assumed to increase with temperature through its dependence with the stacking fault energy, twinning occurs at higher strains when the temperature increases.

The constitutive model described above was explicitly implemented into Z-set finite-element software (Zset, 2015) as a user-defined material subroutine.

3.4 Determination of material parameters

3.4.1 Mechanical tests

The constitutive model was calibrated using experimental data on the AISI 316L steel taken from the literature and obtained as part of this work. The latter involved the following type of tests:

- *Monotonic tensile tests* performed at temperatures ranging from -100°C to 600°C and with strain rates of 5×10^{-2} and 5×10^{-4} s^{-1}, using an MTS 810 100 kN servo-hydraulic testing machine. A contact extensometer was used at -100, 20 and 100°C, whereas an image correlation technique was used at 600°C to measure axial strain.
- *Stress reversal tests* performed at 20 and 600°C, imposing an equivalent strain rate of 5×10^{-2} s^{-1}.
- *Stress relaxation tests* performed at 550 and 600°C, on a lever arm system Adamel TR3 testing machine. The tensile loading was strain controlled with a strain rate of 10^{-4} s^{-1} until a true inelastic strain of 0.05, then the true total strain was kept constant for about 350 h.

The calibration was based on tests performed using specimens machined from the annealed material. In addition, axisymmetric specimens machined from 21% cold rolled plates were tested for the needs of the residual stress problem presented in section 3.5.

3.4.2 Flow stress calibration

In the annealed state, the flow stress (see Equation 3.20) only depends on the temperature, the strain rate and the initial deformation resistance. The latter depends on the grain size and the initial dislocation density, ρ_0. Since no deformation twins were observed in the annealed material and no internal stresses are expected, it can be assumed that $f = 0$ and $\mathbf{B}_i = \mathbf{0}$ for i = I,II. The flow stress parameters were calibrated on the experimental flow stress data extracted from the monotonic tensile tests of this work and from AISI 316L data collected from Reed et al. (1983). The proposed flow stress calibration procedure consisted of two parts: the calibration of (i) the initial deformation resistance parameters and (ii) of the lattice friction resistance parameters:

(i) Initial deformation resistance calibration

The initial value of the deformation resistance, S, was determined by calibrating the Equation 3.4 parameters:

- Hall-Petch-type part of S: the pre-factor k_{HP} was assumed to be approximately 300 MPa.μm$^{1/2}$ (Schwartz, 2011).
- Forest resistance part of S: α was set at 0.3 (Cheong and Busso, 2004), the Taylor factor, M, for FCC materials without crystallographic texture is 3.07 (François et al., 2012), the value of $b = \frac{\sqrt{2}}{2} a_0 = 0.2544$ nm with, a_0, the lattice parameter of an AISI 316L steel given by Weiss and Stickler (1972). The shear and the bulk moduli, respectively, μ and κ, were interpolated as linear functions of temperature, θ, from Young's modulus data given in (Lacombe et al., 1990) (using the Poisson's ratio, $\nu = 0.3$): $\mu = 85 - 0.03 \times \theta$ GPa and $\kappa = 184 - 0.065 \times \theta$ GPa (θ in K). Finally, the initial dislocation density was adjusted to reach the material deformation resistance found at high temperature. The calibrated initial dislocation density found by this method was 5.2×10^{12} m^{-2} which is plausible for an annealed austenitic stainless steel.

(ii) Lattice friction resistance calibration

The five flow parameters $(\dot{\tilde{\epsilon}}_0, G_0, S_0^*, p, q)$ from Equation 3.18 were adjusted to describe the experimental flow stress evolution presented in Figure 3.6. The friction stress resistance at 0 K

was determined using data from the literature (Reed et al., 1983): at 0 K, $\tilde{\sigma}_f - S = S_0^* = 473$ MPa. The exponential pre-factor, $\dot{\tilde{\epsilon}}_0$, was set at 10^5 s^{-1}. The three remaining parameters were numerically optimised: $G_0 = 4.6 \times 10^{-19}$ J was found to satisfactorily match experimental results and is close to the value of 4.75×10^{-19} J found for a AISI 316H steel by Li et al. (2013). The values $p = 0.13$, and $q = 1.05$, enable a good description of the flow evolution with temperature and are within the admissible range given in subsection 3.3.3. The flow parameters and deformation resistance parameters are summarized in F, while the initial internal variable values for the annealed state are given in G. The flow stress calibration results are presented in Figure 3.6.

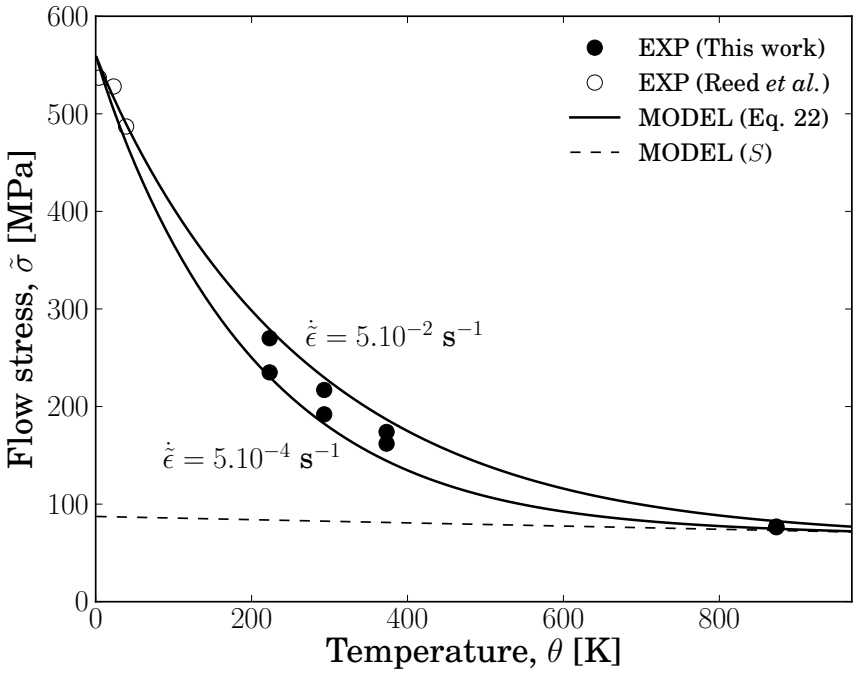

Figure 3.6: Flow stress (at 0.2% viscoplastic strain) evolution with temperature, θ, and equivalent strain rate, $\dot{\tilde{\epsilon}}$: comparison between the experimental data and Equation 3.20. The physical underlying structure of these curves is outlined in Figure 3.5.

3.4.3 Intrinsic twinning parameters

The evolution of the SFE with temperature was investigated by Lecroisey (1971), in a 16Cr-13Ni austenitic stainless steel. His experimental data were used to estimate the SFE evolution of the material in the -123 to 127°C temperature range (see Equation 3.38 and Figure 3.7a). The slope, $a_\gamma = 9 \times 10^{-2}$ mJ.m^{-2}.K^{-1} and the SFE at 0 K, $\gamma_0 = 0.46$ mJ.m^{-2} were identified by linear regression. Thus, at 20°C, the stacking fault energy was found to be 27 $mJ.m^{-2}$, which is within the range, 25 ± 5 mJ.m^{-2}, measured by Feaugas and Gaudin (2004) in an AISI 316L steel. For higher temperatures (*e.g.* 600°C), the stacking fault energy values were linearly extrapolated.

Twinning was assumed to be substantial when the critical twinning stress, $\tilde{\sigma}^c$, which increases with the stacking fault energy, is exceeded. Data collected on several FCC single crystal by François et al. (2012) were used to calibrate Equation 3.37, which describes the critical twinning stress evolution with the SFE (see Figure 3.7b). It should be noted that the initial experimental data from François et al. (2012) consisted of critical shear stress values and were multiplied by

the Taylor factor, M, to approximate $\tilde{\sigma}^c$ in this work. The value, $a_t = 3.10^9$ kg$^{0.5}$.m^{-1}.s^{-1} was found to satisfactorily predict the experimental data.

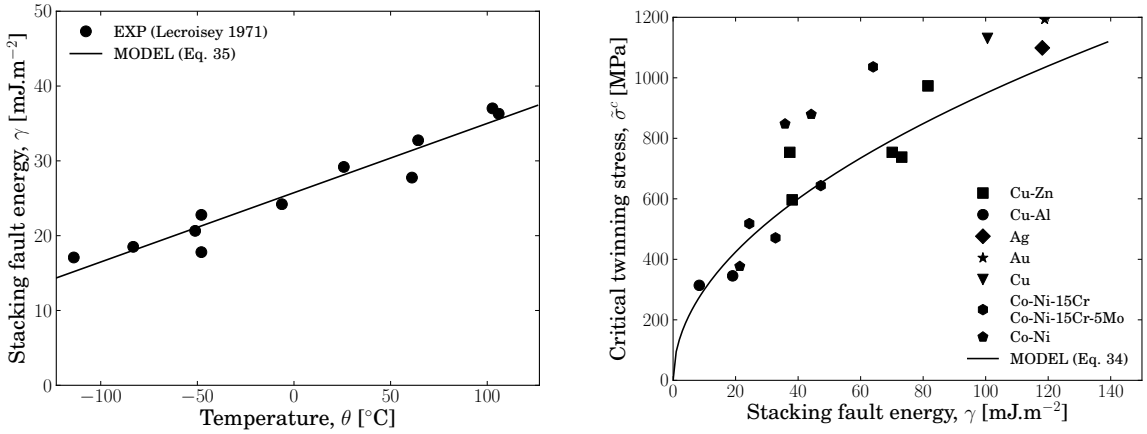

(a) (b)

Figure 3.7: (a) Stacking fault energy evolution with temperature and (b) critical twinning stress evolution with stacking fault energy.

3.4.4 Hardening parameters

In order to determine the hardening parameters of Eqs. 3.27, 3.30 and 3.33 and the remaining twinning parameters, n_0 and ℓ, in Equation 3.39, the constitutive model response was calibrated using the monotonic tensile and stress reversal tests (see respectively Figs. 3.8 and 3.9) and the microstructural measurements (see Figure 3.10).

The hardening parameters were calibrated as follows. First of all, since the mechanical tests of interest were performed at a strain rate of 5.10^{-2} s^{-1}, the static recovery terms in Eqs. 3.27 and 3.30 were disregarded by setting the value of Γ_0 in Equation 3.27 to zero. Then, twinning was switch off in order to pre-calibrate the hardening parameters for conditions where the twinning was assumed to be negligible (*i.e.* at 600°C or at low strain for tests performed at 20 and 100°C). The deactivation of twinning in the model was performed by setting $n_0 = 0$ in Equation 3.39. The distribution between the deformation resistance evolution - responsible for the isotropic hardening - and the internal stress evolution - responsible for the kinematic hardening - was estimated with the stress reversal data in Figure 3.9a. Finally, twinning was switched on and its hardening effect adjusted by calibrating the n_0 and ℓ parameters from the monotonic tensile tests and the microstructural measurements (see Figs. 3.8b and 3.10). The AISI 316L calibrated hardening parameters are given in F.

3.4.5 Model prediction of the 21% cold rolled material responses

The constitutive model is to be used in section 3.5 to predict the material response after 21% cold rolling including stress relaxation which has not been calibrated at this point. Firstly, the constitutive model ability to predict the material quasi-rate-independent response after 21% cold rolling is verified. The cold rolling process was numerically simulated in a volume element by imposing uniaxial strain-controlled compression on the volume element at room temperature assuming plane-strain conditions (no deformation in the transerve direction). Then, the internal

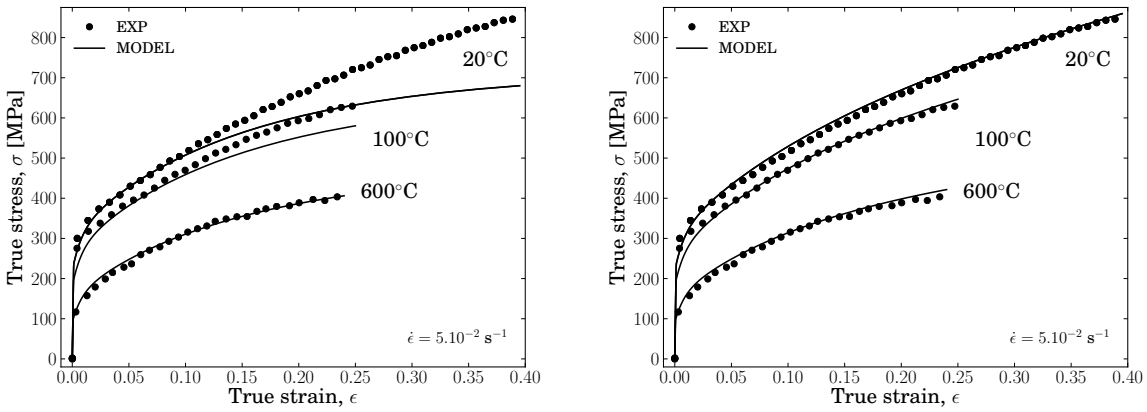

Figure 3.8: Model simulation of the monotonic tensile tests: (a) without and (b) with twinning.

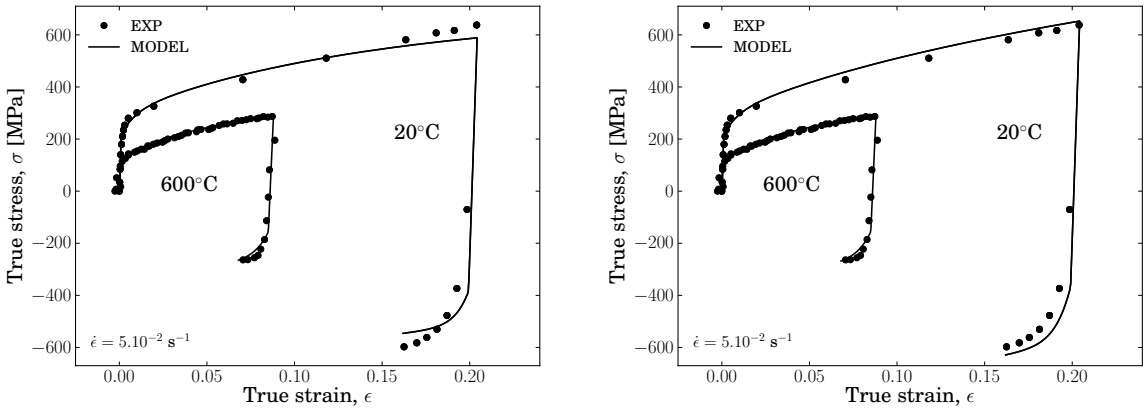

Figure 3.9: Model simulation of the stress reversal tests: (a) without and (b) with twinning.

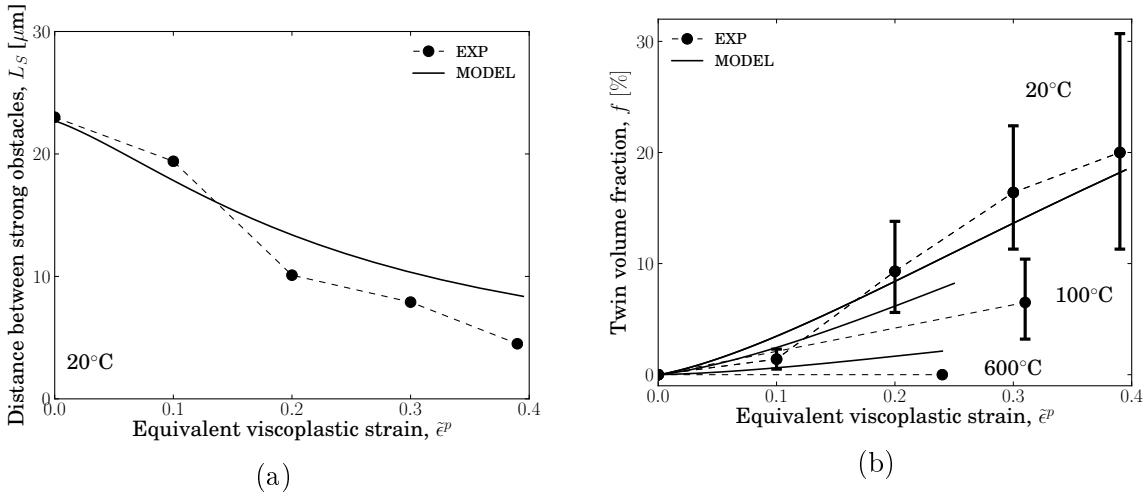

Figure 3.10: Comparison between the experimental measurements and the numerical simulations of (a) the mean distance between strong obstacles evolution at 20°C and (b) the twin volume fraction evolution with deformation at 20, 100 and 600°C.

variables values obtained at the end of this calculation (see appendix G) were set as initial ones for the prediction of the cold rolled state behavior. Figure 3.11 presents the cold rolled material response when tested in traction followed by a compression and in compression followed by a traction. The higher flow stress observed in the traction/compression test than in the compression/traction test are satisfactorily predicted by the model (due to the inital internal stresses) and confirm the constitutive model ability to predict the cold rolled material behavior at room temperature.

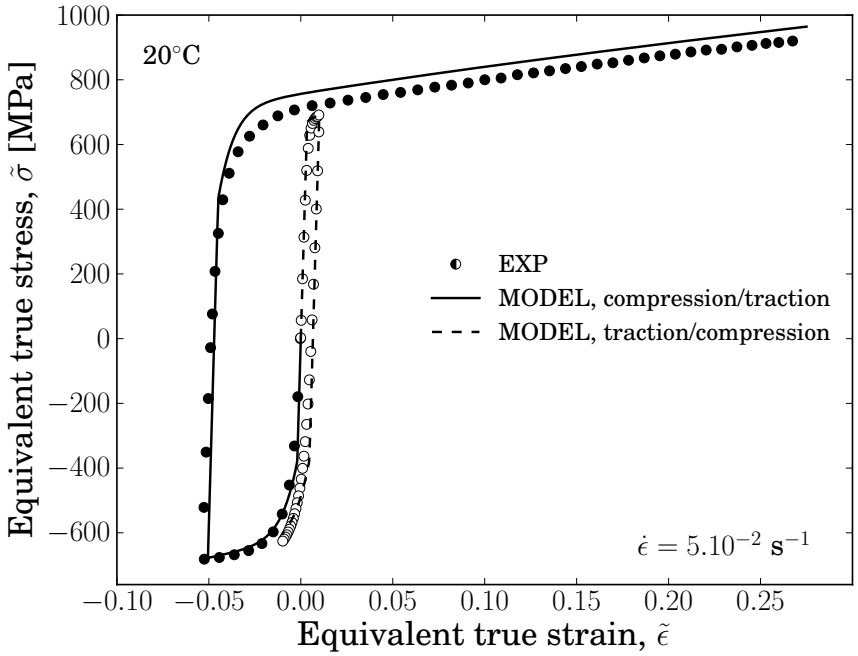

Figure 3.11: Comparison between the experimental data and the model prediction of the stress reversal tests using specimens machined from the 21% cold rolled material.

3.4.6 Static recovery parameters

The static recovery parameters control partially the material high temperature relaxation behavior by reducing the dislocation density (see Equation 3.27). For the requirement of section 3.5, they were calibrated on the 21% cold rolled state. Therefore, axisymmetric specimens were machined, along the RD, from the 21% cold rolled plate and tested at 550 and 600°C. The parameters Γ_0, Q and ρ_{eq} in Equation 3.27 and β in Eqs. 3.32 and 3.33 were adjusted to fit the stress relaxation data shown in Figure 3.12. The experimental data were extrapolated from $\sim$ 500 up to $>$ 3500 hrs for the needs of section 3.5. It was perfomed using the slopes of the experimental stress relaxation data when plotted in terms of $\log\sigma$ *vs* $\log\dot{\epsilon}^p$. Furthermore, the thermal activation description of static recovery and the temperature-dependent flow rule enabled the prediction of untested relaxation responses at other temperatures, *e.g.* the stress relaxation curve at 575°C in Figure 3.12. The calibrated static recovery parameters for AISI 316L are given in F. It should be noted that the equilibrium dislocation density, ρ_{eq}, was found to be 0 m^{-2} in the 550-600°C temperature range for the AISI 316L of interest but was found to be non zero for other AISI 316L-type steels (see Appendix E). Furthermore, the predicted dislocation densities

at the end of the stress relaxation tests are given in Appendix E.

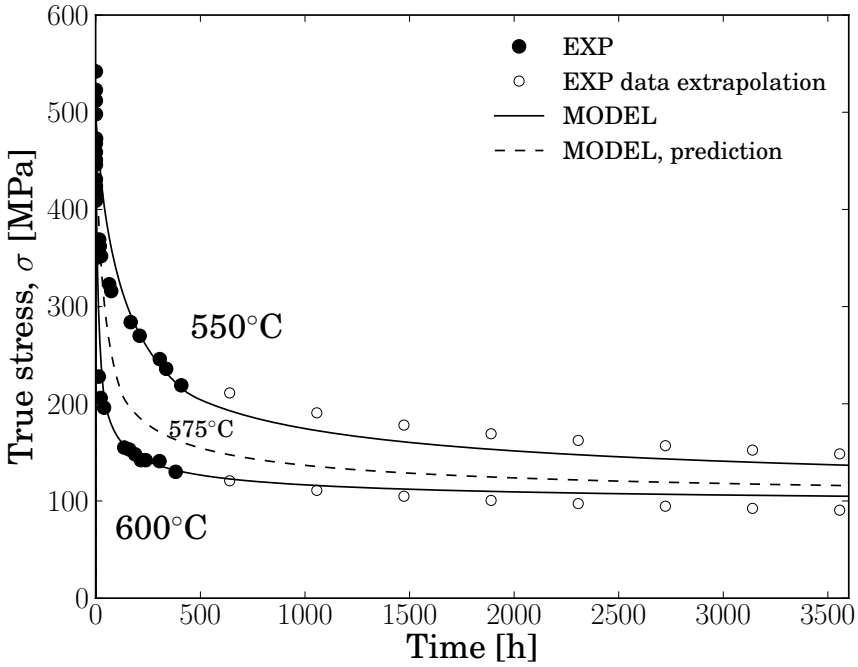

Figure 3.12: Model simulation of the stress relaxation tests using specimens machined from the 21% cold rolled material.

3.5 Application of the constitutive model to the prediction of residual stress fields in the notch root region of a CT-like specimen

In this section, the constitutive model was relied upon to study the evolution of residual stress fields in the notch root region of a CT-like specimen (see 3D geometry in Figure 3.13a) used to study reheat cracking in chapter 2. The CT specimens of interest were machined from a 21% cold rolled plate. Thus, the constitutive model parameters used here correspond to those identified earlier in the text (see Appendix F and G).

The residual stress introduction was done by compressing the CT-like specimen in the Y-direction with geometrically-adapted cylindrical-headed pieces. During compression, a confined plastically deformed zone was introduced in the notch root. Upon unloading, the balance of elastic strains in the specimen led to the formation of a tensile residual stress field whose magnitude is known to be maximum in the Y-direction close to the notch root (Sherry et al., 2002; Turski et al., 2008). Once the residual stress fields were present in the specimens, the latter were thermally exposed at 550, 575 or 600°C without loading during 4320 hours to enable the residual stress relaxation.

The simulation of this experiment was performed using one-quarter geometry 3D mesh (see Figure 3.13b) symmetry boundary conditions. Hexaedral 20-noded quadratic elements were used in the notch root region and the specimen half-thickness was divided into 10 elements. The load was applied *via* a rigid cylindrically-adapted meshed pin. The loading conditions are given in Table 3.1.

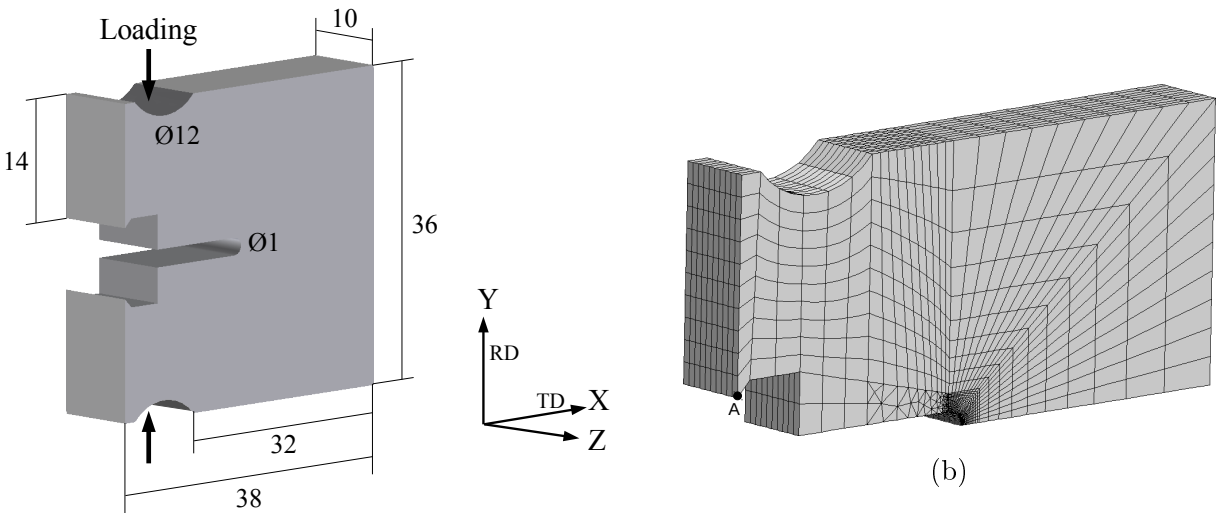

Figure 3.13: (a) CT-like specimen geometry. and corresponding (b) one quarter 3D FE mesh.

Table 3.1: FE simulation loading conditions, θ=550, 575 or 600°C.

Time	0 s	50 s	100 s	1 h	6 months
Temperature [°C]	20	20	20	θ	θ
Load [kN]	0	25	0	0	0

3.5.1 Simulation results

Figure 3.14 shows the comparison between the experimental data and the numerical prediction of the CT-like specimen force/displacement responses during compression and unloading at 20°C. The displacement was measured at node A (see Figure 3.13b). The different experimental curves correspond to the response of five tested CT-like specimen with identical geometry. These results shows the ability of the constitutive model to predicting the global response of the CT-specimen during such loading. An error of $\sim$ 20% can however be observed in the final CT specimen mouth displacement value. It is attributed to the higher flow stress predicted by the constitutive model in tension after a compression stage than the one measured experimentally (see Figure 3.11).

Figure 3.15 shows the predicted residual stress field of interest, σ_{22}, upon unloading at 20°C (t=100 s, see Table 3.1), in the notch root region of the CT-like specimen. The predicted maximal residual stress magnitude is 930 MPa at about 300 μm from the notch root. These results are consistent with the corresponding σ_{22} residual stress distribution found by Sherry et al. (2002); Turski et al. (2008) in the notch root regions of CT-like specimens after pre-compression. Figure 3.16 shows the numerical predictions of this residual stress field relaxation at 550, 575 and 600°C (t>100 s) as a function of the distance from de notch root along the X-direction, at mid-thickness. During the first 120 hrs of stress relaxation, approximately 30-40% of the initial residual stress magnitude relaxes. Less substantive changes are predicted thereafter. Furthermore, peak residual stress moves towards the X-direction to be maximum at about 1200 μm

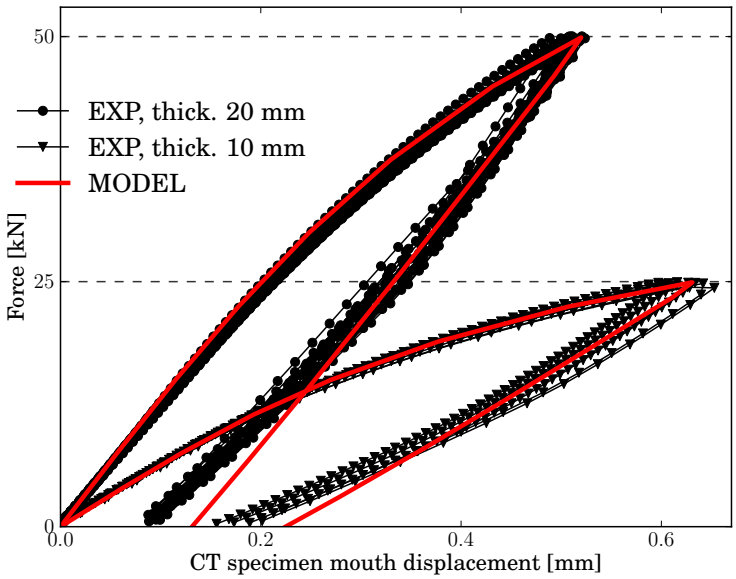

Figure 3.14: Measured and predicted force/displacement responses of the CT-like specimens during loading at 20°C.

from the notch root after 4320 hrs. Such predictions are consistent with the residual stress distribution evolution observed by Turski et al. (2008) for similar conditions. During the residual stress relaxation, the distribution of the σ_{22} residual stress field was found to develop two local maxima (see Figure 3.16). This numerically predicted phenomenon can be explained by the initial internal stress distributions in the notch root region of the CT-like specimen and may also involve residual stress redistribution in the whole specimen during relaxation to maintain the mechanical equilibrium (see Figure 3.17). Further experimental measurements of such residual stress field evolution is required to confirm the existence of this predicted phenomenon.

3.6 Conclusions

A rate-dependent constitutive model based on evolving microstructural length scales has been developed for austenitic stainless steels. The material behavior was associated to microstructure-related length scales, *viz.* the dislocation spacing and the deformation twin spacing. The formulation provides a constitutive framework suitable to other low stacking fault energy FCC materials to predict the development of residual stress fields by inelastic deformation and the subsequent relaxation of these fields when thermally exposed at high temperatures. The formulation relies on a single rate-dependent flow rule to describe the material quasi-rate-independent behavior at room temperature and rate-dependent behaviour at typical service temperatures (500-600°C). The constitutive model was formulated within a continuum mechanics framework for large strains and was explicitly implemented into a finite element method and the constitutive parameters were calibrated for an AISI 316L austenitic stainless steel. In the 20-600°C temperature range, a good agreement between the model responses and the experimental data which included monotonic tensile tests, stress reversal tests (showing Baushinger effect), stress relaxation tests and microstructural measurements, was found. To take account deformation twinning enabled the material hardening behavior in the 20-600°C temperature range to be reproduced

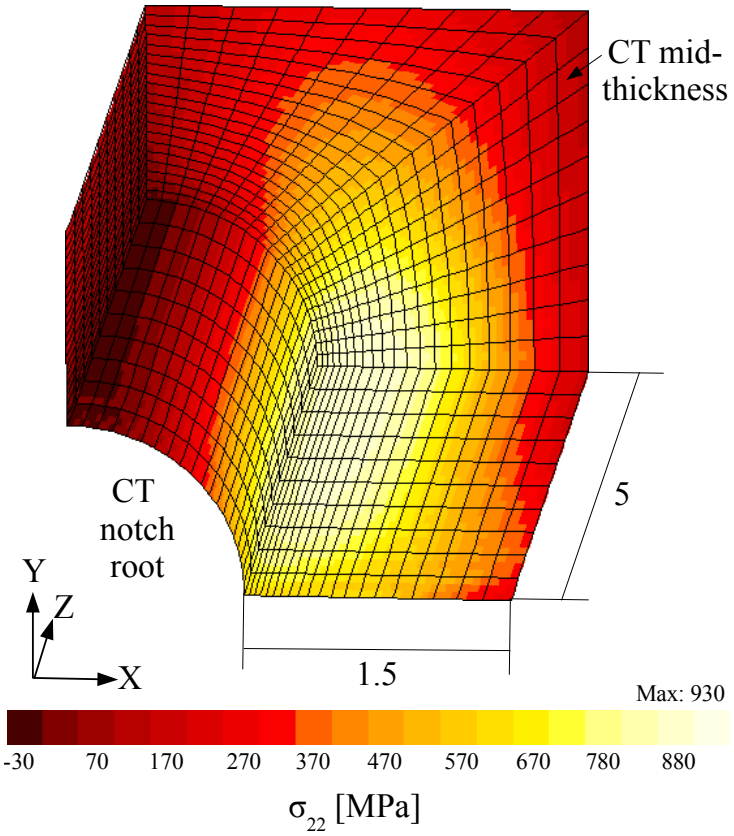

Figure 3.15: σ_{22} residual stresses in the notch root region of the CT-like specimens before thermal exposure (t=100 s, see Table 3.1).

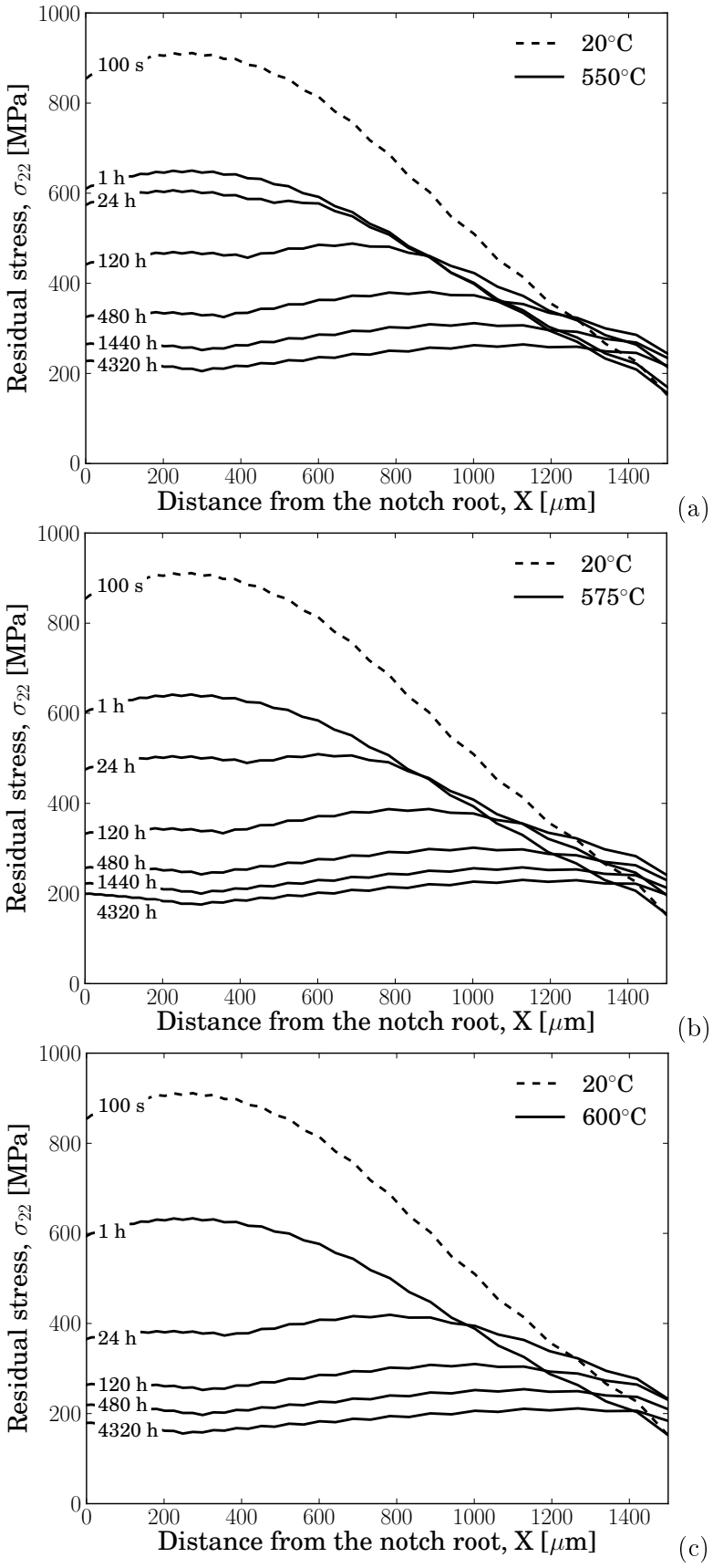

Figure 3.16: σ_{22} residual stress field in the notch root region of the CT-like specimen as a function of the relaxation time at (a) 550, (b) 575 and (c) 600°C.

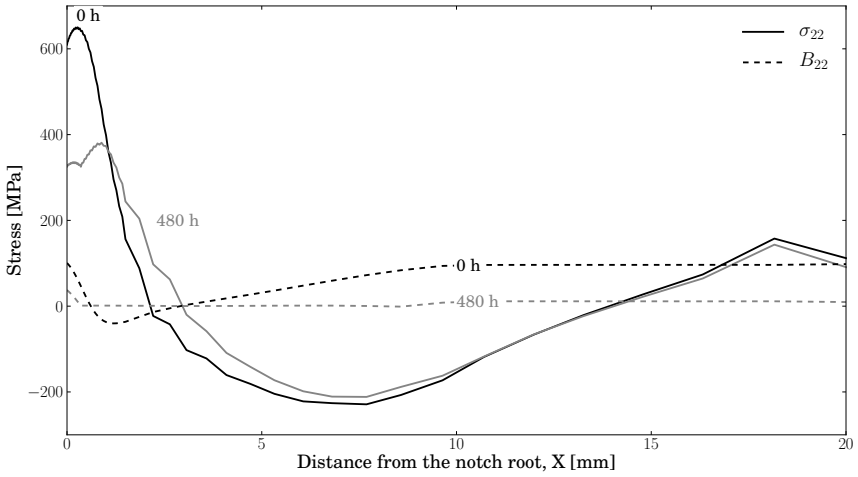

Figure 3.17: Prediction of the σ_{22} residual stress and the B_{22} internal stress during stress relaxation at 550°C as a function of relaxation time.

with a single set of temperature-independent parameters. Furthermore, the thermally-activated static recovery of the dislocation density enabled the stress relaxation kinetics to be predicted at high temperatures. The accurate prediction of the material behavior after cold rolling was found possible by initialising the initial internal variables. Finally, the constitutive model was applied to predict the residual stress relaxation in a CT-like specimen used to study stress relaxation cracking. The residual stress field distributions and their evolutions were found consistent with results from the literature. This constitutive model can be useful to assess the level of residual stress that led to stress relaxation cracking in specimens or components.

CHAPTER 4

Local damage approach to stress relaxation cracking

Résumé

Ce chapitre concerne la mesure expérimentale et la prédiction numérique des distributions d'endommagment intergranulaire dans les éprouvettes CT. L'endommagement majoritairement constitué de microfissures intergranulaires, a été calculé à partir des données issues de la tomographie X de synchrotron. Cette technique permet de visualiser les distributions d'endommagement en 3D dans les éprouvettes et d'obtenir une distribution statistiquement plus représentative que sur une coupe 2D du matériau. Ainsi, la meilleure connaissance des distributions d'endommagement en fond d'entaille a permis de déduire les conditions thermomécaniques permettant la FER en les comparant avec les prédictions numériques des champs de contraintes résiduelles. Ensuite, l'évolution d'une variable d'endommagement scalaire liée à l'évolution des déformations et des contraintes résiduelles dans les éprouvettes est calibrée sur les distributions expérimentales d'endommagement. Ce modèle d'endommagement constitue un outil utile pour prédire la FER dans des structures en aciers de type 316L.

This chapter is concerned with the intergranular damage quantification in the notch root regions of the tested CT-like specimens using synchrotron X-ray tomography and the numerical prediction of this damage following local approach to fracture. A damage law is proposed and calibrated to reproduce the experimental damage distributions in the CT specimens. The residual stress and strain field predictions in this chapter were obtained from the viscoplastic constitutive model presented in chapter 3. This chapter is structured for a possible publication.

Abstract

This study deals with the experimental quantification and the numerical prediction of the intergranular damage which develops during residual stress relaxation in the notch root region of AISI 316L-type CT-like specimens tested at 550, 575 and 600°C. Here, the damage, consisting of cracked grain boundaries, was measured using synchrotron X-ray tomography and the residual strain and stress field evolutions in the damaged regions were predicted by finite element calculations. Finally, a continuum damage model using a scalar damage variable was calibrated to

reproduce the experimentally measured damage distributions the specimens. The numerical predictions were found to be consistent with the measured damage distributions. It is also shown that the damage model can also provide a useful estimation of the propensity to relaxation cracking in highly pre-strained AISI 316L-type steels.

Contents

4.1 Introduction

During high temperature service, AISI 316L-type austenitic stainless steels can be prone to intergranular cracking near welded joints. This phenomenon, known as stress relaxation cracking or reheat cracking (RC), is driven by the relaxation of residual stress fields initially introduced during the welding process due to thermal strain incompatibilities. The prediction of such damage development is crucial to ensure the durability of welded components operating at high temperatures.

Intergranular fracture at high temperatures has been largely investigated in austenitic stainless steels, particularly at Centre des Matériaux (Argence and Pineau, 1995; Auzoux et al., 2005; Levaillant, 1984; Weiss, 1992; Yoshida, 1985). Typically, approaches to predict high temperature intergranular fracture rely on local damage models using the local approach to fracture (e.g. (Yoshida et al., 1987)). Some proposed damage models (e.g. (Auzoux et al., 2005; Michel, 2004; Skelton et al., 2003; Spindler, 2004a, 2007)) incorporate the reduced ductility observed under multiaxial creep conditions. Other damage models (e.g. (Auzoux et al., 2005)) addressed the effect of pre-strain, which is known to decrease the creep strain rate and the creep strain at failure (Moen and Smith, 1975; Willis et al., 1999; Wilshire and Willis, 2004). However, there has been very limited work which considered the predictive capability of such phenomenological damage models, under residual stress relaxation conditions, when the temperature and/or the initial residual stress magnitude evolve. It is known that temperature affects residual stress relaxation kinetics. However, it is unclear whether the different residual stress relaxation kinetics can explain the different levels of intergranular damage that can be found after residual stress relaxation at high temperatures. This work addresses those limitations by investigating the responses of a high temperature intergranular damage model, simply inspired from the damage kinetics initially introduced by Yoshida et al. (1987), when evaluated under stress relaxation conditions at different temperatures.

Particular emphasis is placed in the prediction of stress relaxation cracking damage de-

velopment in an AISI 316L-type austenitic stainless steel which was previously tested using pre-compressed CT-like specimens (see chapter 2). To that purpose, the level of intergranular damage present in the notch root of CT-like specimens tested under residual stress relaxation conditions at 550, 575 and 600°C for 3620 h is first measured using X-ray synchrotron tomography and 3D image analysis. Then, the residual strain and stress field predictions in the notch root region of the tested CT-like specimens are presented. Finally, the distribution of the measured local intergranular damage was modelled numerically by linking, in a sequential manner, an evolutionary relation for a scalar damage variable with the predicted stress and strain fields.

4.2 Materials and experimental methodology

4.2.1 Materials and specimens

This work is a follow-up of that reported in chapter 2 in which AISI 316L-type austenitic stainless steels were tested under stress relaxation conditions using CT-like specimens. This experiment involved the introduction of high tensile residual stress fields in the notch root regions of CT specimens at room temperature by a compression technique. Then, the CT specimens were exposed at temperatures of 550, 575 and 600°C for 3620 h. After thermal exposure, intergranular damage was observed in the specimen high tensile residual stress regions by optical microscopy and SEM. Intergranular microcavities were found to have developed at grain boundaries (GBs) containing $M_{23}C_6$ carbides which preferentially precipitated, during thermal exposure, on highly misoriented grain boundaries (GBs) (25 to 55^o) normal to the maximum principal residual stress directions. In the most highly damaged specimens, the microcavities were found to have coalesced into grain-sized microcracks (GB facets). In this work, five CT specimens are to be considered: three CT specimens with the same notch radius (1 mm) and tested at 550, 575 and 600°C for 3620 h and two others with notch radii of 0.5 and 2 mm, both tested at 575°C for 3620 h.

The CT specimens were obtained from of a 19% cold rolled AISI 316L-type austenitic stainless steel sheet containing 0.028 wt.% carbon and 0.077 wt.% nitrogen. The microstructure was composed of equiaxed austenitic grains containing annealing and deformation twins ($\sim$ 11% volume fraction), and showed no crystallographic texture. The mean grain size was 40$\pm$23 μm and the material hardness measured on residual stress-free regions before thermal exposure was 276 HV_{30}.

4.2.2 Damage measurement

In order to quantify the intergranular damage, tensile specimens containing the notch root regions of the CT-like specimens (at mid-thickness) were machined by EDM after residual stress relaxation at high temperature. Then, the tensile specimens were deformed *in situ* and scanned using synchrotron X-ray tomography at the European Synchrotron Radiation Facility (ESRF, beamline ID15a) in Grenoble (further information about synchrotron tomography and *in situ* tensile tests can be found in (Kahziz, 2016; Landron, 2012)). The tensile deformation was carried out to open up any existing microcavities and microcracks by plastic deformation. When the size of a defect exceeded the tomography voxel size (i.e. for this experiment, 1.095 μm), the defect could be detected. From experimental observations, it was concluded that the damage observed in the *in situ* tomography studies could only have evolved from GB crack-like defects

which could already be identified by SEM after the residual stress relaxation tests (see chapter 2 for further information about this procedure). The studied volumes were deformed by 20±3% (true plastic strain) in a direction normal to the damaged GBs. To identify the original microcrack positions in the CT specimens, the scanned volumes were resized using bilinear voxel interpolation to the theoretical dimensions they had before they were plastically deformed. A typical slice exhibiting the notch root region of a CT-like specimen tested at 575°C for 3620 h and *in situ* scanned by synchrotron X-ray tomography is shown in Figure 4.1. In this figure, the microcracks appear darker than the matrix. Some ring-shaped artefact can also be observed. They are inherent to the tomography technique and were removed thereafter in the complete 3D reconstructions.

A typical rendered 1000x1300x500 μm^3 notch root region exhibiting microcracks is shown

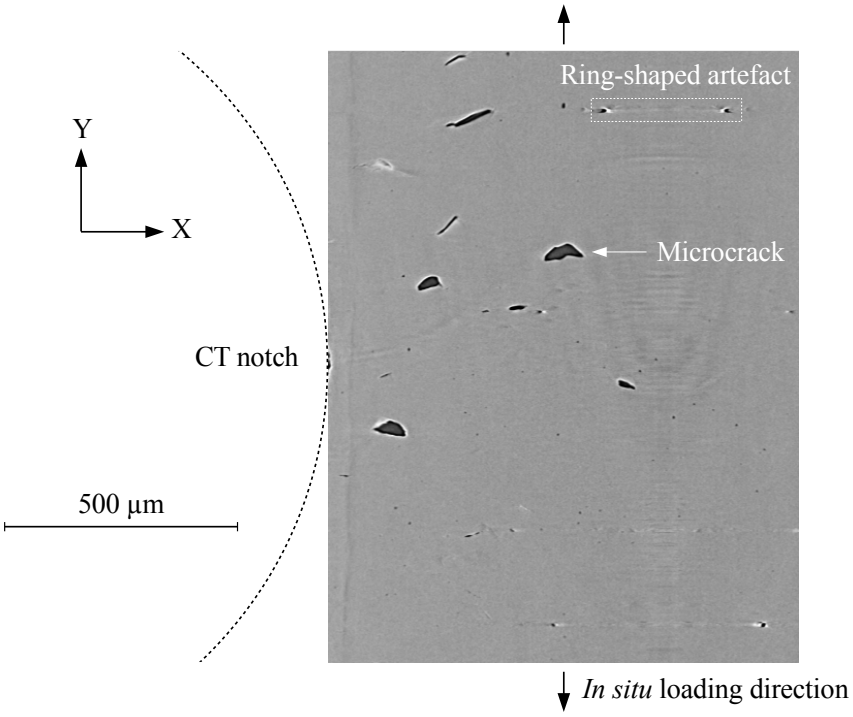

Figure 4.1: Notch root region of a CT-like specimen tested at 575°C for 3620 h and *in situ* scanned by synchrotron X-ray tomography.

in Figure 4.2(a). Here, the CT notch root *loci* are represented with the red dashed line, the CT loading direction was along the Y-axis. In Figure 4.2(b), the intergranular microcracks contained in the volume were rendered in 3D by thresholding the grayscale data. The additional homogeneous distribution of small particles that also appear coloured in red in this figure were identified as MnS inclusions. They were not removed from the rendered data since they were not found to alter the damage quantification performed thereafter. The total analysed volume was discretised into 20x26x10 50 μm cubes . Then, a local damage variable, D, was defined in each cube by the ratio of the microcracks projected area in the Y-direction, S, over the area of a cube face (see Figure 4.2(c)). The position of each cube in the specimen notch root region can be represented by three indices (i,j,k) corresponding to its position in the X, Y and Z-directions,

respectively (see Figure 4.2(d)). Thus, the damage in the cube (i,j,k), can be written as,

$$D^{(ijk)} = \frac{S^{(ijk)}}{a^2} \tag{4.1}$$

where, a is the cube unit length.

Since the grain size (40±23 μm) was close to the cube size (50 μm), a grain size microcrack ($\sim$ GB facet) can be assumed to be present in a cube when D=1. Figure 4.2(d) shows an example of the experimental damage calculation results in 3D.

In order to facilitate the damage distribution visualisations in the specimen notch root regions, the damage, D, can be averaged in the Z-direction to obtain a 2D damage variable, called here mean planar damage, $\overline{D}$. The objective of defining this mean planar damage variable is to enable a better statistical significance of the damage distribution since all microcracks present through the scanned volume thickness (Z-direction) are taken into account. It should be noted that averaging the damage values through the volume thickness (Z-direction) is physically consistent since the residual strain and stress fields predicted by finite element were not found to evolve significantly along that direction in the CT specimen mid-thickness. This mean planar damage can be defined as,

$$\overline{D}_{ij} = \frac{1}{10}\sum_{k=1}^{10} D^{(ijk)} \tag{4.2}$$

Finally, in order to facilitate the damage distribution visualisations along the X-direction from the specimen notch root, the damage, $\overline{D}$, can be averaged in the Y-direction to obtain a 1D damage variable, denoted as the mean linear damage, $\overline{\overline{D}}$. This damage variable was built to enable a better visualisation of the damage distribution along the X-direction from the notch root. However, since the damage was found to be inhomogeneously distributed along the Y-direction, the values of $\overline{\overline{D}}$ are lower than those of $\overline{D}$ along the X-direction from the notch root. Therefore, the values of the mean linear damage, $\overline{\overline{D}}$, must be multiplied by a fitting constant, ϕ, so that they correspond approximately to the mean planar damage values of interest. It gives,

$$\overline{\overline{D}}_i = \frac{\phi}{26}\sum_{j=1}^{26} \overline{D}^{(ij)} \tag{4.3}$$

4.3 Numerical predictions

4.3.1 Residual strain and stress field predictions

Finite element simulations were carried out using the commercial Z-set software (Zset, 2015) to predict the residual stress and strain field evolutions in the notch root regions of the CT-like specimens. The constitutive model used to describe the mechanical behaviour of the 316L-type steel has been described elsewhere (see chapter 3). It was implemented into the Z-set code as a user-defined material subroutine. The material parameters, the specimen mesh and the finite element simulation parameters can be found in chapter 3.

The predictions of the stress field evolutions in the notch root region of the five CT-like specimens are shown in Figure 4.3. In all specimens, the initial maximum principal residual stress was found to be close to the notch root surface ($\sim$300 μm in the X-direction) while the

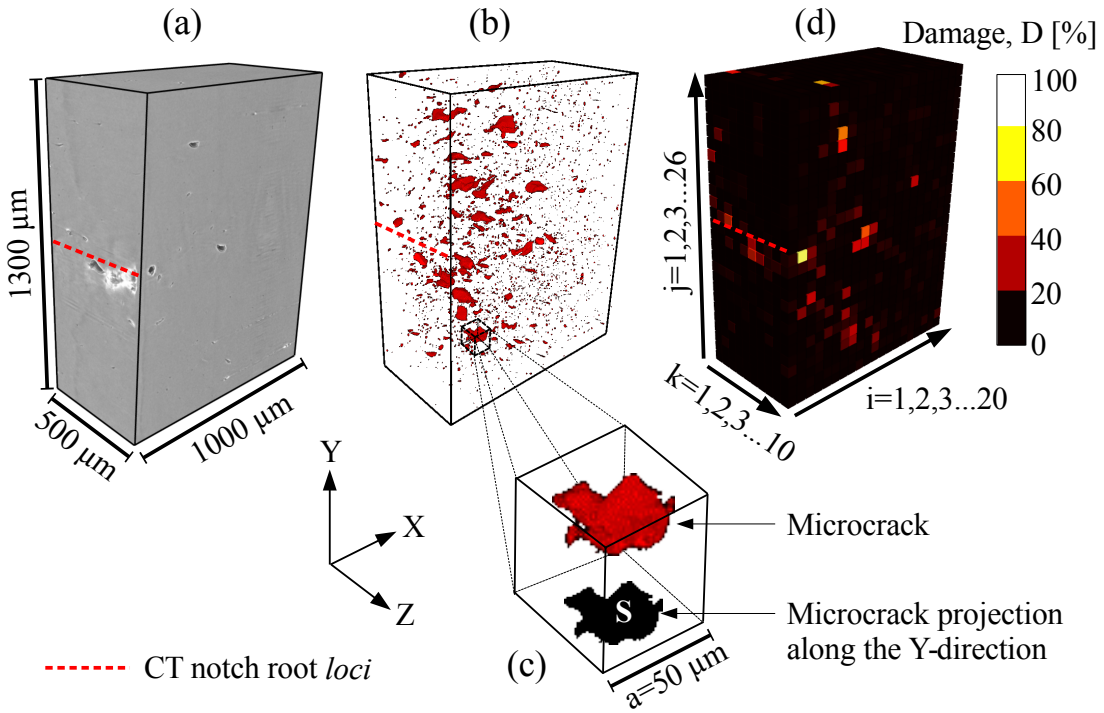

Figure 4.2: Damage quantification method from X-ray synchrotron tomography data in the notch root region of the CT-like specimen tested at 575°C for 3620 h: (a) gray-scale rendered volume, (b) binarised volume showing the microcracks, (c) schematic illustration of the damage projection and (d) damage calculation results according to Eq. 1.

initial equivalent plastic strain is maximum at the notch root surface (see dashed-curves). Furthermore, the maximum principal residual stress levels were predicted to increase with decreasing specimen notch radius. When considering the stress relaxation kinetics, it can be observed that approximately 30-40% of the initial residual stress magnitude relaxes during the first 360 hs of thermal exposure and that the residual stress hardly relaxes afterwards. Such predictions are consistent with the stress relaxation kinetics observed by (Turski et al., 2008) in a AISI 316H austenitic stainless steel.

4.3.2 Damage model

The damage model to be used in this work is inspired from the damage evolutionary relation initially introduced by (Yoshida et al., 1987) which was applied to describe creep (Piques, 1989; Poquillon, 1997; Reytier, 1999; Yoshida, 1985) and creep-fatigue (Argence and Pineau, 1995; Levaillant, 1984; Weiss, 1992) damage development in austenitic stainless steels. The formulation enables the assessment of the intergranular damage evolution, $\dot{D}^*$, as a function of the principal stress, σ_I and the equivalent viscoplastic strain rate, $\dot{\bar{\epsilon}}^p$:

$$\dot{D}^* = \alpha \langle \sigma_I \rangle^\beta \dot{\bar{\epsilon}}^p \tag{4.4}$$

where, α and β are material-dependant parameters and the notation $\langle\ \rangle$ corresponds to the Macauley brackets: $\langle x \rangle = x$ if $x > 0$ and is 0 elsewhere. Thus, this formulation enables damage development only under tensile loading.

It should be noted that Equation 4.4 does not take into account explicitly the level of pre-strain. This point was motivated by the fact that pre-straining is known to reduce creep ductility in austenitic stainless steels. However, for high pre-strain levels (> 0.2 equivalent plastic strain), the creep ductility is known to remain stable at a minimum value in AISI 316-type austenitic stainless steels (Willis et al., 1999). In the notch root regions of the specimens of interest, the equivalent plastic strains were predicted to be higher than 0.24 (see Figure 4.3). Thus, the pre-strain effect on intergranular damage development was assumed to be approximately the same in the whole specimen notch root regions, whatever the different equivalent plastic strain values. Furthermore, the maximum principal residual stress was assumed to be the best mechanical driving force to describe intergranular damage development under stress relaxation conditions from the results of chapter 2.

The damage model was linked to the finite element stress and strain field predictions as post-processing routine using Python. The damage rate was integrated using the explicit Euler method at each time increment during the stress relaxation. The damage model parameter identification was performed by correlating the experimental damage distributions measured by synchrotron X-ray tomography to the numerical ones.

4.4 Results and discussion

4.4.1 Intergranular damage measurements

The results of the intergranular damage measurement are presented in Figure 4.4, in the form of the mean planar damage (Eq. 4.2) and in Figure 4.5 as the mean linear damage (Eq. 4.3)

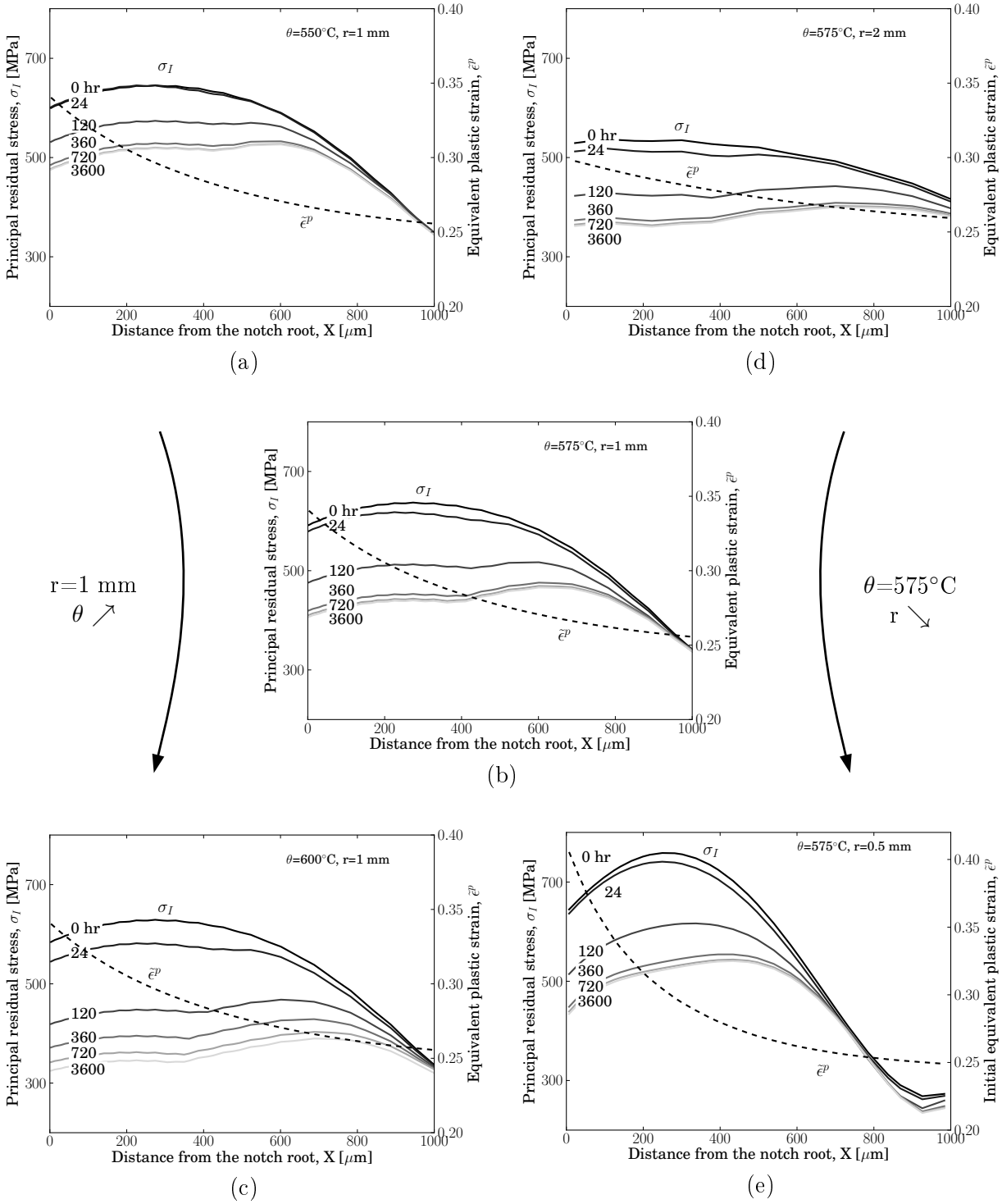

Figure 4.3: Prediction of the principal residual stress relaxations in the CT specimens with a notch root radius, r=1 mm tested at (a) 550, (b) 575 and (c) 600°C for 3600 hrs and in CT specimens with notch root radii of (d) 2 mm and (e) 0.5 mm tested at 575°C for 3600 h. The initial equivalent plastic strain is represented by the dashed-curves.

in the same specimens. The values of ϕ used to fit $\overline{\overline{D}}$ (Eq. 4.3) are given in Table 4.1. When comparing the experimental damage calculation results in Figure 4.4 and 4.5, one can observe the consistency of the two damage parameters, $\overline{D}$ and $\overline{\overline{D}}$, along the X-direction from the notch root. In all specimens except the one with a notch radius of 0.5 mm (Figure 4.5(e)), the microcracks were uncontinuously distributed in the notch root regions of the specimens and the *loci* of maximum damage were close to ∼300 μm from the notch root, as were the predicted *loci* of the initial maximum principal residual stresses (see Figure 4.3).

The specimen with a notch root of 0.5 mm (Figure 4.5(e)), exhibited a ∼750 μm long crack in the X-direction and presented the highest level of intergranular damage compared with those with notch radii of 1 and 2 mm tested in the same conditions (Figure 4.5(b) and (d), respectively). Furthermore, the effect of testing temperatures can be observed when considering the specimens with a notch radius of 1 mm which were tested at 550, 575 and 600°C (Figure 4.5(a)). In these specimens, the highest level of intergranular damage was observed in the one tested at 575°Cl, followed by the one tested at 550°C and then the one tested at 600°Cl.

Table 4.1: Testing time and temperature, CT notch root radius and ϕ parameters of the five tested specimens.

Specimen No.	①	②	③	④	⑤
Testing temperature, θ [K]	600	575	550	575	575
Test duration, t [h]	3620	3620	3620	3620	3620
Notch root radius, r [mm]	1	1	1	0.5	2
Value of ϕ (see Eq. 4.3)	5	5	5	14	10

4.4.2 Damage modelling

Figure 4.6(a) corresponds to the damage model predictions in the specimens with the notch radii of 0.5, 1 and 2 mm tested at 575°C (Specimens No. 4, 2 and 5, respectively) with $\alpha = 1.4 \times 10^{-15}$ MPa^{-6} and $\beta = 6$. A good agreement is observed between the experimental and the numerical damage distributions which shows the damage model ability to describe the different levels of intergranular damage associated to different levels of initial residual stresses. With the performed calibration, the predicted damage level which corresponds to the formation of a macrocrack (between the green and the blue curves) can be estimate to be in the 0.25-0.5 damage range. Furthermore, the numerical damage level which corresponds to the onset of the experimental damage detection is approximately 0.05.

Figure 4.6(b) shows the damage model predictions in the specimens with a notch radius of 1 mm and tested at 600, 575 and 550°C (specimens No. 1, 2 and 3, respectively) with α and β having the same values as previously calibrated at 575°C. Here, the damage model shows poor predictive capabilities when the temperature changes. Therefore, the different residual stress relaxation kinetics in the specimens (see Figure 4.3) are not sufficient to accurately describe the different levels of intergranular damage found at different temperatures. This result indicates that the α parameter in Eq.4.4 must be strongly temperature dependent and potentially associated to diffusion-related mechanisms.

Figure 4.6(c) corresponds to the damage model responses with α calibrated for each temperature: $\alpha = 1.6 \times 10^{-16}$, 1.4×10^{-15} and 6.2×10^{-16} MPa^{-6} at 600, 575 and 550°C, respectively. A good agreement is observed between the experimental and the numerical damage distributions in this case. It can be inferred from the damage measurements in the specimens with a notch

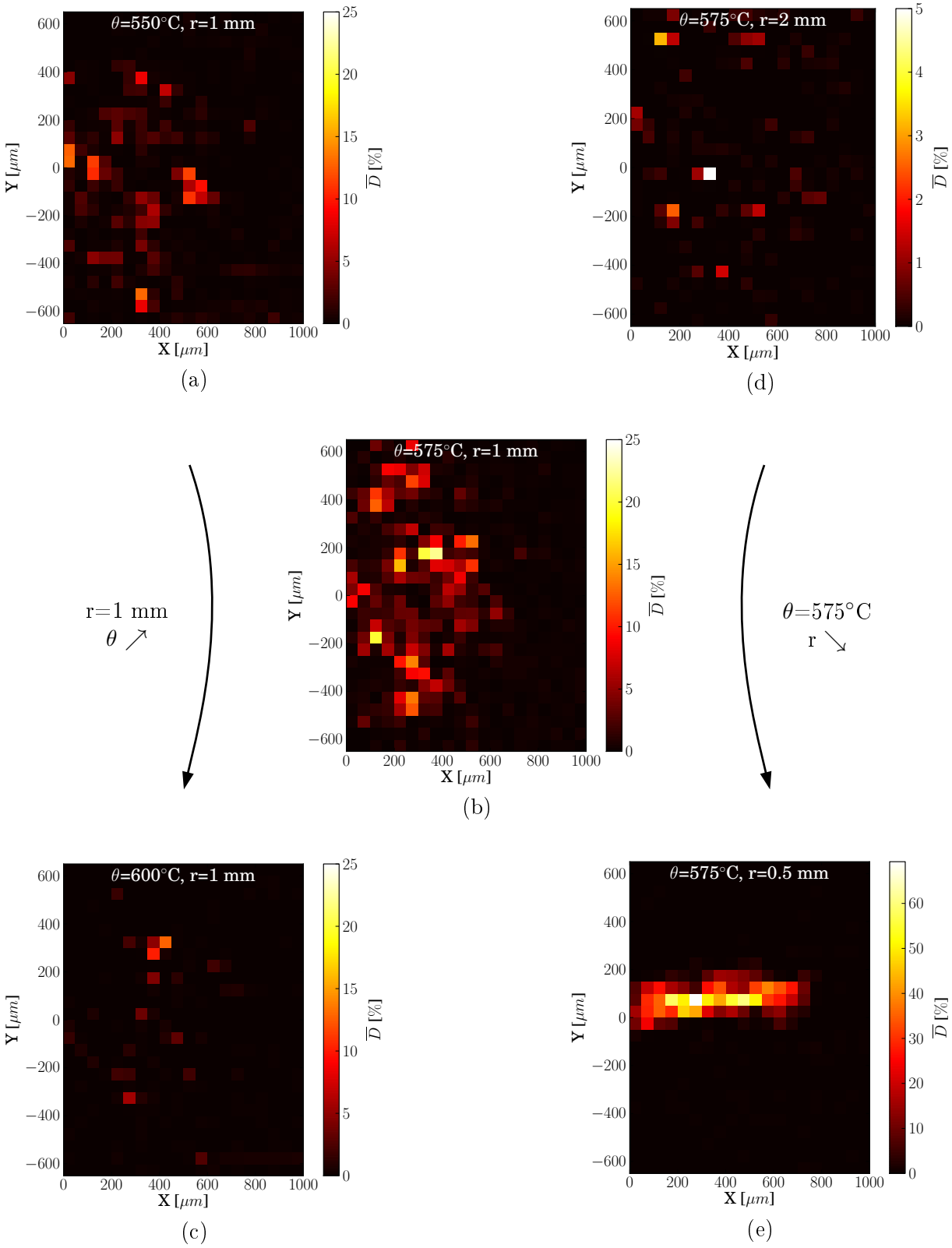

Figure 4.4: Mean planar damage, $\overline{D}$, in the notch root regions of the CT specimens with a notch root radius, r=1 mm tested at (a) 550, (b) 575 and (c) 600°C for 3620 h and in the CT specimens with notch root radii of (d) 2 mm and (e) 0.5 mm tested at 575°C for 3620 h.

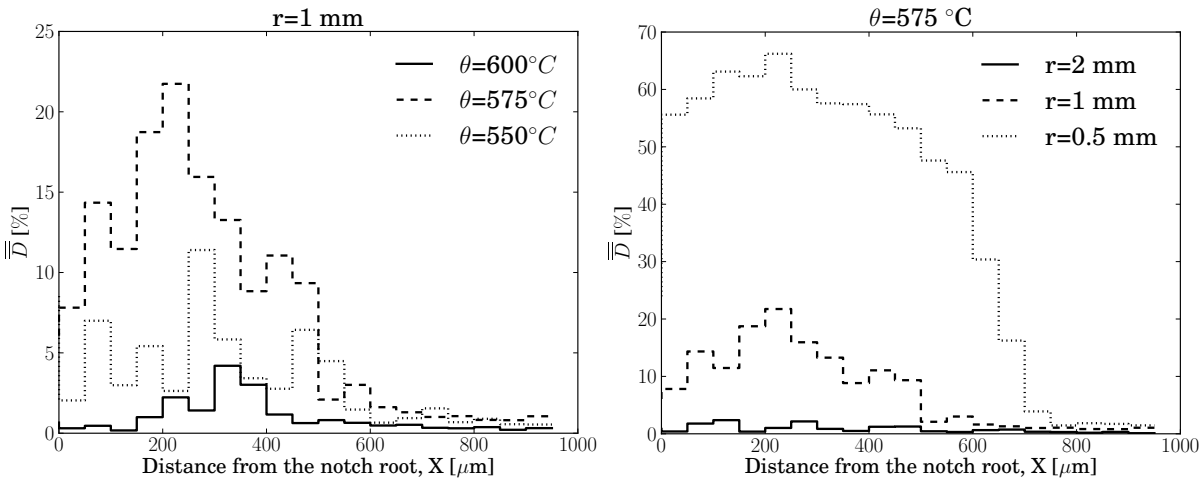

Figure 4.5: Mean linear damage, $\overline{\overline{D}}$, along the X-direction in the CT specimens (a) tested at 550, 575 and 600°C for 3620 h and (b) in the CT specimens with notch radii of 0.5, 1 and 2 mm tested at 575°C for 3620 h.

radius of 1 mm and tested at 550, 575 and 600°C that a critical temperature between 550 and 600°C for stress relaxation cracking likely exists in the AISI 316L-type steel of interest. The prediction of stress relaxation damage for temperatures close to the tested ones can be estimated by extrapolating the α parameter values (Eq. 1) which were calibrated at 550, 575 and 600°C (see Figure 4.6). For this purpose, a quadratic interpolation of the α^{-1} values as a function of the temperature is proposed to avoid negative values of α when extrapolated outside the 550-600°C temperature range. The result is shown in Figure 4.7(a). The corresponding values of α are shown in a logarithmic representation in Figure 4.7(b). With such interpolation function, the critical temperature which should induce the most stress relaxation cracking was found to be 565°C. However, these results are highly dependent on the interpolation function and would require further experimental data to be confirmed.

The temperature effect on the measured intergranular damage levels was reproduced in this work by calibrating the damage model at each tested temperature. However, a comprehensive understanding of the mechanisms responsible for such non-linear temperature effect on reheat cracking damage development is still lacking. This problem may involve thermally-activated GB degradation by carbide precipitation and intergranular segregation which also depend on GB normal stress and pre-strain levels.

It should be noted that the damage model used here does not take into account the stress and strain fields at the grain scale. A more accurate prediction of the microcrack distributions in the specimen could be attempted following the work by Diard et al. (2002) in which they meshed representative microstructures and applied a crystal plasticity model in order to evaluate the local intergranular heterogeneity of the stress and strain fields. Then, an intergranular damage model was applied at the grain scale to assess the damage localisation. Such method should enable a better description of the intergranular damage development on specific GBs and also enable an implicit description of the pre-strain effect on GB stress localisation.

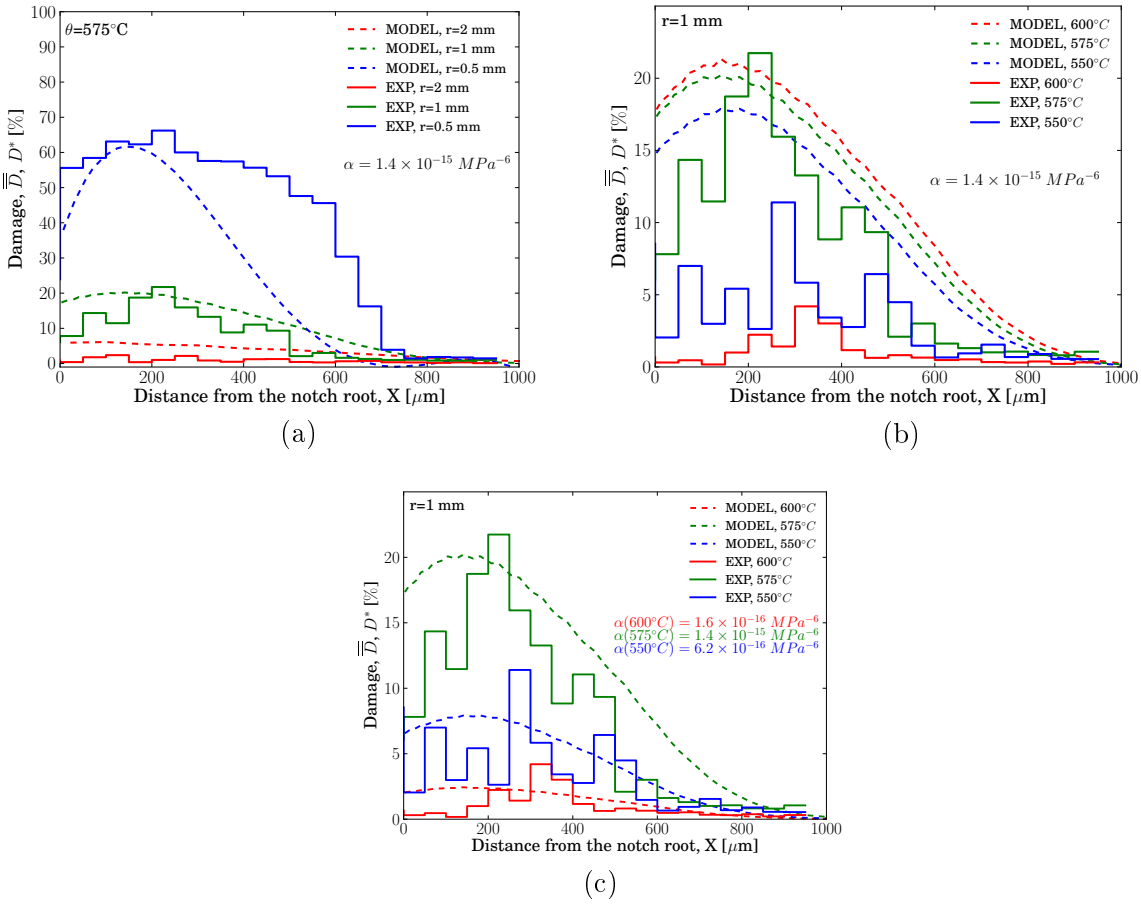

Figure 4.6: Comparison between the experimental mean linear damage and the numerical predictions of the damage model in the CT-like specimens (a) No. 2, 4 and 5 with α being temperature independent, (b) No. 1, 2 and 3, with α being temperature independent and (c) No. 1, 2 and 3, with α being temperature dependent.

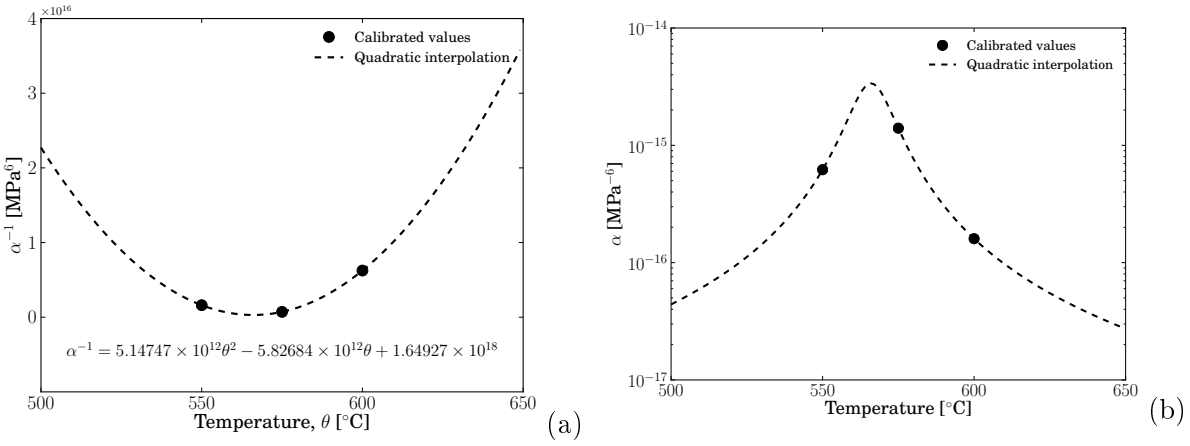

Figure 4.7: (a) Quadratic interpolation of the α^{-1} values as a function of temperature and (b) corresponding values of α in a logarithmic representation.

4.5 Conclusions

In a AISI 316L-type austenitic stainless steel, the intergranular damage distributions in the notch root region of CT-like specimens tested under reheat cracking conditions have been measured using synchrotron X-ray tomography and 3D image analysis. A simple damage model based on a scalar damage variable has been proposed to model stress relaxation cracking in the tested AISI 316L-type austenitic stainless steel. The damage model was calibrated in the 550-600°C temperature range for high levels of pre-strain (>0.2 equivalent plastic strain). The numerical damage variable value can be relied upon to assess the nature of the predicted intergranular damage: from 0 to ∼0.05, no intergranular damage is expected, from ∼0.05 to ∼0.25-0.5, microcracks are expected and finally, above ∼0.25-0.5, macrocracks can develop in the material. It also has been shown that using the maximum principal residual stress evolution as a driving force for intergranular damage development enables a good reproduction of the measured damage distributions whatever the tested initial residual stress magnitude or the tested temperatures. The calibrated damage model may also provide a useful estimation of the relaxation cracking propensity of AISI 316L-type steels at temperatures and residual stress levels outside the range in this work.

CHAPTER 5

Conclusions and prospects for future work

Résumé

Les objectifs ce travail étaient (i) d'identifier les caractéristiques, ainsi que les forces motrices, responsables de la FER dans les aciers de type AISI 316L, (ii) d'améliorer lacompréhension du rôle des éléments d'alliage (en particulier C, N et P) et des conditions thermomécaniques nécessaires au développement de la FER et (iii) de développer un cadre numérique, basé sur des observations et des mesures expérimentales, permettant de décrire et de prédire la FER dans ces aciers. Les principales conclusions de cette thèse peuvent se résumer comme suit. (i) Pour la première fois, il a été montré que le développement d'endommagement intergranulaire était possible par relaxation de contraintes résiduelles dans les aciers de type 316L. (ii) L'étude des mécanismes de FER dans les aciers de type 316L a montré que la précipitation des carbures $M_{23}C_6$ associée à des contraintes résiduelles élevées (nécessitant une pré-déformation plastique importante, voir Auzoux (2004)) qui se relaxent lentement favorise la FER de ces aciers. (iii) Les niveaux d'endommagement de FER sont très dépendants de la composition chimique des aciers, notamment de leur teneur en C, N et P. La comparaison entre les niveaux d'endommagement mesurés dans cinq aciers, de teneurs en C, N et P différentes, a permis de déduire qu'une teneur en C $\sim$>0.025% favorise la FER et qu'une haute teneur en N $\sim$>0.06% devrait être ajoutée uniquement si la teneur en C est très basse $\sim$<0.015%. (iv) Une haute teneur en P ($\sim$520 ppm) dans un acier de type 316L a été testé en condition de FER mais n'a pas été aussi néfaste à la résistance des joints de grains qu'attendu. Ce résultat pourait être dû à un mécanisme de compétiton de site de ségrégation intergranulaire entre le P, N,C et/ou le B. (v) La comparaison entre les distributions expérimentales d'endommagement et les prédictions numériques des champs de contraintes résiduelles dans les éprouvettes a permis de déduire un niveau seuil de contrainte résiduelle principale, σ_I, de 740$\pm$40 MPa en dessous duquel la FER ne se développe pas dans les cinq aciers testés. (vi) L'analyse de l'effet de la température sur la FER a montré que la température intermédiaire de 575°C était plus endommageante que celles de 550 et 600°C. Il semble donc exister une température entre 550 et 600°C favorisant l'endommagement de FER pour un niveau de contraintes résiduelles donné. (vii) Finalement, l'évolution d'une variable d'endommagement scalaire liée à l'évolution des déformations et des contraintes résiduelles dans les éprouvettes a été calibrée sur les distributions expérimentales d'endommagement. Ainsi la loi d'endommagement obtenue est un outil numérique utile pour prédire la FER dans des structures en aciers de type 316L.

Contents

5.1 Results overview and conclusions

The aims of this work were (i) to identify the material and microstructural characteristics as well as the driving forces responsible for reheat cracking damage development in AISI 316L-type austenitic stainless steels, (ii) to gain an understanding about the role of alloying element and the thermo-mechanical conditions on the mechanisms of reheat cracking in AISI 316L-type austenitic stainless steels, and (iii) to develop a physics-inspired constitutive material modelling framework based on the experimental observations and measurements to predict the reheat cracking damage development in AISI 316L-type austenitic stainless steels. To that purpose, five cold-rolled AISI 316L-type austenitic stainless steels have been tested under residual stress relaxation conditions using pre-compressed CT-like specimens. Experimental damage observations and measurements have been carried out and a viscoplastic constitutive model has been developed to predict by finite element simulations the residual stress evolutions in the specimens. Finally, an evolutionary law for a scalar damage variable was calibrated to predict RC damage development in AISI 316L-type austenitic stainless steels. The main findings of this doctoral research can be summarised as follows.

For the first time, intergranular damage has been evidenced in AISI 316L-type austenitic stainless steels from residual stress field relaxations. The method chosen, using pre-compressed CT-like specimen, enabled the mechanical conditions necessary for RC damage development in some of the tested steels to be reproduced. Some of the studied alloys were not found to be sensitive to RC under the tested conditions. The results of this research revealed that AISI 316L-type austenitic stainless steels can exhibit drastically different RC resistances despite close chemical compositions, microstructure and room temperature mechanical behaviour. These results are consistent with the different creep and creep-fatigue resistances observed in the past for similar steels (Argence and Pineau, 1995) and the different intergranular crack propagation resistance observed by Auzoux (2004) in other AISI 316L-type steels.

In AISI 316L-type austenitic stainless steels, RC damage was found to consist of microcavities that nucleate along GBs at $M_{23}C_6$ carbides, and subsequently coalesce into intergranular microcracks and finally macrocracks. A study of the microcrack sites in the microstructure showed that GBs normal to the maximum principal residual stress where the most prone sites to RC. Furthermore, among these, 25 to 55° misoriented GBs were found particularly affected whereas $\Sigma 3$ ones were not. A literature review showed that such damage distribution on specific GBs is consistent with the different GB degradation by (i) $M_{23}C_6$ carbide precipitation (Hong et al., 2001; Jones et al., 2008) and (ii) impurity segregation, such as P, (Herbig et al., 2015; Ogura et al., 1987) as a function of the GB type. The effect of a high P content ($\sim$ 520 ppm) on RC damage development in a AISI 316L-type steel was tested but was not found to particularly aggravate the levels of intergranular damage. This unexpected result was attributed to intergranular site-competing segregation mechanisms between P, N, C and/or B, which inhibit P segregation at GBs in austenitic stainless steels. Consequently, the major chemical driving force for RC damage development was identified as being $M_{23}C_6$ carbide precipitation.

The five tested steels exhibit similar mechanical behaviour at room temperature. However,

close to 575°C, their stress relaxation kinetics were found to be significantly different. From the literature, slow stress relaxation was attributed to high solid N solution contents (Mathew et al., 1991). Consequently, high N contents were assumed to enable high residual stresses at GBs to be maintained for longer durations and thus increase the number of microcavities. From those considerations, a comparison between the five steel resistances to RC and their chemical compositions enabled to infer threshold values for C and N contents to reduce RC propensity. It was found that a high C content (about >0.025%) is detrimental to the GB resistance, and that high N content (about >0.06%) should be added only if the C content of the steel is low (about <0.015%).

A novel aspect of this work has been the use of synchrotron X-ray tomography to quantify the level of intergranular damage present in the specimens. To that purpose, a dedicated *in situ* procedure was devised to enable intergranular damage to be detected by tomography with a resolution of ∼1 μm. It consists of machining tensile specimens containing the intergranular damaged region of interest. Then, the specimens are deformed *in situ* to open up any existing microcrack oriented perpendicularly to the applied load by plastic deformation. Subsequent 3D image analyses of the tomography scanned volumes enabled the level of intergranular damage present in the specimens to be calculated with a greater statistical significance than on polished 2D surfaces. The results of those experimental damage calculations showed that extensive damage developed in the CT specimens with smaller notch radii, and that the ones tested at 575°C exhibited more damage than those tested at 550 and 600°C, respectively. Further work is needed for a comprehensive understanding of such temperature dependence.

The numerical prediction of the local residual stress and strain fields in the specimens was obtained from FE calculations. To this purpose, a novel viscoplastic constitutive model was proposed capable of describing both the development of residual stresses in AISI 316L-type steels by inelastic deformation at room temperature and their subsequent relaxation at high temperatures. The formulation relies on a single rate-dependent flow rule to describe the material inelastic and rate-dependent behaviour ranging from ambient temperature up to typical service temperatures (∼500-600°C). The evolution of the material behaviour is described through internal state variables explicitly linked to intrinsic microstructural length scales, *viz.* the dislocation spacing and the deformation twin spacing. A comparison between the predicted residual stress fields in the CT-like specimens and the intergranular damage distributions measured by synchrotron X-ray tomography was carried out to infer the threshold level of local residual stresses associated with the initiation of stress relaxation microcracks. For the less resistant tested steel, a maximum principal residual stress threshold of 740 ± 30 MPa (at room temperature) was identified below which no intergranular damage was found after ∼3600 hrs in the 550-600°C temperature range. This threshold level can be relied upon to predict the RC occurrence in AISI 316L-type steels.

Finally, a simple damage model based on a scalar damage variable has been proposed and combined with above viscoplastic constitutive model in a sequential (*i.e.* post-processed) manner to provide simulated distributions of RC damage in the tested AISI 316L-type austenitic stainless steel. The damage model was calibrated in the 550-600°C temperature range for high levels of pre-strain. It has also been shown that using the maximum principal residual stress evolution as a driving force for intergranular damage development enables a good reproduction of the measured damage distributions whatever the tested initial residual stress magnitude or the tested temperatures. The calibrated damage model may also provide a useful estimation about the relaxation cracking propensity of AISI 316L-type steels at temperatures and residual stress levels outside the range investigated in this work.

5.2 Study limitations and perspectives

The study of RC was performed in this work by testing pre-compressed CT-like specimens machined from cold rolled materials. Real HAZ affected by RC have been found to undergo several thermal cycles during welding which typically induce inelastic deformation up to ∼10-20% cumulated plastic strain (Auzoux et al., 2010; Turski et al., 2008). Such pre-deformation history is not reproduced by the technique chosen in this work. Instead, ∼20% cold rolled materials were used to approximate the material deformation level mentioned above. Two major differences between these pre-deformation conditions can be highlighted. First, cold rolling induces the development of deformation twins which act as microstructural barriers. Even though the presence of those twins was not found to alter the intergranular damage mechanisms, they could potentially affect the macroscopic stress relaxation kinetics. Secondly, the internal stress levels found after cyclic or monotonic deformations are unlikely to be similar. It could also result in different stress relaxation kinetics between real and re-created pre-deformation levels. In order to provide a validation of this work, the damage model predictions should be assessed from the RC damage observed in real welded structures. To that purpose, the predictions of the initial residual stress distributions after multi-pass welding could be obtained from finite element calculations of this process (*e.g.* see (Deng et al., 2008)).

The effect of temperature on RC damage development was not found to rely solely on different stress relaxation kinetics. Actually, the intermediate testing temperature of 575°C was found to be more damaging than 550 and 600°C. A comprehensive understanding behind this phenomenon has not been provided by this work. However, a competing mechanism between residual stress relaxation and GB degradation is suspected. In order to investigate this possibility, GB degradation kinetics by carbide precipitation and impurity segregation should be quantified. Such study could potentially involve the thermal ageing of AISI 316L-type austenitic stainless steels at 550, 575 and 600°C for different lengths of time. Then, the energy needed to fracture at low temperature the thermally aged specimens could be measured (*e.g.* see (Chen et al., 2010)) and linked to quantitative measurements of intergranular carbide distributions on the intergranular fractured surfaces. Furthermore, a knowledge of the GB chemical composition after thermal exposure is lacking. In this work, Auger electron spectroscopy was attempted to that purpose but gave no results due to the tendency of austenitic stainless steel to undergo ductile fracture at low temperatures. Another approach could consist in using secondary ion mass spectrometry (SIMS), which also enables surface chemical composition analyses (*e.g.* see (Kurban et al., 2006)).

The viscoplastic constitutive model proposed in this work was calibrated from experimental AISI 316L-type steel data. Some modelling aspects such as the dislocation density static recovery was not calibrated from experimental dislocation density measurements. Further work is necessary to validate the extent of this phenomenon at high temperatures in the different tested steels. Furthermore, the residual stress relaxation predictions by finite element in the notch root regions of the CT specimens were not compared to experimental measurements. These measurements could be performed by high energy X-ray diffraction (HEXRD) or neutron diffraction as described in (Turski et al., 2008).

The simple damage model applied in this work is macroscopic and phenomenological in nature and hence does not take into account the stress and strain fields at the grain scale. A more accurate prediction of the microcrack distributions in the specimen could be attempted following a more local approach. An example is the work by Diard et al. (2002) in which they meshed representative microstructures and applied a crystal plasticity model to evaluate the local inter-

granular heterogeneity of the stress and strain fields. Then, an intergranular damage model was applied at the grain scale to assess the damage localisation. Such method should enable a better description of the intergranular damage development on specific GBs and also enable an implicit description of the pre-strain effect on GB stress localisation.

The calibrated damage model provides a useful estimation of the relaxation cracking propensity of AISI 316L-type steels at temperatures and residual stress levels outside the range in this work. However, accurate predictions of RC damage development for much longer thermal exposures (>5000 hrs) would require a more physically-based damage model which takes into account for thermally-activated GB degradation mechanisms. Furthermore, the damage evolutionary equation used in this work was not fully coupled with the viscoplastic constitutive model. Consequently, numerical damage development do not affect residual stress evolution. A better description of RC damage development should involve a different constitutive framework with a coupled damage-viscoplastic approach but is likely to be intricate to model, calibrate and implement numerically.

Bibliography

S. Allain, J.-P. Chateau, D. Dahmoun, and O. Bouaziz. Modeling of mechanical twinning in a high manganese content austenitic steel. Materials Science and Engineering: A, 387–389(0): 272 – 276, 2004. ISSN 0921-5093. 13th International Conference on the Strength of Materials.

A. Andrieu, A. Pineau, P. Joly, F. Roch, and D. Ryckelynck. Infuence of P and C intergranular segregation during manufacturing and ageing on the fracture toughness of nuclear pressure vessel steels. In 20th European Conference on Fracture (ECF 20), June 2014, Trondheim, Norway, 2014.

D. Argence and A. Pineau. Predictive metallurgy applied to creep-fatigue damage of austenitic stainless steels. In The Donald McLean Symposium Structural Materials Engineering Application Through Scientific Insight, 1995.

S. Asgari, E. El-Danaf, S.R. Kalidindi, and R.D. Doherty. Strain hardening regimes and microstructural evolution during large strain compression of low stacking fault energy fcc alloys that form deformation twins. Metallurgical and Materials Transactions A, 28(9):1781–1795, 1997. ISSN 1073-5623.

Q. Auzoux. Fissuration en relaxation des aciers inoxydables austénitiques - Influence de l'écrouissage sur l'endommagement intergranulaire. Thèses, École Nationale Supérieure des Mines de Paris, January 2004.

Q. Auzoux, L. Allais, C. Caës, B. Girard, I. Tournié, A.F. Gourgues, and A. Pineau. Intergranular damage in AISI 316L(N) austenitic stainless steel at 600°C: pre-strain and multiaxial effects. Nuclear Engineering and Design, 235(21):2227 – 2245, 2005. ISSN 0029-5493.

Q. Auzoux, L. Allais, C. Caës, I. Monnet, A.F. Gourgues, and A. Pineau. Effect of pre-strain on creep of three AISI 316 austenitic stainless steels in relation to reheat cracking of weld-affected zones. Journal of Nuclear Materials, 400(2):127 – 137, 2010. ISSN 0022-3115.

J. Besson, G. Cailletaud, J.-L. Chaboche, S. Forest, and M. Blétry. Non-Linear Mechanics of Materials. Solid Mechanics and Its Applications. Springer, 2009. ISBN 9789048133567.

A. Bolshakov, W.C. Oliver, and G.M Pharr. Influences of stress on the measurement of mechanical properties using nanoindentation: Part II – finite element simulations. Journal of Materials Research, 11:760–768, 1996. ISSN 2044-5326.

J.C. Borland. Generalized theory of super-solidus cracking in welds (and castings). British Welding Journal, 7(8):508–512, 1960.

O. Bouaziz and N. Guelton. Modelling of twip effect on work-hardening. Materials Science and Engineering: A, 319–321(0):246 – 249, 2001. ISSN 0921-5093.

O. Bouaziz, S. Allain, and C. Scott. Effect of grain and twin boundaries on the hardening mechanisms of twinning-induced plasticity steels. Scripta Materialia, 58(6):484 – 487, 2008. ISSN 1359-6462.

P.J. Bouchard, P.J. Withers, S.A. McDonald, and R.K. Heenan. Quantification of creep cavitation damage around a crack in a stainless steel pressure vessel. Acta Materialia, 52(1):23 – 34, 2004. ISSN 1359-6454.

C.L. Briant. Grain boundary segregation of phosphorus and sulfur in types 304L and 316L stainless steel and its effect on intergranular corrosion in the huey test. Metallurgical Transactions A, 18(5):691–699, 1987a. ISSN 0360-2133.

C.L. Briant. Nitrogen segregation to grain boundaries in austenitic stainless steel. Scripta Metallurgica, 21(1):71 – 74, 1987b. ISSN 0036-9748.

C.L. Briant and P.L. Andresen. Grain boundary segregation in austenitic stainless steels and its effect on intergranular corrosion and stress corrosion cracking. Metallurgical Transactions A, 19(3):495–504, 1988. ISSN 0360-2133.

E.P. Busso. Cyclic deformation of monocrystalline nickel aluminide and high temperature coatings. PhD thesis, Massachusetts Institute of Technology, 1990.

E.P. Busso and F.A. McClintock. A dislocation mechanics-based crystallographic model of a B2-type intermetallic alloy. International Journal of Plasticity, 12(1):1 – 28, 1996. ISSN 0749-6419.

M.T. Cabrillat, P. Allegre, E. Pluyette, and B. Michel. Intergranular reheat cracking in 304H components. Experiments and damage evaluation. Structural Mechanics in Reactor Technology, 16, 2001.

M. Chabaud-Reytier, L. Allais, C. Caës, P. Dubuisson, and A. Pineau. Mechanisms of stress relief cracking in titanium stabilised austenitic stainless steel. Journal of Nuclear Materials, 323(1):123 – 137, 2003. ISSN 0022-3115.

J.L. Chaboche. A review of some plasticity and viscoplasticity constitutive theories. International Journal of Plasticity, 24(10):1642 – 1693, 2008. ISSN 0749-6419. Special Issue in Honor of Jean-Louis Chaboche.

B. Chen, P.E.J. Flewitt, and D.J. Smith. Microstructural sensitivity of 316H austenitic stainless steel: residual stress relaxation and grain boundary fracture. Materials Science and Engineering A, 527(27-28):7387 – 7399, 2010. ISSN 0921-5093.

K.S. Cheong and E.P. Busso. Discrete dislocation density modelling of single phase fcc polycrystal aggregates. Acta Materialia, 52(19):5665 – 5675, 2004. ISSN 1359-6454.

M.C. Coleman, D.A. Miller, and R.A. Stevens. Reheat cracking and strategies to assure integrity of type 316 welded components. In Integrity of High-Temperature Welds, International Conference, Nottingham, pages 169–179, 1998.

R.M. Curran and A.W. Rankin. Austenitic steels in high temperature steam piping. Trans. ASME, 79:1398–1409, 1957.

A Delesse. Annals des Mines. Paris, 13:378–388, 1848.

P. Delobelle and C. Oytana. Experimental study of the flow rules of a 316 stainless steel at high and low stresses. Nuclear Engineering and Design, 83(3):333 – 348, 1984. ISSN 0029-5493.

D. Deng, H. Murakawa, and W. Liang. Numerical and experimental investigations on welding residual stress in multi-pass butt-welded austenitic stainless steel pipe. Computational Materials Science, 42(2):234 – 244, 2008. ISSN 0927-0256.

A. Dhooge. Survey on reheat cracking in austenitic stainless steels and Ni base alloys. Welding in the World, 41(3):206–219, 1998. ISSN 0043-2288.

A. Dhooge and A. Vinckier. Reheat cracking – A review of recent studies. International Journal of Pressure Vessels and Piping, 27(4):239 – 269, 1987. ISSN 0308-0161.

O. Diard, S. Leclercq, G. Rousselier, and G. Cailletaud. Distribution of normal stress at grain boundaries in multicrystals: application to an intergranular damage modeling. Computational Materials Science, 25(1–2):73 – 84, 2002. ISSN 0927-0256.

R. Ding, A. Islam, S. Wu, and J. Knott. Effect of phosphorus segregation on fracture properties of two quenched and tempered structural steels. Materials Science and Technology, 21(4): 467–475, 2005.

E. El-Danaf, S.R. Kalidindi, and R.D. Doherty. Influence of deformation path on the strain hardening behavior and microstructure evolution in low SFE FCC metals. International Journal of Plasticity, 17(9):1245 – 1265, 2001. ISSN 0749-6419.

R.W. Emerson and R.W. Jackson. The plastic ductility of austenitic piping containing welded joints at 1200 F. Research Supplement to the Welding Journal, pages 89–104, 1957.

H. Erhart and H. J. Grabke. Equilibrium segregation of phosphorus at grain boundaries of Fe-P, Fe-C-P, Fe-Cr-P, and Fe-Cr-C-P alloys. Metal Science, 15(9):401–408, 1981a.

H. Erhart and H.J. Grabke. Site competition in grain boundary segregation of phosphorus and nitrogen in iron. Scripta Metallurgica, 15(5):531 – 534, 1981b. ISSN 0036-9748.

H. Erhart and M. Paju. Phosphorus segregation in austenite. Scripta Materialia, 17:171–174, 1983.

X. Feaugas. On the origin of the tensile flow stress in the stainless steel AISI 316L at 300 K: back stress and effective stress. Acta Materialia, 47(13):3617 – 3632, 1999. ISSN 1359-6454.

X. Feaugas and C. Gaudin. Ratchetting process in the stainless steel AISI 316L at 300 K: an experimental investigation. International Journal of Plasticity, 20(4–5):643 – 662, 2004. ISSN 0749-6419.

D. François, A. Pineau, and A. Zaoui. Mechanical Behaviour of Materials: Volume I: Micro- and Macroscopic Constitutive Behaviour. Springer, 2012. ISBN 9789400725461.

R.L. Fullman. Measurement of approximately cylindrical particles in opaque samples. Journal of Metals, 5:1267–1268, 1953.

M. Herbig, M. Kuzmina, C. Haase, R.K.W. Marceau, I. Gutierrez-Urrutia, D. Haley, D.A. Molodov, P. Choi, and D. Raabe. Grain boundary segregation in Fe-Mn-C twinning-induced plasticity steels studied by correlative electron backscatter diffraction and atom probe tomography. Acta Materialia, 83(0):37 – 47, 2015. ISSN 1359-6454.

T.R. Heyward and J.I. Goldstein. Ternary diffusion in the α and γ phases of the Fe–Ni–P system. Metallurgical Transactions, 4(10):2335–2342, 1973. ISSN 0360-2133.

H. Hong and S. Nam. Improvement of creep-fatigue life by the modification of carbide characteristics through grain boundary serration in an AISI 304 stainless steel. Journal of Materials Science, 38(7):1535–1542, 2003. ISSN 0022-2461.

H.U. Hong, B.S. Rho, and S.W. Nam. Correlation of the $M_{23}C_6$ precipitation morphology with grain boundary characteristics in austenitic stainless steel. Materials Science and Engineering: A, 318(1–2):285 – 292, 2001. ISSN 0921-5093.

J. Hong, S. Nam, and S. Choi. The influences of sulphur and phosphorus additions on the creep cavitation characteristics in type 304 stainless steels. Journal of Materials Science, 21: 3966–3976, 1986. ISSN 0022-2461.

S. Hossain, C.E. Truman, D.J. Smith, R.L. Peng, and U. Stuhr. A study of the generation and creep relaxation of triaxial residual stresses in stainless steel. International Journal of Solids and Structures, 44(9):3004 – 3020, 2007. ISSN 0020-7683.

S. Hossain, C.E. Truman, and D.J. Smith. Generation of residual stress and plastic strain in a fracture mechanics specimen to study the formation of creep damage in type 316 stainless steel. Fatigue & Fracture of Engineering Materials & Structures, 34:654–666, 2010.

M. Huang, O. Bouaziz, D. Barbier, and S. Allain. Modelling the effect of carbon on deformation behaviour of twinning induced plasticity steels. Journal of Materials Science, 46(23):7410–7414, 2011. ISSN 0022-2461.

N. Huber and J. Heerens. On the effect of a general residual stress state on indentation and hardness testing. Acta Materialia, 56(20):6205 – 6213, 2008. ISSN 1359-6454.

R. Jones, V. Randle, and G. Owen. Carbide precipitation and grain boundary plane selection in overaged type 316 austenitic stainless steel. Materials Science and Engineering: A, 496(1–2): 256 – 261, 2008. ISSN 0921-5093.

M. Kahziz. Experimental and numerical investigation of ductile damage mechanisms and edge fracture in advanced automotive steels. PhD thesis, Ecole des Mines de Paris, 2016.

S.R. Kalidindi. Modeling the strain hardening response of low SFE FCC alloys. International Journal of Plasticity, 14(12):1265 – 1277, 1998. ISSN 0749-6419.

I. Karaman, H. Sehitoglu, Y.I. Chumlyakov, H. Maier, and I.V. Kireeva. The effect of twinning and slip on the Bauschinger effect of hadfield steel single crystals. Metallurgical and Materials Transactions A, 32(13):695–706, 2001a. ISSN 1073-5623.

I. Karaman, H. Sehitoglu, H.J Maier, and Y.I Chumlyakov. Competing mechanisms and modeling of deformation in austenitic stainless steel single crystals with and without nitrogen. Acta Materialia, 49(19):3919 – 3933, 2001b. ISSN 1359-6454.

I. Karaman, H. Sehitoglu, Y.I. Chumlyakov, and H.J. Maier. The deformation of low-stacking-fault-energy austenitic steels. JOM, 54(7):31–37, 2002. ISSN 1047-4838.

G.R. Kegg, J.M. Silcock, and D.R.F. West. The effect of phosphorus additions and cooling rate on the precipitation of $M_{23}C_6$ in austenite. Metal Science, 8(1):337–343, 1974.

K.J. Kim, H.U. Hong, K.S. Min, and S.W. Nam. Correlation between the carbide morphology and cavity nucleation in an austenitic stainless steels under creep-fatigue. Materials Science and Engineering: A, 387–389(0):531 – 535, 2004. ISSN 0921-5093. 13th International Conference on the Strength of Materials.

U.F. Kocks. A statistical theory of flow stress and work-hardening. Philosophical Magazine, 13 (123):541–566, 1966.

U.F. Kocks and H. Mecking. Physics and phenomenology of strain hardening: the FCC case. Progress in Materials Science, 48(3):171 – 273, 2003. ISSN 0079-6425.

U.F. Kocks, A.S. Argon, and M.F. Ashby. Progress in materials science. Pergamon Press: Oxford, 19:1–129, 1975.

M. Kurban, U. Erb, and K.T. Aust. A grain boundary characterization study of boron segregation and carbide precipitation in alloy 304 austenitic stainless steel. Scripta Materialia, 54(6):1053 – 1058, 2006. ISSN 1359-6462.

P. Lacombe, B. Baroux, and G. Béranger. Les Aciers inoxydables. Les Éditions de Physique, 1990. ISBN 9782868831422.

R. Lagneborg. Development and refinement of the recovery-creep theory. Metal Science, 3(1): 161–168, 1969.

R. Lagneborg. A modified recovery-creep model and its evaluation. Metal Science, 6(1):127–133, 1972.

C. Landron. Ductile damage characterization in Dual-Phase steels using X-ray tomography. PhD thesis, Institut National des Sciences Appliquée de Lyon, 2012.

C. Landron, E. Maire, O. Bouaziz, J. Adrien, L. Lecarme, and A. Bareggi. Validation of void growth models using X-ray microtomography characterization of damage in dual phase steels. Acta Materialia, 59(20):7564 – 7573, 2011. ISSN 1359-6454.

F. Lecroisey. Transformations martensitiques induites par déformation plastique dans le système Fe-Ni-Cr-C. PhD thesis, Université de Nancy 1, 1971.

C. Levaillant. Approche métallographique de l'endommagement d'aciers inoxydables austénitiques sollicités en fatigue plastique ou en fluage. PhD thesis, 1984.

D.F. Li, C.M. Davies, S.Y. Zhang, C. Dickinson, and N.P. O'Dowd. The effect of prior deformation on subsequent microplasticity and damage evolution in an austenitic stainless steel at elevated temperature. Acta Materialia, 61(10):3575 – 3584, 2013. ISSN 1359-6454.

L.E. Lindgren, K. Domkin, and S. Hansson. Dislocations, vacancies and solute diffusion in physical based plasticity model for AISI 316L. Mechanics of Materials, 40(11):907 – 919, 2008. ISSN 0167-6636.

K.H. Lo, C.H. Shek, and J.K.L. Lai. Recent developments in stainless steels. Materials Science and Engineering: R: Reports, 65(4–6):39 – 104, 2009. ISSN 0927-796X.

A.M. Lush, G. Weber, and L. Anand. An implicit time-integration procedure for a set of internal variable constitutive equations for isotropic elasto-viscoplasticity. International Journal of Plasticity, 5(5):521 – 549, 1989. ISSN 0749-6419.

M.D. Mathew, G. Sasikala, K. Bhanu Sankara Rao, and S.L. Mannan. Influence of carbon and nitrogen on the creep properties of type 316 stainless steel at 873 K. Materials Science and Engineering: A, 148(2):253 – 260, 1991. ISSN 0921-5093.

D. McLean. Grain Boundaries in Metals. Clarendon Press, 1957.

C.F. Meitzner. Stress relief cracking in steel weldments. Welding Research Council Bulletin, (211), 1975.

B. Michel. Formulation of a new intergranular creep damage model for austenitic stainless steels. Nuclear Engineering and Design, 227(2):161 – 174, 2004. ISSN 0029-5493.

M. Militzer, W.P. Sun, and J.J. Jonas. Modelling the effect of deformation-induced vacancies on segregation and precipitation. Acta Metallurgica et Materialia, 42(1):133 – 141, 1994. ISSN 0956-7151.

R.A. Moen and G.V. Smith. A consideration on limits of cold working in nuclear construction. Journal of Engineering Materials and Technology, 97(2):162–171, 1975.

C. Naudin, J.M. Frund, and A. Pineau. Intergranular fracture stress and phosphorus grain boundary segregation of a Mn–Ni–Mo steel. Scripta Materialia, 40(9):1013–1019, 1999.

W.D. Nix, J.C. Gibeling, and D.A. Hughes. Time-dependent deformation of metals. Metallurgical Transactions A, 16(12):2215–2226, 1985. ISSN 0360-2133.

T. Ogura, T. Watanabe, S. Karashima, and T. Masumoto. Dependence of phosphorus segregation on grain boundary crystallography in an Fe–Ni–Cr alloy. Acta Metallurgica, 35(7):1807 – 1814, 1987. ISSN 0001-6160.

M. Paju and R. Möller. The effect of boron on phosphorus segregation in austenite. Scripta Metallurgica, 18(8):813–815, 1984.

M. Paju, H. Viefhaus, and H.J. Grabke. Phosphorus segregation in austenite in Fe–P–C, Fe–P–B and Fe–P–C–B alloys. Steel Res., 59(8):336–343, 1988.

R. Piques. Mécanique et mécanismes de l'amorçage et de la propagation des fissures en viscoplasticité dans un acier inoxydable austénitique. PhD thesis, 1989.

H. Pommier, E.P. Busso, T.F. Morgeneyer, and A. Pineau. Intergranular damage during stress relaxation in AISI 316L-type austenitic stainless steels: Effect of carbon, nitrogen and phosphorus contents. Acta Materialia, 103:893 – 908, 2016. ISSN 1359-6454.

D. Poquillon. Approche locale : fissuration a haute température dans un acier inoxydable austénitique sous chargements thermomécaniques. simulations numériques et validations expérimentales. PhD thesis, 1997.

R.P. Reed, R.L. Tobler, and J.W. Elmer. Temperature dependence of flow strength of selected austenitic stainless steels. In Austenitic Steels at Low Temperatures, pages 105–116. Springer US, 1983. ISBN 978-1-4613-3732-4.

L. Rémy. Kinetics of fcc deformation twinning and its relationship to stress-strain behaviour. Acta Metallurgica, 26(3):443 – 451, 1978. ISSN 0001-6160.

L. Rémy. The interaction between slip and twinning systems and the influence of twinning on the mechanical behavior of fcc metals and alloys. Metallurgical Transactions A, 12(3):387–408, 1981. ISSN 0360-2133.

M. Chabaud Reytier. Etude de la fissuration différée par relaxation d'un acier inoxydable austénitique stabilisé au titane. PhD thesis, 1999.

R. Sandström and R. Lagneborg. A model for hot working occurring by recrystallization. Acta Metallurgica, 23(3):387 – 398, 1975. ISSN 0001-6160.

J. Schwartz. Approche non locale en plasticité cristalline : application à l'étude du comportement mécanique de l'acier AISI 316LN en fatigue oligocyclique. Phd thesis, Ecole Centrale Paris, June 2011.

P. Ševc, J. Janovec, P. Lejček, P.Z.áhumenský, and J. Blach. Thermodynamics of phosphorus grain boundary segregation in 17Cr12Ni austenitic steel. Scripta Materialia, 46(1):7 – 12, 2002. ISSN 1359-6462.

A.H. Sherry, M. Turski, M.A. Wilkes, D.W. Beardsmore, P.J. Withers, and P.J. Bouchard. The development of a compact specimen to study the influence of residual stresses on fracture. In Engineering structural integrity assessment, 2002.

T.R. Simes, S.G. Mellor, and D.A. Hills. A note on the influence of residual stress on measured hardness. The Journal of Strain Analysis for Engineering Design, 19(2):135–137, 1984.

C.W. Sinclair, W.J. Poole, and Y. Bréchet. A model for the grain size dependent work hardening of copper. Scripta Materialia, 55(8):739 – 742, 2006. ISSN 1359-6462.

R.P. Skelton, I.W. Goodall, G.A. Webster, and M.W. Spindler. Factors affecting reheat cracking in the HAZ of austenitic steel weldments. International Journal of Pressure Vessels and Piping, 80(7-8):441 – 451, 2003. ISSN 0308-0161.

M.W. Spindler. The multiaxial creep ductility of austenitic stainless steels. Fatigue & Fracture of Engineering Materials & Structures, 27(4):273–281, 2004a. ISSN 1460-2695.

M.W. Spindler. The use of borland specimens to reproduce reheat cracking in type 316H. In Int. Conf. on High Temperature Plant Integrity and Life Extension, 2004b.

M.W. Spindler. An improved method for calculation of creep damage during creep–fatigue cycling. Materials Science and Technology, 23(12):1461–1470, 2007.

D.R. Steinmetz, T. Jäpel, B. Wietbrock, P. Eisenlohr, I. Gutierrez-Urrutia, A. Saeed–Akbari, T. Hickel, F. Roters, and D. Raabe. Revealing the strain-hardening behavior of twinning-induced plasticity steels: Theory, simulations, experiments. Acta Materialia, 61(2):494 – 510, 2013. ISSN 1359-6454.

R.D. Thomas. HAZ cracking in thick sections of austenitic stainless steels–I. Weld. J., 63(12): 24–32, 1984.

T.Y. Tsui, W.C. Oliver, and G.M. Pharr. Influences of stress on the measurement of mechanical properties using nanoindentation: Part I – experimental studies in an aluminum alloy. Journal of Materials Research, 11:752–759, 1996. ISSN 2044-5326.

M. Turski, P.J. Bouchard, A. Steuwer, and P.J. Withers. Residual stress driven creep cracking in AISI type 316 stainless steel. Acta Materialia, 56(14):3598 – 3612, 2008. ISSN 1359-6454.

E.E. Underwood. Quantitative stereology. Addison-Wesley series in metallurgy and materials. Addison-Wesley Pub. Co., 1970.

J.C. Van Wortel. Relaxation cracking in the process industry, an underestimated problem. Maintenance for Managing Life and Performance, pages 637–647, 1998.

J.A Venables. The nucleation and propagation of deformation twins. Journal of Physics and Chemistry of Solids, 25(7):693 – 700, 1964. ISSN 0022-3697.

B. Weiss and R. Stickler. Phase instabilities during high temperature exposure of 316 austenitic stainless steel. Metallurgical Transactions, 3(4):851–866, 1972.

J. Weiss. Endommagement en viscoplasticité cyclique sous chargement multiaxial a haute température d'un acier inoxydable austénitique. PhD thesis, 1992.

M. Willis, A. McDonaugh-Smith, and R. Hales. Prestrain effects on creep ductility of a 316 stainless steel light forging. International Journal of Pressure Vessels and Piping, 76(6):355 – 359, 1999. ISSN 0308-0161.

B. Wilshire and M. Willis. Mechanisms of strain accumulation and damage development during creep of prestrained 316 stainless steels. Metallurgical and Materials Transactions A: Physical Metallurgy and Materials Science, 35 A(2):563–571, 2004.

M. Yoshida. Endommagement intergranulaire de fluage dans un acier inoxydable 17 Cr-12 Ni. PhD thesis, Evry, 1985.

M. Yoshida, C. Levaillant, R. Piques, and A. Pineau. Quantitative study of intergranular damage in an austenitic stainless steel on smooth and notched bars. High Temperature Fracture Mechanisms and Mechanics, pages 3–21, 1987.

R.N. Younger and R.G. Baker. Heat affected zone cracking in welded high-temperature austenitic steels. Journal of the Iron and Steel Institute, 196:1S8, 1960.

R.N. Younger, R.G. Baker, and D.M. Haddrill. Post-weld heat treatement of high-temperature austenitic steels. Journal of the Iron and Steel Institute, 201(8):693, 1963.

Zset. http://www.zset-software.com. Online, 2015.

APPENDIX A

Material microstructures

The material microstructures are presented below in Figs. A.1 and A.2. Left figures correspond to the annealed state while right ones show the cold rolled microstructure in a close-up view. For each material, the grain size, d_0, and the hardness are given.

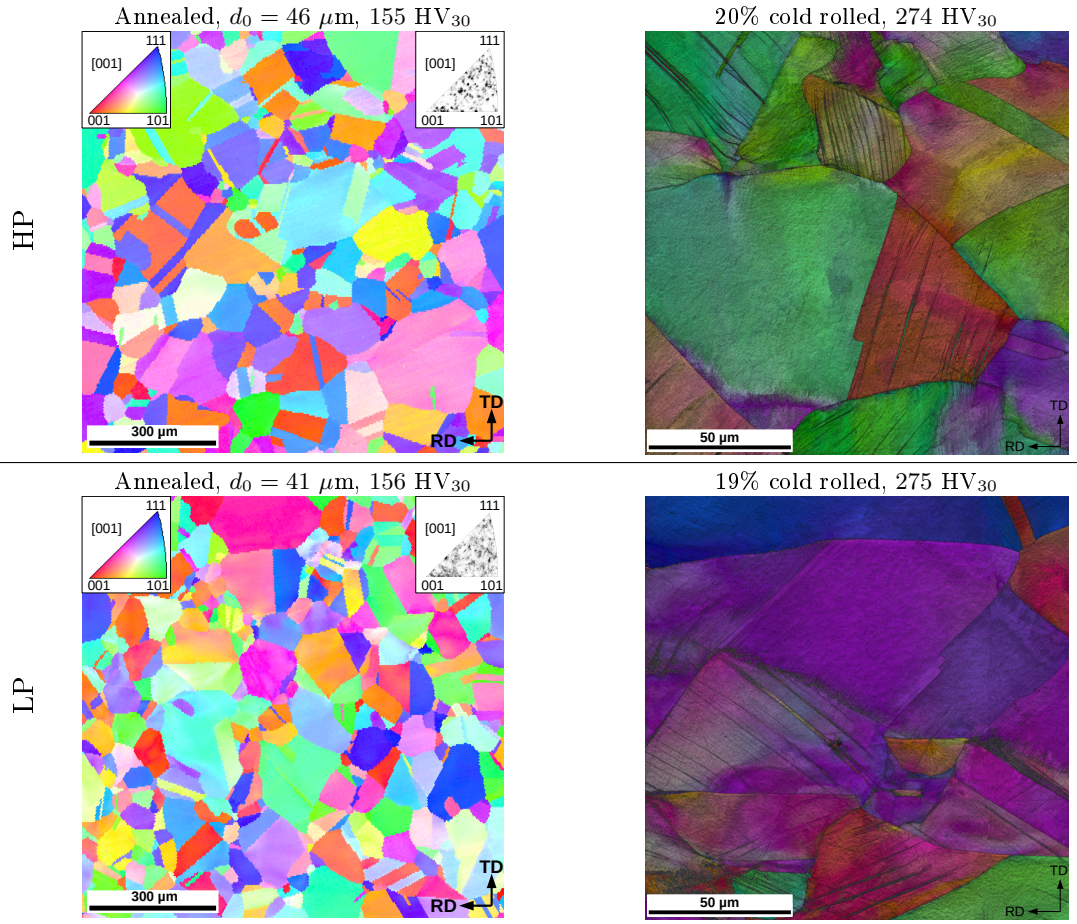

Figure A.1: Microstructure of the low and high phosphorus (LP and HP) austenitic stainless steels observed by EBSD: (a) annealed state shown in inverse pole figure (IPF) and (b) cold-rolled state, in a close-up view, shown by a superposition of the IPF and image quality (IQ) maps.

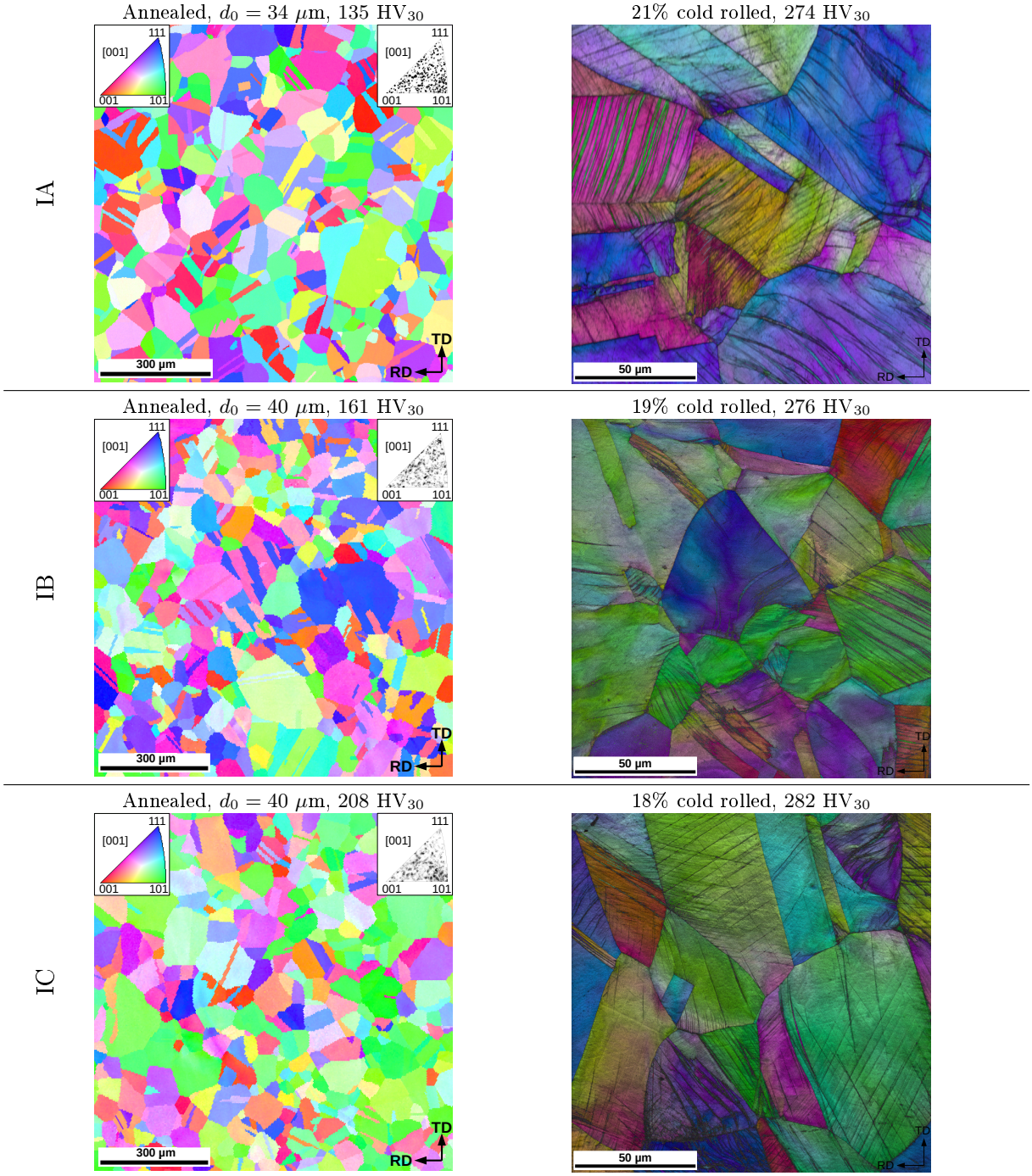

Figure A.2: Microstructure of the industrial-type austenitic stainless steels observed by EBSD: (a) annealed state shown in inverse pole figure (IPF) and (b) cold-rolled state, in a close-up view, shown by a superposition of the IPF and image quality (IQ) maps.

APPENDIX B

Additional images

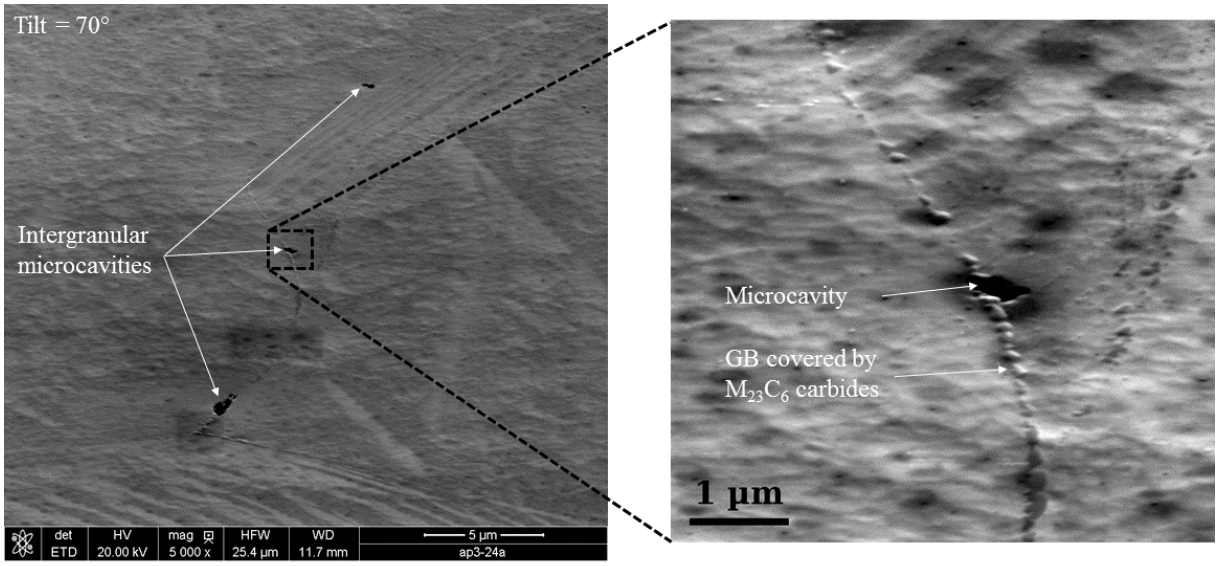

Figure B.1: (a) Mid-thickness SEM micrograph in the notch root region of the IA steel CT specimen tested at 823 K for 4313 hrs (e=10 mm, r=1 mm) and (b) the same region in a close-up view.

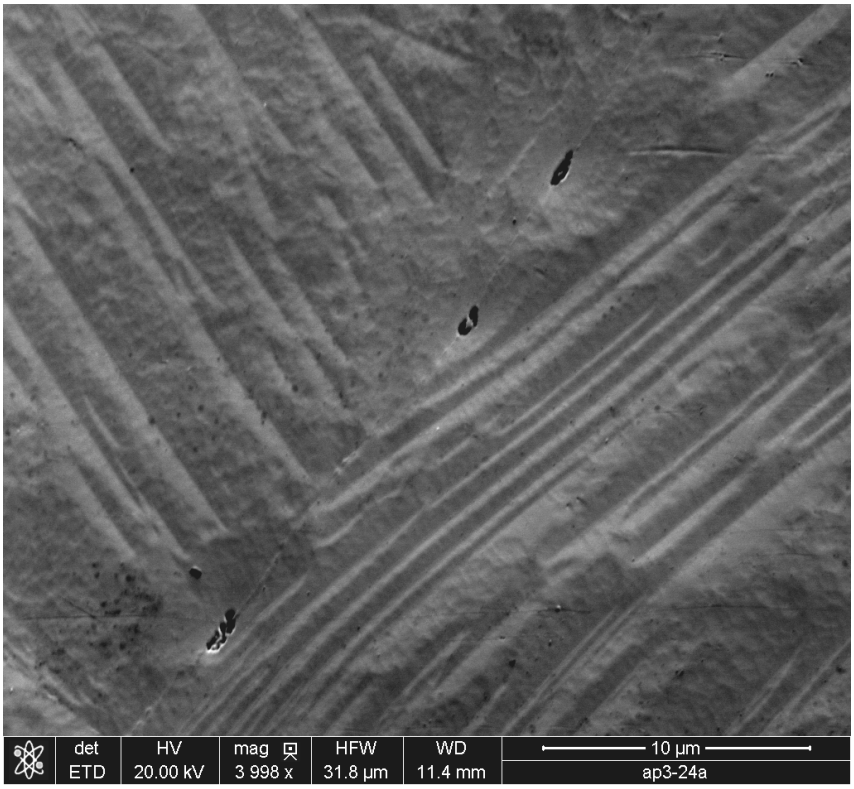

Figure B.2: Mid-thickness SEM micrograph in the notch root region of the IA steel CT specimen tested at 823 K for 4313 hrs (e=10 mm, r=1 mm).

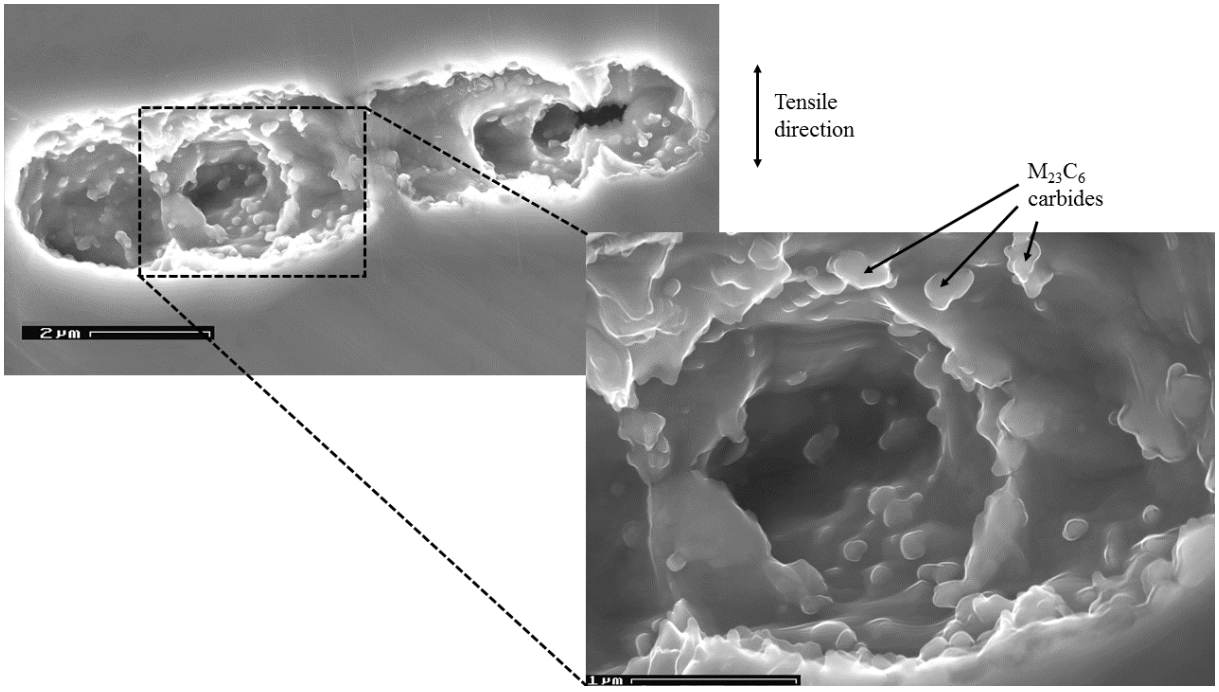

Figure B.3: SEM micrograph in the notch root region of the IA steel CT specimen tested at 823 K for 2946 hrs (e=10 mm, r=1 mm) and deformed *insitu* up to ∼10% true plastic strain.

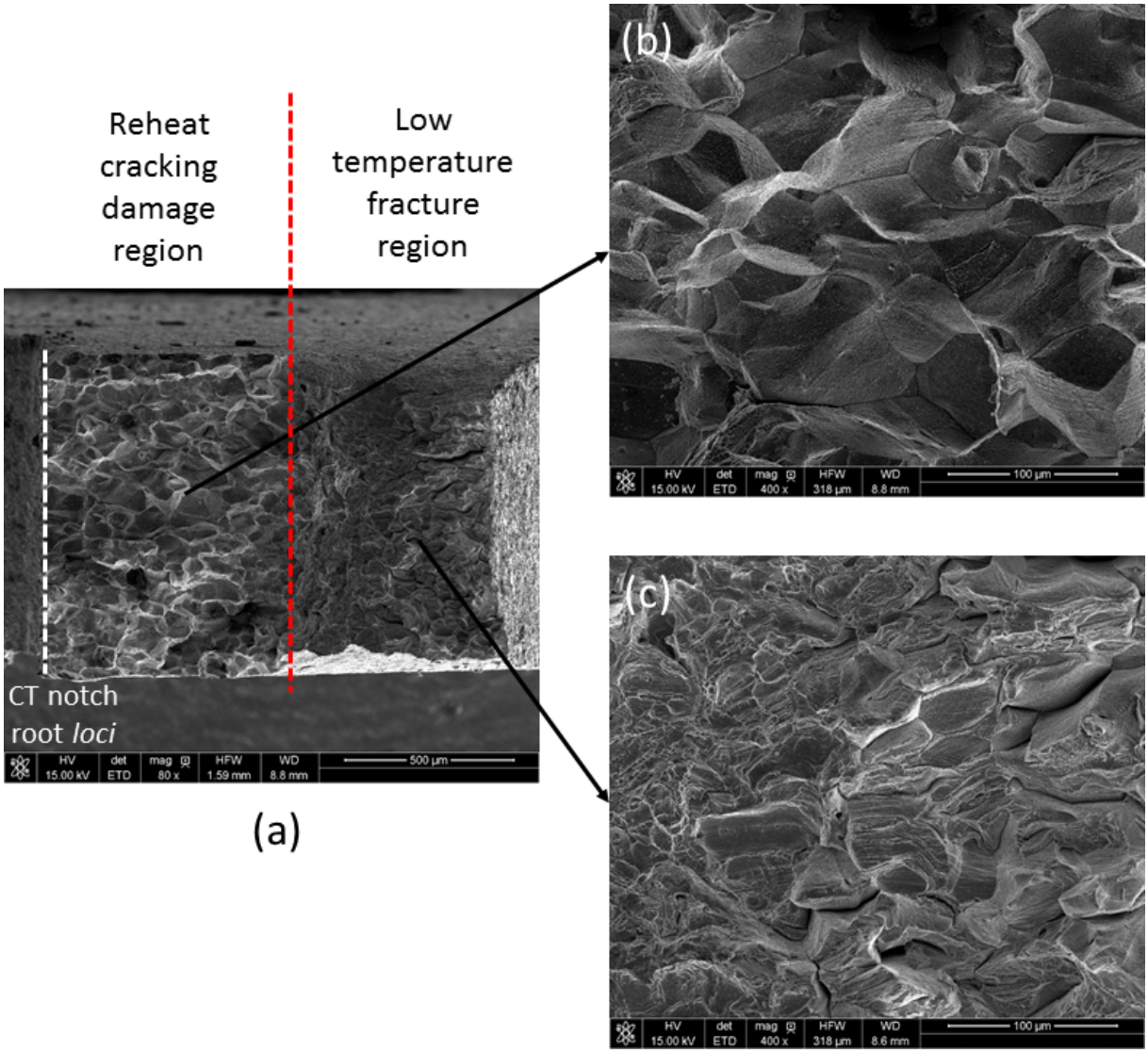

Figure B.4: (a) SEM fracture surface micrograph in the notch root region of IB steel CT specimen tested at 848 K for 3621 hrs (e=20 mm, r=0.5 mm) which exhibits (b) the reheat cracking damaged surface and (c) the final fracture surface obtained at liquid nitrogen temperature.

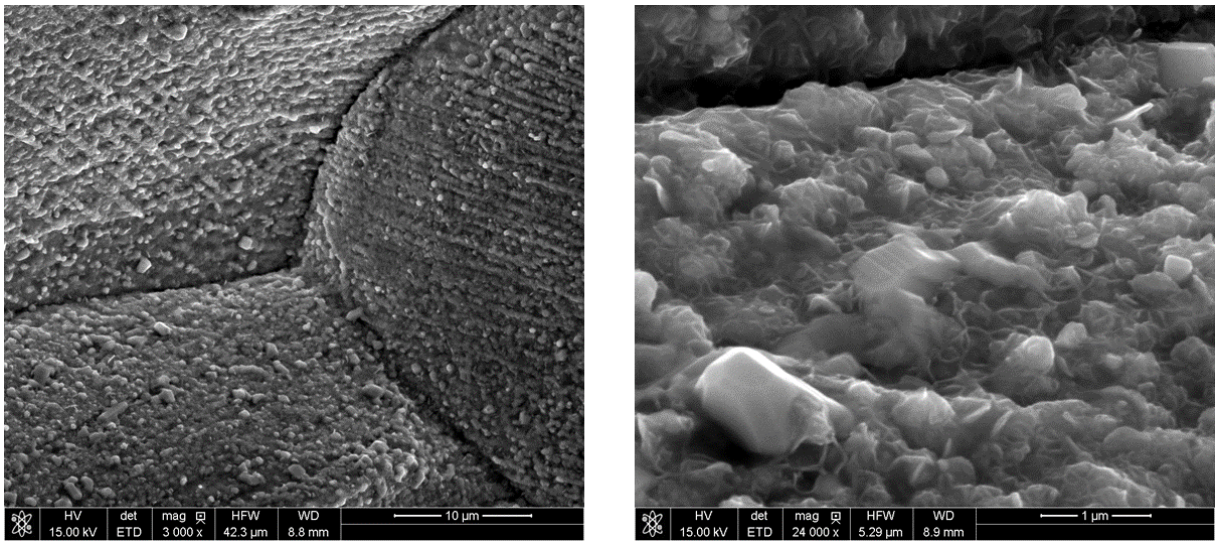

Figure B.5: Close-up views of the reheat cracking damaged region shown in Figure B.4. GBs are covered by carbides and oxides.

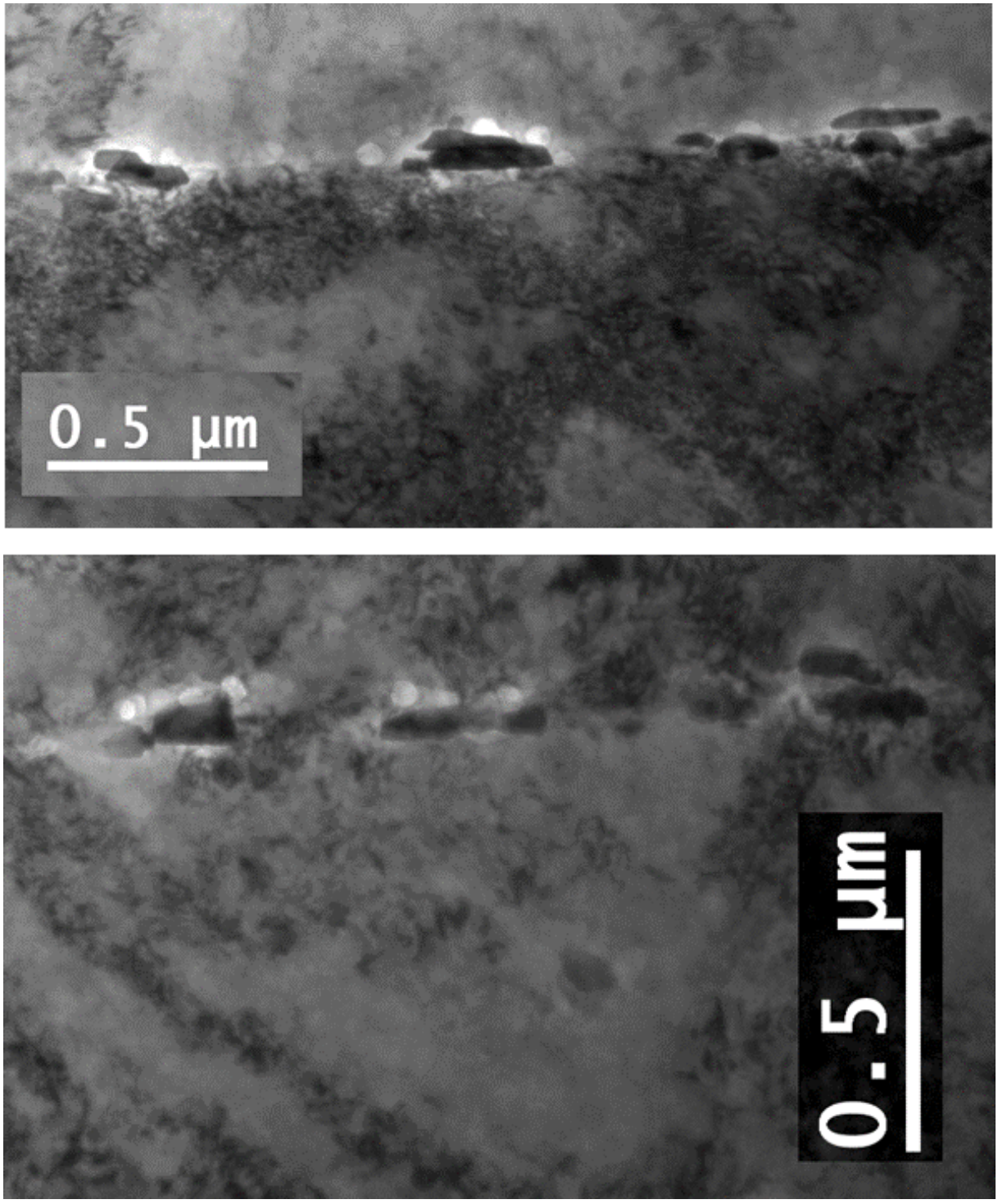

Figure B.6: Intergranular $M_{23}C_6$ carbides and nanocavities observed by TEM in two thin foils machined from the notch root region of the IB steel CT specimen tested at 848 K for 3621 hrs.

APPENDIX C

In situ microcrack opening by synchrotron X-ray tomography

In chapter 2, the *in situ* microcrack opening in the notch root regions of the CT specimens was described. This appendix presents the *in situ* microcrack opening visualisations during tensile deformation observed by synchrotron X-ray tomography. The scanned volume locations, dimensions and orientations in the CT specimens are schematically shown in Figure C.1. The corresponding results are presented in Fig. C.2 to C.5.

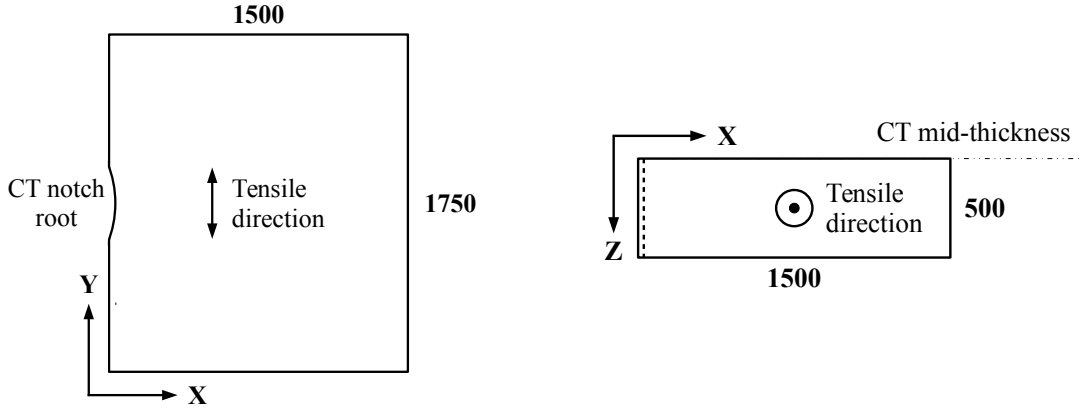

Figure C.1: Schematic representation of the locations, dimensions and orientations of the *in situ* tomography scans in the CT specimens (dimensions in μm)

IB steel CT specimen (r=1 mm, e=20 mm) tested at **600°C** for 3621 hrs.

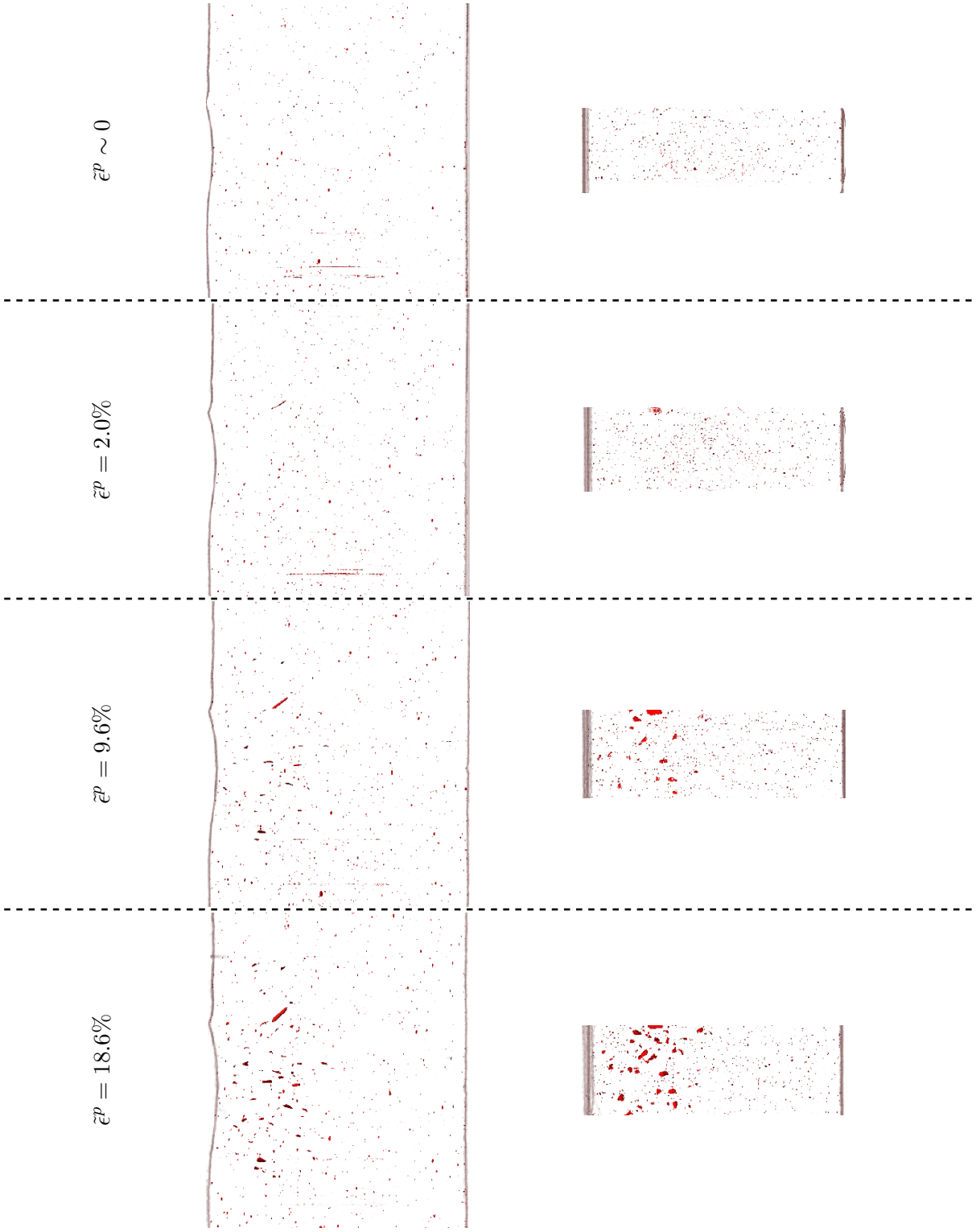

Figure C.2: Projection of intergranular damage identified by synchrotron X-ray tomography: (left) in the Z-direction, (right) in the Y-direction (the scan dimensions and orientations correspond to those of Figure C.1)

IB steel CT specimen (r=1 mm, e=20 mm) tested at **575°C** for 3621 hrs.

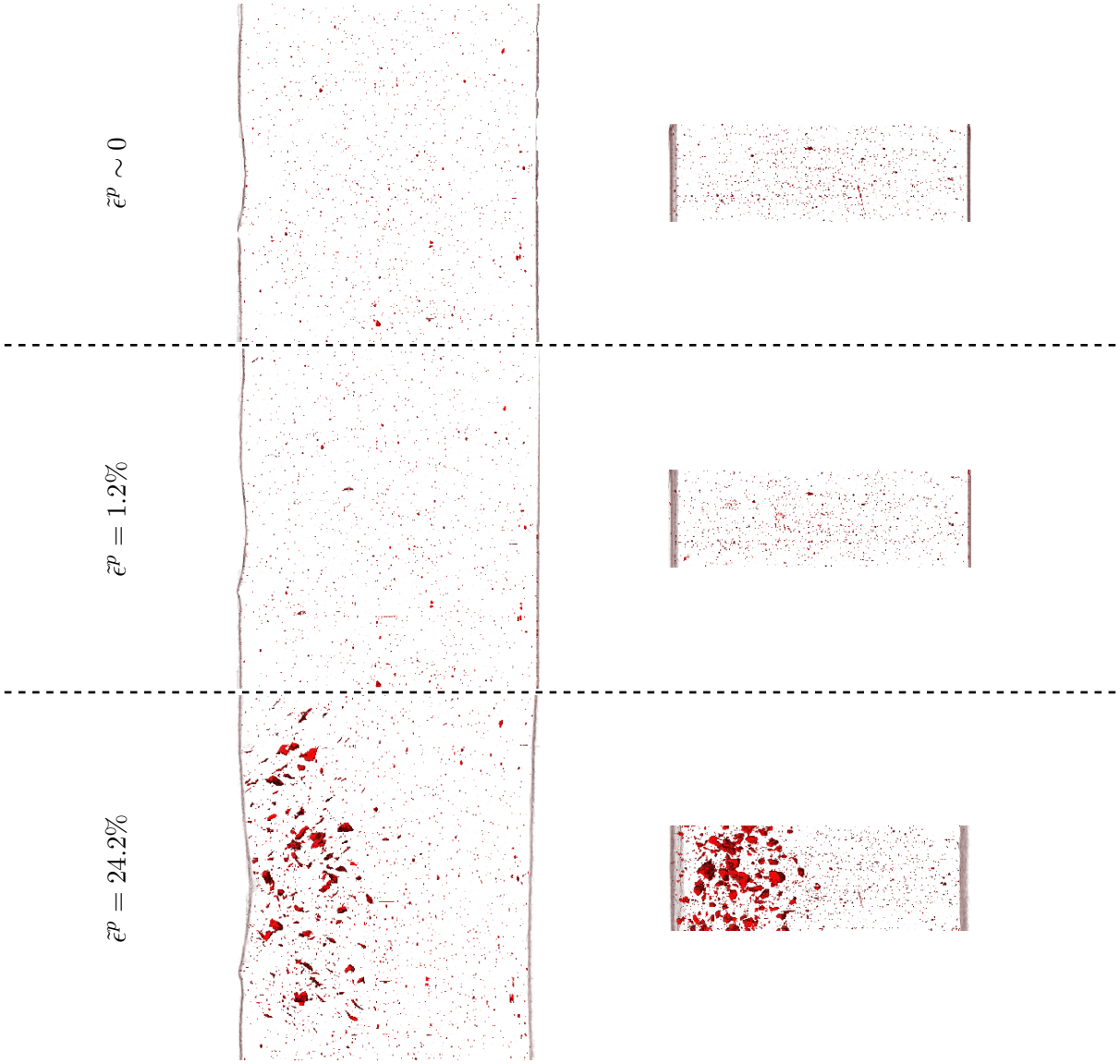

Figure C.3: Projection of intergranular damage identified by synchrotron X-ray tomography: (left) in the Z-direction, (right) in the Y-direction (the scan dimensions and orientations correspond to those of Figure C.1)

IB steel CT specimen (r=1 mm, e=20 mm) tested at **550°C** for 3621 hrs.

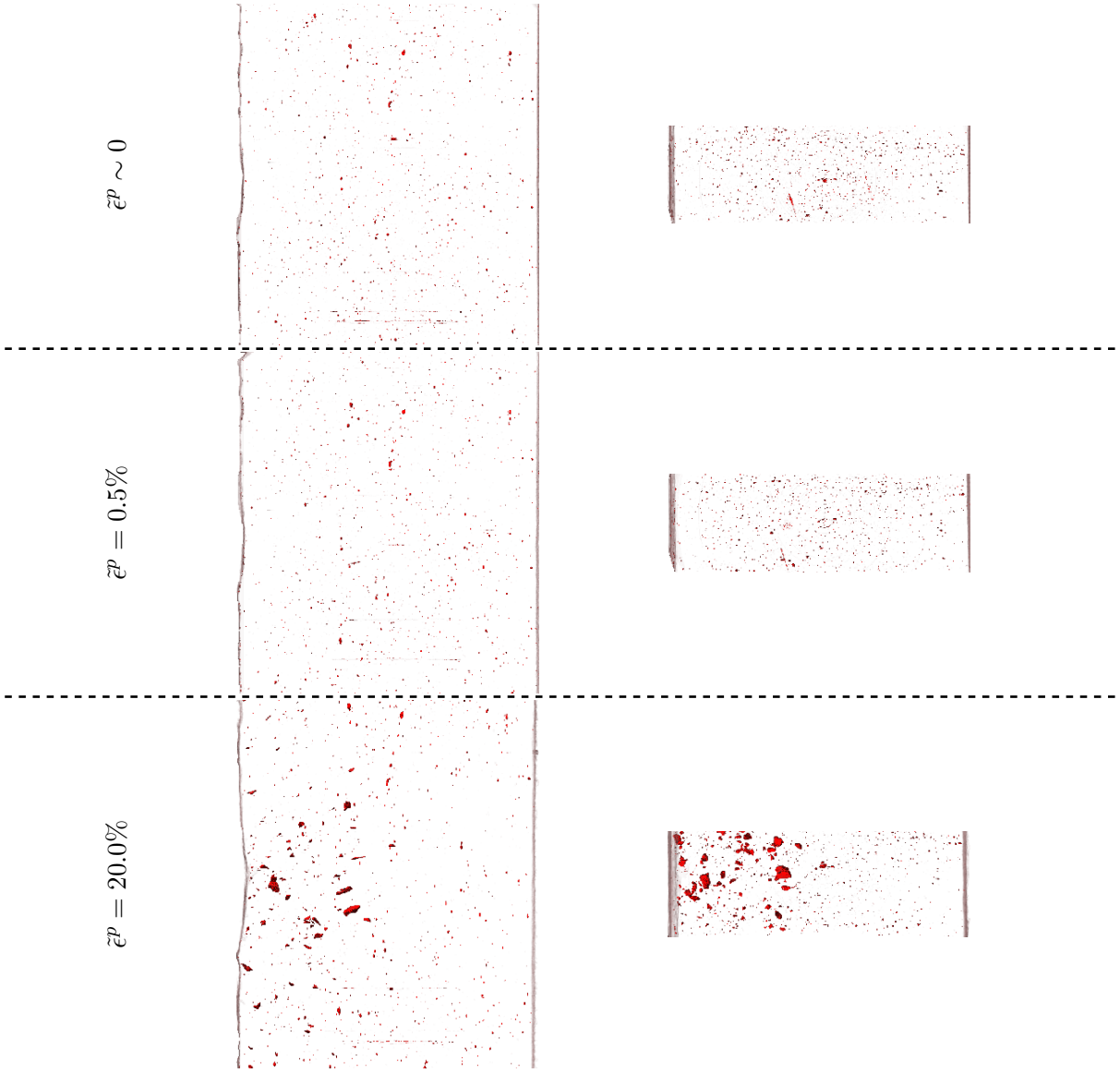

Figure C.4: Projection of intergranular damage identified by synchrotron X-ray tomography: (left) in the Z-direction, (right) in the Y-direction (the scan dimensions and orientations correspond to those of Figure C.1)

IB steel CT specimen (**r=2 mm**, e=20 mm) tested at **575°C** for 3621 hrs.

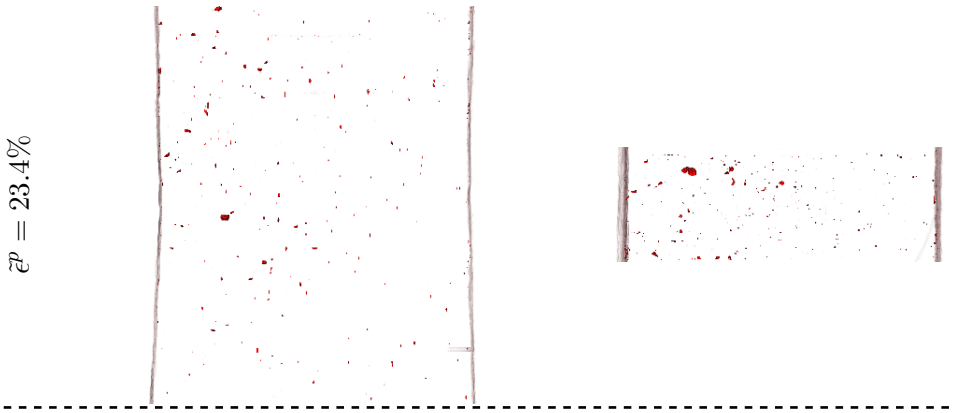

IB steel CT specimen (**r=0.5 mm**, e=20 mm) tested at **575°C** for 3621 hrs.

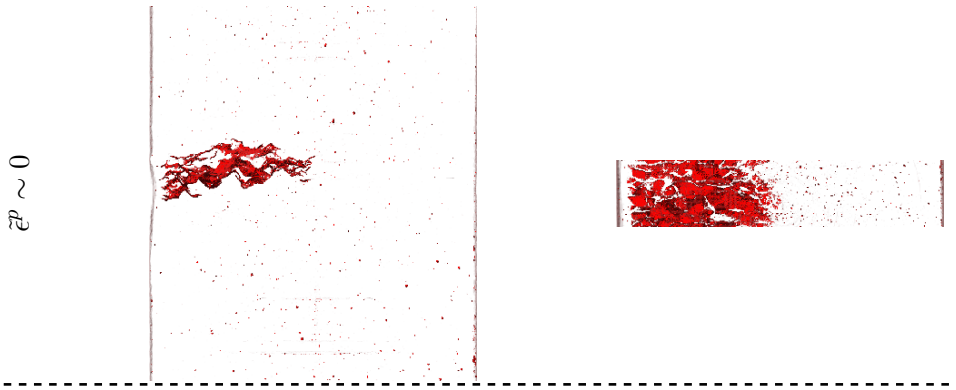

IB steel CT specimen (r=1 mm, **e=10 mm**) tested at **575°C** for **1455 hrs**.

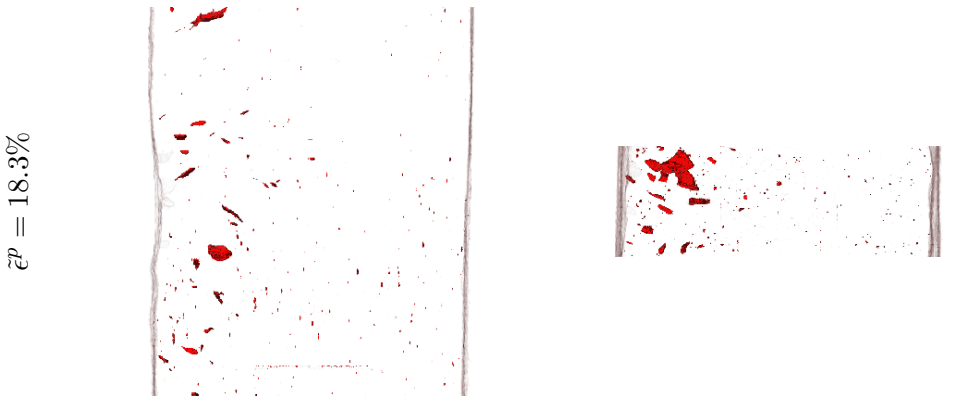

Figure C.5: Projection of intergranular damage identified by synchrotron X-ray tomography: (left) in the Z-direction, (right) in the Y-direction (the scan dimensions and orientations correspond to those of Figure C.1)

APPENDIX D

Langmuir-McLean model

The GB equilibrium monolayer coverage of the solute of interest, C_{∞}^{GB} is a function of its bulk concentration, C^B, the temperature, T, and its Gibbs energy of segregation, ΔG^0 (McLean, 1957). When assuming that C^B is small, then

$$C_{eq}^{GB} = \frac{C^B exp(\Delta G^0/RT)}{1 + C^B exp(\Delta G^0/RT)}. \tag{D.1}$$

The GB monolayer coverage of the solute of interest at time t, $C^{GB}(t)$, is expressed as (McLean, 1957):

$$C^{GB}(t) = C_{eq1}^{GB} - C^B(\alpha_1 - \alpha_0) exp\left(\frac{4Dt}{\alpha_1^2\delta^2}\right) erfc\left(\frac{2\sqrt{Dt}}{\alpha_1\delta}\right), \tag{D.2}$$

with, C_{eqi}^{GB}, the GB equilibrium concentration at temperature T_i, D, the solute diffusion coefficient in the bulk material at temperature T_1, δ, the GB thickness, $\alpha_1 = C_{eq1}^{GB}/C^B$ and $\alpha_0 = C_{eq0}^{GB}/C^B$. The parameters used to predicted GB monolayer coverage of P were taken from the literature (see Table D.1). The diffusion coefficient, D, was identified by Heyward *et al.* (Heyward and Goldstein, 1973) in a Fe-Ni-P grade in the 1173-1473 K temperature range (austenitic phase). The Gibbs energy for the P segregation was taken from the work of Erhart *et al.* (Erhart and Paju, 1983) in Fe-P+(C,Cr, Ni,Mn,V) grades (austenitic phase).

Table D.1: Langmuir-McLean model parameters for P segregation in γ-iron.

Parameter	Value	Reference
$\Delta G^0 = \Delta H - T\Delta S$	$\Delta H = -32$ kJ.mol^{-1} $\Delta S = 17$ kJ.K^{-1}.mol^{-1}	(Erhart and Paju, 1983)
$D = Aexp\left(-\frac{Q}{RT}\right)$	A=0.51 cm^{2}s^{-1} Q=230.2 kJ.K^{-1}.mol^{-1}	(Heyward and Goldstein, 1973)
δ	0.8 nm	(McLean, 1957)

APPENDIX E

Constitutive model parameters for the IB and IC steels

In chapter 3, a viscoplastic constitutive model was presented and calibrated from the IA steel experimental data mainly obtained in this work. This appendix presents the calibration of the constitutive model parameters for the IB and IC steels. In chapter 2, it was shown that the mechanical responses at room temperature of the five cold rolled materials were similar (see Figure 2.3). However, IA, IB and IC steels stress relaxation responses were found to be different (see Figure 2.7). Consequently, it was assumed that the only parameters to re-calibrate in order to reproduce the mechanical behaviour of the IB and IC steels were those affecting significantly stress relaxation through the dislocation static recovery kinetics, *i.e.* Γ_0, Q and $\rho_{eq}(\theta)$ (see Eqs. H.9). It should be noted that these parameters hardly affect the quasi-rate-independent material behaviour. Their values are given in Table E.1. A comparison between the experimental stress relaxations (same data as in Figure 2.7) and the model responses for the IB and IC steels is shown in Figure E.1. The static recovery parameter calibration enabled a good reproduction of the IB and IC steel stress relaxation behaviour (all other parameters being the same as given in Appendix F). The predicted dislocation densities in the IA, IB and IC steels at the end of the stress relaxation tests are given in Table E.2. Further experimental measurements of the material dislocation densities after ∼3500 hrs stress relaxation are necessary to corroborate these numerical predictions.

Table E.1: Static recovery parameters for the IB and IC steels

	Γ_0 [m^2s^{-1}]	Q [J]	$\rho_{eq}(\theta)$ [m^{-2}]
IB steel	3.5×10^{-16}	1.8×10^{-19}	$-3.12 \times 10^{12}\theta + 2.8178 \times 10^{15}$
IC steel	1.0×10^{-16}	1.7×10^{-19}	$-1.4 \times 10^{12}\theta + 1.3422 \times 10^{15}$

Table E.2: Constitutive model predictions of the IA, IB and IC steel dislocation densities (in [m^{-2}]) after 3500 hrs of stress relaxation at 550 or 600°C (see Figs. 3.12 and E.1).

Material	IA	IB	IC
550°C	8.5×10^{12}	2.5×10^{14}	1.9×10^{14}
600°C	7.8×10^{11}	9.4×10^{13}	1.2×10^{14}

Note: the predicted dislocation density at the beginning of each stress relaxation test is $\sim 4.3 \times 10^{14}$ m^{-2}.

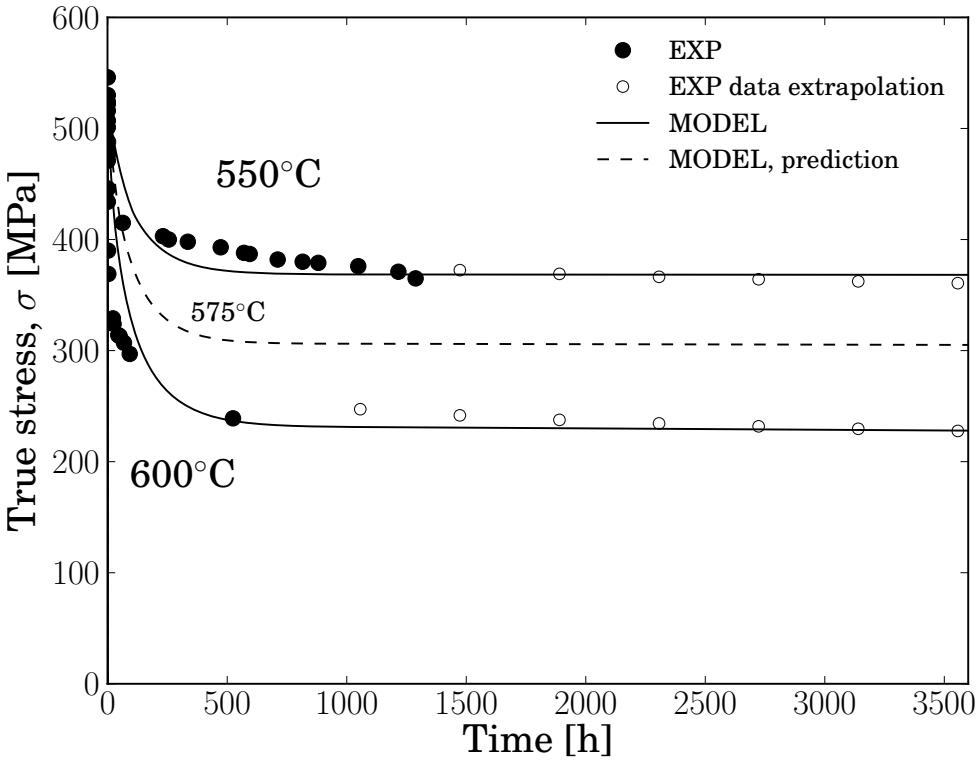

(a)

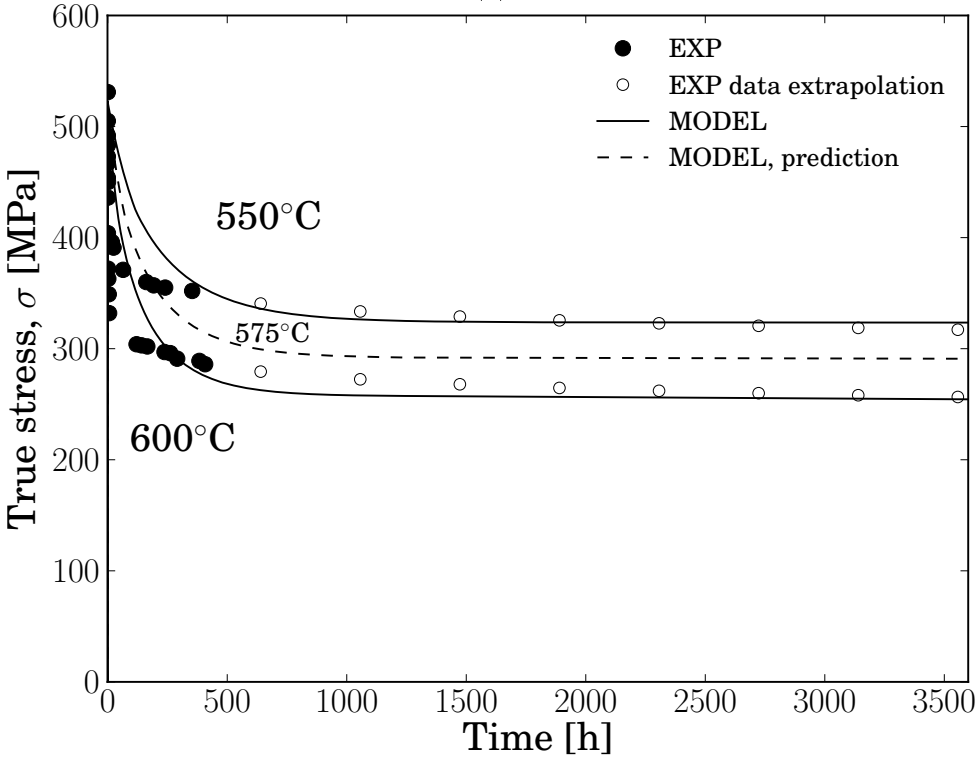

(b)

Figure E.1: Model simulation of the stress relaxation tests for the (a) IB and (b) IC steels.

APPENDIX F

Material parameters and physical properties of the AISI 316L constitutive model (IA steel)

	Notation	Value	Unit	Reference/Comment
Micro-structure				
	b	0.2544	$[nm]$	(Weiss and Stickler, 1972)
	d_0	34	$[\mu m]$	EBSD measurement
	α	0.3	-	Cheong and Busso (2004)
	M	3.07	-	FCC system
				w/o texture (François et al., 2012)
	e	1.5	$[\mu m]$	From EBSD observations
	γ_p	$1/\sqrt{2}$	-	FCC system
	k_{HP}	300	$[MPa.\mu m^{\frac{1}{2}}]$	(Schwartz, 2011)
Physical properties				
	μ	$85 - 0.03 \times \theta^*$	$[GPa]$	(Lacombe et al., 1990)
	κ	$184 - 0.065 \times \theta$	$[GPa]$	(Lacombe et al., 1990)
	a_γ	9×10^{-2}	$[mJ.m^{-2}.K^{-1}]$	(Lecroisey, 1971)
	γ_0	0.46	$[mJ.m^{-2}]$	(Lecroisey, 1971)
Flow rule				
	S_0^*	473	$[MPa]$	Calibrated
	$\dot{\epsilon}_0$	10^5	$[s^{-1}]$	Calibrated
	G_0	4.6×10^{-19}	$[J]$	Calibrated
	p	0.13	-	Calibrated
	q	1.05	-	Calibrated
Hardening evolution				
	K	2×10^{-2}	-	Calibrated
	d	0.5	$[nm]$	Calibrated
	λ	0.9	$[\mu m]$	Calibrated
	m_0	25	-	Calibrated
	c_1	250	$[MPa]$	Calibrated
	c_2	3.8	-	Calibrated
Static recovery				
	Γ_0	314	$[m^2.s^{-1}]$	Calibrated
	Q	6.31×10^{-19}	$[J]$	Calibrated
	β	0.2	-	Calibrated
	ρ_{eq}	0	$[m^{-2}]$	Calibrated
Twinning evolution				
	a_t	3.10^9	$[kg^{\frac{1}{2}}.m^{-1}.s^{-1}]$	Calibrated
	n_0	5×10^{14}	-	Calibrated
	ℓ	1.5	-	Calibrated

* θ is the temperature in $[K]$

APPENDIX G

Initial internal variable values for AISI 316L (IA steel)

G.1 Annealed state

Initial value of the twin volume fraction: $f = 0$

Initial value of the dislocation density: $\rho = 5.2 \times 10^{12}\ m^{-2}$

Initial internal stress tensors (in MPa):
$\mathbf{B}_I = \mathbf{0}$ and $\mathbf{B}_{II} = \mathbf{0}$

G.2 21% RT-rolled state

Initial value of the twin volume fraction: $f = 0.114$

Initial value of the dislocation density: $\rho = 3.9 \times 10^{14}\ m^{-2}$

Initial internal stress tensors (in MPa):

$$\mathbf{B}_I = \begin{bmatrix} B_{I_{11}} & B_{I_{12}} & B_{I_{13}} \\ B_{I_{21}} & B_{I_{22}} & B_{I_{23}} \\ B_{I_{31}} & B_{I_{32}} & B_{I_{33}} \end{bmatrix} = \begin{bmatrix} 73 & 0 & 0 \\ 0 & -73 & 0 \\ 0 & 0 & 0 \end{bmatrix}$$

and,

$$\mathbf{B}_{II} = \begin{bmatrix} B_{II_{11}} & B_{II_{12}} & B_{II_{13}} \\ B_{II_{21}} & B_{II_{22}} & B_{II_{23}} \\ B_{II_{31}} & B_{II_{32}} & B_{II_{33}} \end{bmatrix} = \begin{bmatrix} 23 & 0 & 0 \\ 0 & -23 & 0 \\ 0 & 0 & 0 \end{bmatrix}$$

(11=rolling direction, 22=thickness direction, 33=transverse direction)

APPENDIX H

Summary of viscoplastic constitutive model equations

Rate of change of the Kirchhoff stress tensor:

$$\dot{\mathbf{T}} = \mathcal{L} : (\mathbf{D} - \mathbf{D}^p) \tag{H.1}$$

where, $\mathcal{L} = 2\mu\mathcal{I} + \left[\kappa - \frac{2}{3}\mu\right] \mathbf{I} \otimes \mathbf{I}$

Flow rule:

$$\mathbf{D}^p = \frac{3}{2}\dot{\tilde{\epsilon}}^p \frac{(\mathbf{T}' - \mathbf{B})}{\tilde{\sigma}^e} \tag{H.2}$$

$$\mathbf{D}_g^p = \frac{3}{2}\dot{\tilde{\epsilon}}_g^p \frac{(\mathbf{T}' - \mathbf{B})}{\tilde{\sigma}^e} \tag{H.3}$$

with,

$$\dot{\tilde{\epsilon}}^p = \underbrace{(1-f)\dot{\tilde{\epsilon}}_0 \exp\left\{-\frac{G_0}{\mathcal{K}\theta}\left[1 - \left\langle \frac{\tilde{\sigma}^e - S}{S_0^* \frac{\mu}{\mu_0}} \right\rangle^p\right]^q\right\}}_{=\dot{\tilde{\epsilon}}_g^p} + \frac{\gamma_p}{\sqrt{3}M}\dot{f} \tag{H.4}$$

and, $\tilde{\sigma}^e = \sqrt{\frac{3}{2}(\mathbf{T}' - \mathbf{B}) : (\mathbf{T}' - \mathbf{B})}$

Internal stress tensor evolution:

$$\dot{\mathbf{B}} = \dot{\mathbf{B}}_I + \dot{\mathbf{B}}_{II} \tag{H.5}$$

$$\dot{\mathbf{B}}_I = \frac{\lambda}{b}\left[\frac{2}{3}\frac{M\mu b}{L_S}\mathbf{D}_g^p - \frac{1}{m_0}\mathbf{B}_I\dot{\tilde{\epsilon}}_g^p\right] - \beta\frac{M\mu b}{2\sqrt{\rho}}\frac{\mathbf{B}_I}{\tilde{B}_I}\dot{\rho}_{SR} \tag{H.6}$$

$$\dot{\mathbf{B}}_{II} = \frac{2}{3}c_1\mathbf{D}_g^p - c_2\mathbf{B}_{II}\dot{\tilde{\epsilon}}_g^p - \beta\frac{M\mu b}{2\sqrt{\rho}}\frac{\mathbf{B}_{II}}{\tilde{B}_{II}}\dot{\rho}_{SR} \tag{H.7}$$

Deformation resistance:

$$S = \frac{k_{HP}}{\sqrt{L_S}} + \frac{\alpha M\mu b}{L_W} \tag{H.8}$$

Evolution of the dislocation density:

$$\dot{\rho} = \frac{M}{b}\left[\frac{1}{L_S} + \frac{K}{L_W} - 2d\rho\right]\dot{\tilde{\epsilon}}_g^p - \underbrace{\Gamma_0 e^{-\frac{Q}{\mathcal{K}\theta}}\frac{\mu b^3}{\mathcal{K}\theta}\langle\rho^2 - \rho_{eq}^2(\theta)\rangle}_{=\dot{\rho}_{SR}} \tag{H.9}$$

with,

$$\frac{1}{L_S} = \frac{1}{d_{GB}} + \frac{1}{d_T} \quad and, \quad \frac{1}{d_T} = \frac{f}{2e(1-f)} \tag{H.10}$$

$$\frac{1}{L_W} = \sqrt{\rho} \tag{H.11}$$

Twin volume fraction evolution:

$$\dot{f} = \frac{\pi}{4}d_0^2 e(1-f)^3 n_0 \left(\frac{\tilde{\sigma}^e}{Ma_t\sqrt{\gamma}}\right)^{\ell}\dot{\tilde{\epsilon}}_g^p \tag{H.12}$$

where, $\gamma = a_\gamma\theta + \gamma_0$

Fissuration en relaxation des aciers inoxydables austénitiques de type AISI 316L

Résumé : La fissuration en relaxation (FER) peut apparaître dans les zones affectées par la chaleur de larges pièces soudées pendant leur utilisation entre 500 et 700°C. Il est admis que ce phénomène est induit par la relaxation à haute température de champs de contraintes résiduelles initialement introduits lors du soudage. L'objectif de ce travail est d'identifier, dans les aciers de type AISI 316L, les caractéristiques de ce type de matériaux, ainsi que les forces motrices, responsables du développement de la fissuration en relaxation.

La méthodologie proposée consiste à reproduire les conditions de la FER dans cinq aciers de type AISI 316L de compositions chimiques différentes en utilisant des éprouvettes de type "Compact Tension" (CT) pré-comprimées. L'étude des éprouvettes à l'aide du MEB, de l'EBSD, du MET et de la tomographie X a révélé que de l'endommagement intergranulaire s'était développé dans quelques une d'entre elles. Le niveau d'endommagement mesuré dans chaque éprouvette dépend de la nuance de l'acier, de la température et de la durée d'exposition thermique, et du rayon d'entaille.

Ce travail implique également la prédiction numérique des champs de déformations et de contraintes résiduelles dans les éprouvettes à l'aide d'une nouvelle loi de comportement viscoplastique à variables internes. La comparaison entre les champs de contraintes résiduelles prédits dans les éprouvettes de type CT et les distributions d'endommagement mesuré par tomographie a permis de déduire le niveau de contrainte résiduelle critique nécessaire pour l'initiation de la FER. Finalement, les distributions d'endommagement mesurées expérimentalement ont pu être correctement prédites numériquement avec une loi phénoménologique d'endommagement scalaire alimentée par les prédictions du modèle de comportement viscoplastique.

Mots-clés: AISI 316L, fissuration en relaxation, contraintes résiduelles, modèle de comportement, tomographie

Stress relaxation cracking in AISI 316L-type austenitic stainless steels

Abstract: Stress relaxation cracking can potentially be found in the heat affected zone of large welded parts after service in the 500-700°C temperature range. This phenomenon,also known as reheat cracking (RC), is driven by the high temperature relaxation of residual stress fields initially introduced during welding. The main objective of this doctoral thesis is to identify the material and microstructural characteristics as well as the driving forces responsible for RC damage development in AISI 316L-type austenitic stainless steels.

The proposed methodology relies on the reproduction of RC conditions in five chemically different AISI 316L-type steels using pre-compressed CT-like specimens. Subsequent investigation using SEM, EBSD, TEM and X-ray tomography revealed that intergranular damage had developed in some of the specimens. The extent of damage was found to depend on the steel grade, the temperature and duration of the thermal exposure, and the notch radius.

The numerical investigation of the local residual stress and strain fields in the specimens was carried out using a novel internal state variable-based viscoplastic constitutive model. A comparison between the predicted residual stress fields in the CT-like specimens and the intergranular damage distributions measured by X-ray tomography enabled the threshold level of local residual stresses associated with the initiation of stress relaxation microcracks to be inferred. Finally, the distribution of the measured local RC damage was modelled numerically by explicitly linking a suitable phenomenological scalar damage law with the above constitutive model. The corresponding results were found to be consistent with the observed damage distributions.

Keywords: AISI 316L, reheat cracking, residual stress relaxation, constitutive model, tomography

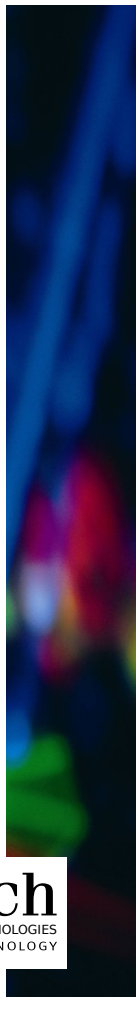

MINES ParisTech

ParisTech
INSTITUT DES SCIENCES ET TECHNOLOGIES
PARIS INSTITUTE OF TECHNOLOGY